University of Sussex

Cryogenic technologies for scalable trapped ion quantum computing.

Anton Grounds

Submitted for the degree of Doctor of Philosophy

University of Sussex

September 2018

Declaration

I hereby declare that this thesis has not been and will not be submitted in whole or in part to another University for the award of any other degree.

Signature:

Anton Grounds

UNIVERSITY OF SUSSEX

Anton Grounds, Doctor of Philosophy

Cryogenic technologies for scalable trapped ion quantum computing.

Abstract

There has been a great deal of effort and progress made towards building a fully scalable quantum computer but there are still significant engineering challenges to overcome. Trapped ions currently represent the best fundamental technology towards achieving this goal and so they form the basis for the work in this thesis.

In this thesis I describe the work towards creating a closed cycle cryogenic vacuum system driven by a Gifford McMahon cryogenic cooler. I will show the equipment required to trap a Ytterbium 174/171 ion on a cryogenic surface ion trap. The primary goal is to create a fast turn-around system for ion trap research. Room temperature systems suffer from long baking times and as such ion traps are rarely changed, this means that there is little room for testing and comparing of trap designs and predicting optimum trapping parameters as each trap is usually not changed unless there is a fault. In the cryogenic system, every effort is made to make the system generic enough to allow for any trap design to be tested and to be replaced within 24 hours.

To create reliable trapping parameters we require a toolkit that can numerically simulate the required RF and DC voltages used to trap the ions above the surface of the ion trap. There are many numerical methods that can be used (FEM, FVM, BEM, FTDI, etc) and in this thesis I describe multiple methods and what their relative benefits are. Since we want to create a full toolkit to allow for chip design and optimisation, most commercial programs suffer from inadequate API interfaces or they dictate which programming languages you can interface with. This would limit our abilities to develop and optimise trapping parameters, especially in a cryogenic system where the goal is rapid deployment. To this end I created a new toolkit based on the Scuff BEM solver engine that allows us to go from AutoCAD layout to field solver and gives us accurate field potentials that match micromotion compensated voltages to within 1%.

I describe a novel cryogenic resonator built out of superconducting wire based on an auto-transformer topology, I compare its strengths and weaknesses compared to other technologies already in use for trapped ion research.

I also describe a novel DSUB design with integrated modular filtering which allows for 50 connections per DSUB. This DSUB is used to connect two sets of 50 wires to a PCB for wirebonding to the surface trap. This allows me to save space within the 4k shield where other PCB designs would not fit. Also it is modular in design which allows for different cutoff frequencies to be swapped out as desired.

I also describe different chip mounting technologies including epoxy based, physical clamping and indium foil based. After extensive testing the indium foil diebonded approach is deemed as being the most reliable and fastest non-destructive method.

I also describe a novel cryogenic coil design for generating $12\mathrm{T\,m^{-1}}$ field gradients for microwave based ion gates with Ytterbium 171. I then describe the creation of a combined RF and microwave antenna for delivering coherent RF and 12.6GHz microwave radiation inside the cryogenic environment. This design is much smaller than typical waveguide typologies used.

I finish by showing the first trapped ions in a cryogenic surface ion trap in the UK and heating rate tests performed on two different linear surface traps. The first trap was a sapphire based, 150µm ion height linear trap with a measured heating rate of $Se(1MHz) = 5.93(10) * 10^{-14}(V/m)^2$. The second ion trap is a 50k Silicon based, 100µm ion height linear trap with a measured heating rate of $Se(1MHz) = 2.45(10)*10^{-13}(V/m)^2$

Acknowledgements

The world of quantum computer research is an exciting and moving field with a lot of opportunities. I must thank firstly Professor Winfried Hensinger for giving me the opportunity to carry out my research within the IQT group at Sussex. I also want to thank Sebastian Weidt for his patience and help throughout these four years. I also want to thank Darren DeMotte for teaching me about cryogenics and passing the system that he started on to me. In general I would like to thank everyone who I have had the opportunity to meet and work with during my time at the University of Sussex, in particular Zak Romaszko and Raphaël Lebrun who have always been an unending source of humour and enlightenment. I also want to thank Andrea Rodriguez-Blanco for the time she spent with me working on the cryogenic system. I also want to thank Wu Wei who joined myself and Andrea on the cryogenic system for one year and without his help and support we would never have trapped for the first time. I would like to thank Ethan Potter who was going through the same struggles as I in trying to trap, and I will always remember the day when we first trapped for the first time. I also would like to thank my family for giving me love and support throughout my time and my wife who kept me going even through the ups and the downs.

Contents

List of Tables v

List of Figures xiv

1 Introduction 1

1.1 The Computer . . . 3

1.2 The Quantum Computer . . . 5

1.2.1 The DiVincenzo criteria . . . 5

1.2.2 Trapped Ion Quantum Computer . . . 6

1.2.3 Cryogenic Trapped Ions . . . 6

1.3 Thesis Outline and Thesis Contributions . . . 8

2 Background Theory 10

2.1 Radio Frequency Paul Traps . . . 11

2.2 Doppler Cooling . . . 16

2.3 Doppler recooling and heating rate . . . 17

2.4 The Yb^+ Ion . . . 18

2.4.1 Photo-ionisation . . . 18

2.4.2 $^{174}Yb^+$ Energy level structure . . . 18

2.4.3 $^{171}Yb^+$ Energy level structure . . . 20

3 Field Simulation Toolkit 22

3.1 Computational methods for electromagnetic field simulations . . . 23

3.1.1 Integral and Differential Forms . . . 24

3.1.2 Discretization . . . 25

3.2 Ion Trap Electric Field Solving . . . 28

3.2.1 ScuffEM . . . 29

3.2.2 LIBSCUFF . . . 32

3.2.3 Reading from *.dxf . . . 33
3.2.4 Mesh electrodes . . . 34
3.2.5 Call LIBSCUFF . . . 35
3.2.6 DC Voltage Control . . . 36
3.2.7 Trajectory simulator and shuttling . . . 37
3.3 Conclusion . . . 40

4 Experimental Setup 41
4.1 Lasers . . . 44
4.2 AOM and EOM Setup . . . 46
4.3 Laser Locking . . . 49
4.4 Lower Optics Table . . . 51
4.5 Upper Optics Table . . . 53
4.6 Imaging Optics . . . 55
4.7 RF and microwave generation . . . 57
4.7.1 Trapping RF . . . 57
4.7.2 Coherent RF and microwaves . . . 58
4.8 Oven Controller . . . 59
4.9 DC Setup . . . 60

5 Cryogenic Vacuum System 67
5.1 Cryogenics . . . 69
5.1.1 Cryogenic Noise Reduction . . . 70
5.1.2 Superconductivity . . . 72
5.2 Cryocooler and Vacuum System . . . 73
5.2.1 Cryocooler . . . 73
5.2.2 Ultra Low Vibration Interfaces . . . 74
5.2.3 Gas Buffered Ultra Low Vibration Interface . . . 76
5.2.4 Vacuum System . . . 76
5.3 Internal Vacuum Components . . . 79
5.3.1 Radiation shields . . . 79
5.3.2 Laser Access Windows . . . 80
5.3.3 Internal wiring . . . 82
5.4 Cryogenic Chip Mount . . . 84
5.4.1 First Generation Chip Mount . . . 84

5.4.2 Second Generation Chip Mount . . . 85
5.4.3 Ion Trap Mounting Methods . . . 86
5.4.4 Cryogenic PCB and Wirebonding . . . 89
5.5 Atomic Oven . . . 91
5.6 Cryogenic RF Resonator . . . 93
5.6.1 Resonance and Q . . . 93
5.6.2 Resonant Gain . . . 94
5.6.3 Resonator Design . . . 95
5.6.4 Matching Networks . . . 96
5.6.5 Autotransformer . . . 98
5.7 Cryogenic Microwave and RF Antenna . . . 101
5.7.1 Antenna theory . . . 101
5.7.2 Patch Antenna . . . 102
5.7.3 Patch Transmission Line Model . . . 104
5.7.4 Patch testing and mounting . . . 108
5.7.5 RF Emitter . . . 109
5.7.6 Magnetic Field Gradient Coils . . . 110
5.8 Conclusion . . . 113
5.9 Characterisation of the ion traps . . . 114
5.9.1 Chip Preparation . . . 114
5.9.2 Generation 1 - Linear Sapphire 2014 . . . 115
5.9.3 Generation 2 - Linear Sapphire 2017 . . . 124
5.9.4 Generation 3 - Linear Silicon 2018 . . . 129
5.9.5 Comparing heating rates . . . 134
5.9.6 Preparation for a complex junction . . . 135
5.9.7 Conclusion . . . 140

6 Conclusion **141**
6.1 Future work . . . 142

Bibliography **143**

A Beam Blocks **161**

List of Tables

3.1 Table of a 150 µm surface ion trap with sapphire substrate, comparing simulated parameters values to measured values after micromotion compensation. 32

5.1 Cryostat details and measured results. Vibration is spread spectrum with dominant peaks at 50Hz and 100Hz. 75

5.2 Thermal expansion of fused silica, PTFE and Copper 81

5.3 Table of important physical parameters of the patch antenna substrate. . . 104

5.4 Transmission line model patch 106

5.5 Table of trapping parameters for the second generation ion trap. 125

5.6 Table of trapping parameters for the second generation ion trap. 132

List of Figures

2.1 Quadrupole trap. (a) shows the RF electric fields and the force experienced by the ion when the RF electric potential is positive on the top and bottom electrodes during one half of the AC voltage cycle. (b) shows the RF electric fields and the experienced by the ion when the electrodes driven with the opposite polarity during the second half of the AC cycle. 13

2.2 Simplified energy diragram for a Yb atom showing both single and double photon ionisation[1, 2, 3] 19

2.3 Energy state diagram of $^{174}Yb^{+}$ shown are the three principle laser wavelengths and state life times. The dashed arrows show optical transitions where the solid arrow shows a transition mediated by high energy collisions [4, 1, 5, 6, 7, 2, 8] 19

2.4 Energy state diagram of $^{171}Yb^{+}$. Shown are the hyperfine states caused by the nuclear spin. Also shown are the frequencies of the hyperfine splitting in GHz [4, 1, 5, 6, 7, 2, 8] 20

3.1 (a) shows a two dimensional slice of the three dimensional FEM discretized mesh at low resolution (323 elements). (b) shows a uniform high resolution mesh (3946 elements). (c) shows the use of a high resolution ring to aid in directing high resolution mesh generation at the predicted position of the ion (471 elements). 26

3.2 A two dimensional slice of the three dimensional BEM discretized mesh. Only surfaces are meshed in a BEM problem. Shown are the DC electrodes, RF electrodes and centre ground. 27

3.3 Workflow for the BEMSolver field solver. This is a manual process that starts by importing the *.dxf output geometry files from AutoCAD™and converting them into 3D lines that represent the outer bounds of the electrodes, then importing those lines into BEMSolver where the electrostatic field at defined points above the surface of the trap are calculated and saved into *.dat files. The *.dat files are then loaded into Mathermatica where the ponderomotive potential is calculated so that we can solve for the ions position and calculate DC values. If new field data is required or the trap geometry needs altering the original *.dxf files are altered then reimported into BEMSolver. 29

3.4 Meshed ion trap design with no gaps between electrodes. Since this layout is symmetrical along the z axis computational time can be reduced by defining a symmetrical boundary at this midpoint. 30

3.5 Plot of the ion trapping position from the RF electrode electric fields. The dashed line contours are the gapless approximation result, the solid line and colour contours are from ScuffEM. Calculated ion height of 135.6 µm for the gapless approximation, 136.1 µm for ScuffEM. Red dot represents the ion position by gapless approximation. 31

4.1 Overview of the hardware that will be covered in this chapter, the cryogenic vacuum system will be covered in Chapter 5. 42

4.2 Lighthouse Photonics Sprout-G pump laser delivers 12 W of 532 nm light to the Ti:sapphire M Squared SolsTiS module. This module is comprised of a titanium sapphire rod laser and generates 738 nm laser light. This then gets shaped and directed into an M Squared ECD-X frequency doubler which contains a Lithium triborate (LBO) crystal that doubles the laser frequency, emitting 369.5 nm wavelength light. 45

4.3 AOM and EOM setup depicting the incoming beam path (Top right) passing over a half height mirror and entering the AOM. This light is then collimated by a lens onto a prism that returns the light with a vertical offset. The returning beam then gets redirected by the half mirror through the EOM and polarisation maintaining optics. 47

4.4 AOM switch in shielded box. Labelled are the TTL control that switches the input to output 1 or 2, the RF input and two RF outputs and the power port. 48

4.5 Diagram showing the layout of the lower optics table. Depicted is the M squared laser and the optics taking the 738 nm light to the wavemeter and locking setups, the main 369.5 nm output is split and sent into the AOM and EOM setup. On the right side of the table the output couplers for the 399 nm and 935.2 nm lasers are positioned along with the output coupler for the 369.5 nm laser after returning from the AOM and EOM setup. Also shown are the beam shaping optics for the 369.5 nm laser and the beam overlap of the 399 nm and 935.2 nm lasers which then pass to two periscopes for the upper optics table. 52

4.6 Upper optics table features a optical breadboard with two full axis translation stages. These stages allow for full lateral and angular control of the beam through the vacuum system windows and across the ion trap. The two lenses allow for focusing of the beam waist at the ion position. The photodiode is used with a 369.5 nm filter to detect the pass-through beam power. 53

4.7 Imaging setup. Shown is the objective lens, two singlet asperical lenses with the iris at the focal point. After the 100mm lens there is a 369.5 nm filter and a motorised flipper mirror. This mirror allows for switching between the EMCCD camera and the PMT device. 55

4.8 System diagram showing the RF generator and amplifier. A directional coupler is used for detecting the reflected RF power from impedance mismatching inside the vacuum system. 57

4.9 DAC system overview, X1A and X1B 16-bit registers contain the voltage word before processing by the DAC's internal architecture. The M 16-bit register contains the multiplier offset value and the C 16-bit register contains the sum offset value. Also shown is the processing path, either the X1A or X1B register is selected via an input control register (not shown). The X1A or X1B register is then passed through the multiplier and sum offset encoders into the second set of voltage registers X2A and X2B. These registers can then be activated and sent to the DAC output. 62

4.10 Image showing the top and bottom of the completed DAC board. Shown is the connector for the main voltage rails of the DACs that are from a linear $\pm 15V$ power supply. Also shown is the 5V reference that the DAC voltage output is relative to and the 5V regulator that powers the digital logic. The SPI socket is for the data communication card or cable. On the bottom of the board is the signal ground connector and the two DACS. There is also a 5V selector jumper for selecting between USB powered or 5V regulator powered for the interface card. 64

4.11 FTDI USB Module with quad Multipurpose universal asynchronous receiver-transmitter / Multi-Protocol Synchronous Serial Engine (UART/MPSSE) interfaces. 65

4.12 Full DAC PCB and FTDI daughter board, case and IDC cables not shown. 65

5.1 Figure showing equilibrium saturation curves of common gasses. Adapted from [9] 70

5.2 Figure showing the heat map profile of the SHI RDK-415 running at 50Hz. This map shows the equilibrium temperature for a given heat load. Adapted from [10] 75

5.3 (a) Schematic diagram showing the entire vacuum system. (b) Highlighted digram showing the buffer gas and heat exchangers. Adapted from [1] . . . 77

5.4 Picture showing the fully assembled vacuum system. Clearly visible are the ULVI (top) and the vacuum octagon and imaging optics (bottom). 78

5.5 Cross-sectional render showing inner and outer radiation shields, 4K and 50K respectively. Also shown are the laser access windows, imaging windows and cold edge of the 4K stage. 80

5.6 Window holder comprised of two PTFE rings and two bolts that gently hold the window vertical and grip the copper shield. 81

5.7 Diagram showing the cable wrapping process, on the left the cables are loosely wrapped around the 50K shield in a double helix pattern with thermal anchoring every full turn. On the right the cables pass through from the 50K shield down to the 4K shield where they spiral up and through the radiation shield towards the mounting structure. 83

5.8 Modified and unmodified ceramic pin grid array (CPGA) 208-pin chip carrier (Global Chip Materials PGA10047002). Adapted from [1] 84

5.9 Design of the top chip mount (a) that is removable with two screws for fast chip swapping. The bottom chip mount (b) that is fixed with six screws into the cold edge. Both parts are made out of OFHC copper. 86

5.10 Three generations of surface clamps. (a) metal clamps made from copper sheet, (b) clamps made from copper wire, (c) clamps milled from an aluminium block and tightened with copper wire. 87

5.11 Flow profile for the diebonder. Starting profile gradient of $1\,^{\circ}\mathrm{C\,s^{-1}}$, 10 s holding time at 160 °C then a $0.5\,^{\circ}\mathrm{C\,s^{-1}}$ cool down ramp. 88

5.12 Diebonding process, (a) shows the chip under the heated head before the indium has melted. (b) shows the melted indium ejected out from the sides of the trap. (c) after cooldown and excess indium removal the heated head is raised off the trap. 88

5.13 Fully assembled trap with PCB and chip mount. Custom PCB is milled from Rogers 3003 substrate. Trap in the picture is a linear surface trap with 24 DC connections and one RF connection. RF SMP connection can be seen in the top left of the image. 90

5.14 Series resonant circuit, where R1 is the combined losses of both L1 and C1. 94

5.15 Circuit diagram of the autotransformer resonator used in the cryostat circuit. The autotransformer is "tapped" to tune the optimum input impedance as close to 50 Ω as possible. The capacitor divider is used to create a high impedance monitor point to measure the trap voltage via an external scope. 99

5.16 Centre fed (current fed) dipole with current and voltage plots. The standing wave on the dipole forms a loop electric field half a wavelength away from the antenna. This folded electric field propagates away from the antenna in a torus radiation pattern. 101

5.17 A patch antenna. (a) shows the top of the patch with the radiative electric field lines along the short edge (W). (b) shows the side on view of the patch and the electric field line density. L is the length of the patch and the direction of polarisation, W is the width. h is the dielectric thickness and t is the conductor thickness. Adapted from [11] 103

5.18 Probe fed patch antenna. The central core of the coax passes through the dielectric and bonds to the surface conductor. The position of the feed from the centre determines the impedance. 103

5.19 Patch and the equivalent circuit model under the transmission line model. (a) The physical patch with length L and width W. (b) Circuit model for the admittance parameters of the two slots. G1 and B1 are the two "virtual" components of the model that represent slot one, G2 and B2 are the two "virtual" components of the model that represent slot two which are used in the models approximation. 104

5.20 Graph of impedance long the length of the patch. 106

5.21 (a) shows the far field plot of the patch. (b) a 2D slice along the YZ plane of the far field plot. 107

5.22 Single port scattering parameter after optimisation routine. 108

5.23 (a) Milled patch on Rogers 3003 substrate. (b) The full RF and microwave assembly with coax feed and SMA connector. 109

5.24 Microwave patch antenna Poynting vector and magnetic field vector shown relative to the ion trap. The antenna is mounted at 45° to the matnetic field vector and also rotated 45° to the surface normal of the trap. 110

5.25 Image of one coil. 121 windings in four layers of superconducting NbTi wire. Mounted on a PTFE holder. 111

5.26 Graph of the simulated magnetic field strength along the coil principle axis. In the centre at the ion position the gradient is 11.85 $\mathrm{T\,m^{-1}}$. 112

5.27 First generation microfabricated linear ion trap. Designed for a 100 µm ion height. The RF electrodes are 144 µm wide with 5 µm gaps (trenches) between the electrodes. The central ground width is 86 µm and the DC electrodes have a width of 200 µm. This generation of traps had issues with the cleaving process where the wafer is snapped to separate the traps, this can be seen by the damage to the top right of the image. 116

5.28 Linear surface ion trap after cryogenic cycle, that shows extreme surface damage. The cause was attributed to titanium removal by hydrofluoric acid during the microfabrication process. 117

5.29 Stitched EMCCD camera image of "glow" between one RF electrode and the neighbouring central ground electrode. 118

5.30 Spectral decomposition of trap "glow" over three different applied RF voltages. Regions of brightest "glow" tend to exhibit in the longer wavelengths (<550 nm). Images taken on a new trap at the first appearance of "glow". Image exposure is 0.5 s. 120

5.31 Image sequence of a wide trench (30 µm) ion trap design, showing the "glow" positions over an RF voltage range from 112 V to 600 V. 121

5.32 Composite images from three different locations where "glow" was observed. The top row of images are focused onto the gold surface of the electrodes. The second row is focused half way between the surface and the bottom of the trench. The bottom row is focused on the trench floor.(a) is centred on the corner of a DC electrode, (b) is along the edge of an RF electrode, (c) is from the middle of a DC electrode edge. 122

5.33 ImageJ 3D image from 5 stacked microscope images displaced by 1 µm increments. Ejected gold volume with little observable surface damage suggest gold is ejected from the bottom of the gold layer at the gold-chromium boundary. 123

5.34 Image of a surface ion trap without the top electroplated gold layer. Visible is the chromium damage after observing glow. Also shown are Lichtenberg style damage marks under the surface of the chrome layer. 123

5.35 Second generation microfabricated linear ion trap. Designed for a 150 µm ion height. The RF electrodes are 147 µm wide with 10 µm trenches. The central ground (GND) width is 180 µm and the DC electrodes have a width of 145 µm. 124

5.36 First ion trapped on the cryogenic system. Lifetime of ion was 4 hours 32 minutes. This image was taken shortly after the ion appeared for the first time, this is before any optical adjustments or micromotion compensation. . 125

5.37 Image of 6 ions with a lifetime of 1 hour 32 minutes. 126

5.38 Generation two ion trap normalised count rate ($\dot{n}$) binned photon counts for 250 runs with a laser-off interval of 15 seconds. Each dot represents the value of a bin with appropriate error bars, time period between bins is 500 µs. 127

5.39 Generation two ion trap heating rate ($\dot{n}$) data from four sets of measurements at 10,15,20 and 30 second laser-off intervals. The gradient gives the heating rate of the ion as 105(7) quanta/s for an axial secular frequency of 137(1) kHz. 127

5.40 Images from the DAC interface test. From (a) to (c) the ion is shown as it passes through the 369.5 nm laser light ($\approx$ 100 µm visible path). The total distance shuttled is 1855 µm or 13 DC electrode widths. 128

5.41 Third generation microfabricated linear ion trap. Designed for a 100 µm ion height. The split RF electrodes are 144 µm wide with 5 µm trenches. The central ground width is 86 µm wide and the DC electrodes have a width of 200 µm. 130

5.42 Graph of resonator Q vs temperature of the high resistivity silicon microfabricated ion trap. At 315 K the Q is 37.9 which rises to a maximum of 49.4 at 81 K. There is then a Q inversion around 60 K. At around 18 K to 14 K the cryogenic wire of the resonator starts superconducting causing the Q to rise. 131

5.43 First cryogenically trapped ion on the high resistivity silicon substrate surface ion trap. 132

5.44 Generation three normalised count rate ($\dot{n}$). Binned photon counts for 250 runs with a laser-off interval of 15 seconds. Each dot represents the value of a bin with appropriate error bars, time period between bins is 500 µs . . 133

5.45 Generation three recooling florescence ($\dot{n}$) data from four sets of measurements at 10, 15, 20 and 30 second laser-off intervals. The gradient gives the heating rate of the ion as 423(7) quanta/s for an axial secular frequency of 138.8(10) kHz. 133

5.46 Graph showing published noise spectral density results from both cryogenic and room temperature systems. Open symbols (holes) are cryogenic systems. Closed symbols (filled) are room temperature. Bowties are systems with in situ surface milling equipment. Our two data points are represented as blue crosses. Adapted from Chiaverini *et al.* [12] 135

5.47 Custom DSUB with built in filtering. The PCB section is soldered to the main PCB, that is wirebonded to the trap. The filter and cable sections normally remain within the vacuum system. The DSUB contains 50 connections and measures 69 mm long, 19.2 mm deep, when closed, and 9 mm wide. 136

5.48 Sample x-junction from generation three. This x-junction design has 60 DC connections split into four corner groups. It also features four RF inputs on the left and right side. 137

5.49 X-Junction PCB design with overlaid trap geometry. (a) shows the top layer with DC terminations from two DSUBs and vias for RF pass through from the bottom layer. (b) shows the bottom layer with dual RF traces terminating in a single SMP connector. SMP connection can be seen in b) on the far right where the RF line ends in a microstrip stub 139

A.1 Beam block controller. Pulse coded modulation (PCM Data) and ground lines are shared between all beam blocks. The MOSFETs are switched by the Gate lines, enabling each servo when required. 162

Chapter 1

Introduction

Ever since the earliest days of mankind, we have sought to understand and control the environment we live in. The drive to question our world is ingrained in the very fabric of our lives and through the ages technology has developed as we further our understanding. With a need to cross the oceans we developed ships, to cross land we developed vehicles such as cars, and to harness he air we developed balloons and aeroplanes.

With every advancement we always had more questions. "Why do objects fall down?", "Why is the sky blue?", "How do I cure the sick?" and though distasteful as it may be "How do I win the war?". For the longest time in human history these questions could be answered by trial and error with the passing of information from successful trials from generation to generation. We could answer what happens but not the how or why of the questions. Simple experiments which probed the fundamentals of the universe were still a long way off by the 18th century but slowly the simple explanations given seemed woefully inadequate and more complex questions needed answering. These questions were beyond what a human could calculate in a reasonable time frame, and a machine was needed that could answer them.

In the 19th century the industrial revolution was growing at a fervent pace. The need for more materials and cheaper items drove engineers and entrepreneurs to invent ways of automating the building process. One such inventor was Joseph Marie Jacquard who invented the Jacquard loom in 1804. This loom was programmable by the use of punch cards that told the loom what pattern to weave. It was one of the earliest attempts at creating a programmable machine that would solve a problem, even if the problem was limited to the realm of patterns in fabric.

In 1822 another inventor and mathematician Charles Babbage took the field of pro-

grammable machines further. He designed what is known as a "Difference Engine" which could calculate, by divided differences, polynomial functions. While the original machine failed, a smaller version was built in 1832 with the help of Joseph Clement and successfully run. This was the first time that a working machine for calculating numeral problems was demonstrated.

1.1 The Computer

All these machines, as impressive as they may be, were designed to solve limited sets of problems and while it is arguable that the Jacquard loom is Turing complete, it was not formally understood or operated in this way at its creation.

In 1936 the mathematician Alan Turing envisioned a machine (later called the Turing Machine[13]) which could be programmed in any arbitrary way allowing for the calculation of any computable algorithm, no matter how complex. The computer was born.

With this the concept of digital bits was created. A bit is a two level state that can either be a 1 or a 0. This may be represented by a two-state device such as an electronic switch. Strings of bits can then represent information and processes in the computer.

It was not until 1945 that the first general-purpose Turing-complete computer was built at the University of Pennsylvania, it was called Electronic Numerical Integrator and Computer (ENIAC).

Over the following decades computers spread into every aspect of human life. With the invention of the transistor in 1947 these machines began to shrink in size and grow ever more complex. In 1965, Gordon Moore noticed a trend in the complexity of the electronics used to create the central processing units (CPUs). He published an article detailing that the number of transistors in the CPU would double every year, now commonly known as Moors's Law.

There was a problem, however. While the machines continued to grow in speed and computational power, the nature of some algorithms and some equations were still too complex to be calculated in a usable time scale.

Problems such as sorting a list of numbers into ascending order using the Quicksort algorithm[14] that take on average, $n \log n$, number of steps to complete, where n is the size of the list to be sorted. This is commonly written as $O(n \log n)$ in what is called the "big O notation". Algorithms which show running times like $O(n), O(n \log n), O(n^2)$ are part of a complexity class called polynomial time.

There exists other algorithms like the Dixen factorisation method[15] for factorising numbers. That take $O(2^{n^{1/3}})$ time.

The travelling salesman problem scales as $O(2^n)$. These classes of problems are known as exponential time. That is to say that a deterministic Turing machine would compute such problems in exponential time. This is why classical computers struggle to solve complex exponential-time problems in a usable time frame.

It is for the problems that solve in exponential time or higher orders that a new kind of computer is needed.

1.2 The Quantum Computer

It is by using quantum mechanics that we can create a machine capable of running special algorithms in polynomial time that would normally take exponential time to complete.

In a quantum computer the fundamental states are created from a superposition of basis states. Using Dirac notation this is written as,

$$|\Psi\rangle = \alpha\,|0\rangle + \beta\,|1\rangle \tag{1.1}$$

where $|0\rangle = \begin{pmatrix} 1 \\ 0 \end{pmatrix}$, $|1\rangle = \begin{pmatrix} 0 \\ 1 \end{pmatrix}$, α and β are complex coefficients. This is known as a qubit or quantum bit.

Since we are representing the states as a superposition of basis states if we process a string of (n) qubits with an operation we are performing the operation on 2^n basis states, in parallel. In general, measuring the superimposed output state of such a quantum operation is not fully deterministic, so the apparently exponential increase in power cannot be naively accessed. Nevertheless the use of superposition states can significantly speed up the rate at which we process information.

Traditional classical algorithms do not apply on a quantum computer therefore new quantum algorithms need to be developed. An example of a quantum algorithm is the quantum equivalent to the factorisation algorithm known as the Shor algorithm[16]. This algorithm reduces the complexity of the problem from exponential to polynomial time.

In 1989 Deutsch described techniques to create a more general class of problems, which laid down the theoretical groundwork for a universal quantum computer[17].

Much work has been done not only on the theoretical background for creating a universal quantum computer but also the hardware to allow us to interface with the quantum world in a controllable manner[18].

1.2.1 The DiVincenzo criteria

In 2000 DiVincenzo laid out the criteria that any fully-functional quantum computer would need to meet, from his published work [19] he defines the following.

1. A physical system where we can create qubits to perform quantum operations.
2. The ability create an initial state in the qubits of the physical system, such as $|000...\rangle$
3. The ratio of the decoherence time to the qubit gate operation time should be sufficiently large.

4. A set of quantum gates that can be used for performing quantum algebra

5. A way of measuring the qubits and reading out their information.

There are many physical systems that have been proposed and physically demonstrated, these systems, have shown progress towards meeting parts of the DiVincenzo criteria. Some examples of these various systems are superconducting qubits [20, 21], nitrogen vacancy centres in diamond [22, 23], photons [24], molecules [25], quantum dots [26], neutral atoms [27] and ions [28, 29]. There have also been proposals of hybrid systems utilising the good features of more than one technology[30].

1.2.2 Trapped Ion Quantum Computer

Out of all the technologies that have been demonstrated, electron spin systems such as ions have fit most of the DiVincenzo criteria [28].

In 2008 a 99% fidelity two-qubit gate was demonstrated with calcium ions [31]. More recently in 2016 a 99.9% fidelity gate was demonstrated [32, 33].

To meet the first DiVincenzo criteria the system needs to be scalable, this includes the ability to add multiple qubits to the system to allow for complex calculations to be solved and to help with errors through the use of error correction algorithms. The system must also be scalable such that it can be physically constructed with the resources at hand, taking into account costs, labour and materials needed.[34, 35].

The second and third DiVincenzo criteria have been demonstrated with ions[36] through the use of lasers or a combination of lasers, magnetic fields and microwaves[37] to be able to set and reset the energy states of the ion, and also perform gate operations such as the quantum CNOT[38].

The fourth and fifth DiVincenzo criteria have also been demonstrated with ions[36, 37] with typical decoherence times being in the hundred-millisecond timescales while the gate times are in the microsecond and low millisecond time scales.

1.2.3 Cryogenic Trapped Ions

Cryogenic ion traps have been demonstrated before[39, 40, 41] and while they bring interesting engineering challenges to the field of ion trapping, they also grant many benefits.

By utilising the properties of cryogenics it is possible to obtain the very low pressures required to trap much faster than for traditional room temperature systems. It is also

possible to use a wider range of materials within the vacuum environment as cryogenic temperatures lower the rate of outgassing, although care must be given to other properties such as the thermal expansion coefficients of the materials and materials becoming brittle. Also, when using semiconductors, their electrons can "freeze-out" where the electrons do not pass from the valence band into the conduction band and as such become insulators, losing their useful doped properties.

Additionally, it is possible to utilise superconductors and superconducting materials which helps achieve the high voltages required for ion trapping and allows me to use high currents, in particular in the magnetic field generation coils and primary coil of the RF resonator, without introducing dissipative losses.

1.3 Thesis Outline and Thesis Contributions

Chapter 2: In this chapter, I describe the fundamental theoretical underpinnings that will be required throughout this thesis. I define what a qubit is, how it is represented, and how we can form logical gates from combinations of these qubits. I describe the Ytterbium atoms outer electronic structure and how this structure can be used to perform quantum operations, this work is largely inspired on the works of Joe Randell [42], Klaus Mølmer and Anders Sørensen [43]. I show the energy levels of the Ytterbium atom and the associated laser wavelengths needed to address them from published works by our group, in particular from the thesis work by Altaf Nizamani [44]. I finish by describing the theory used for measuring the heating rate of the ion known as the Doppler recool method; this method was first theorised by David J. Wineland and Hans Georg Dehmelt [45] with the later mathematical model coming from the work of J. H. Wesenberg et al [46] for measuring heating rates.

Chapter 3: Part of the requirements to be able to trap an ion and perform quantum logic operations with those ions is the need to calculate the required electric fields in vacuum. These fields will affect the motion of the ions, as charged particles, and allow us to confine its position and direct its movement as required by our experiments. In this chapter, I describe the creation of a mathematical toolkit application used for calculating these electric fields based on the existing field simulator ScuffEM by Homer Reid. I compare its processing speed and field accuracy to other numerical methods and how this new toolkit can allow for rapid field simulation of ion trap geometries directly from the layer information used for the microfabrication of the trap.

Chapter 4: To be able to use ions to perform quantum logic, we need an environment that can contain them. Since ions are very light charged particles, they must exist in a ultra high vacuum (UHV) (10^{-11} mBar typical). Therefore we need to create a vacuum system with appropriate feed-throughs for the required DC and RF electric fields, side windows for laser access and an imaging window to allow us to read back the state of the ion. We also need to create a setup on an optical table with all the required laser optics and electronics needed to address and readback from the ion in our vacuum system. In this chapter, I describe the external components required to run a cryogenic vacuum system. Work started on the imaging optical setup with the help of Darren De Motte and

Altaf Nizamani and work on the laser locking techniques comes from Tomas Navickas. I describe my work on the laser alignment and laser control setup, computer control system and the technology I created to control 80 DC electrodes through a custom 80 channel 16-bit DAC for ion control and shuttling.

Chapter 5: It is in this chapter I continue from chapter 4 by delving into the internal workings of a functional cryogenic vacuum system for trapping ions and demonstrate some novel technologies I created such as a cryogenic patch antenna, superconducting magnetic gradient coils and surface trap mounting system and a novel autotransformer based cryogenic resonator. Darren De Motte contributed work on the outer vacuum system and imaging window. A cryogenic system was chosen due to its ability to get low vacuum pressures rapidly through multiple techniques such as cryo-sorption and also the ability to reduce external electrical noise through shielding by copper radiation shields at cryogenic temperatures. Cryogenic temperatures also reduced unwanted electrical generated interference such as Johnson-Nyquist noise which is dependant on the temperature of the material. The result is a system that would allow me to rapidly test multiple trap geometries without the usual long baking procedures needed of typical room temperature systems.

Chapter 6: In this chapter, I review the testing procedure of three generations of linear surface ion traps, these traps were fabricated by fellow colleagues Bjoern Lekitsch, Reuben Kahan Puddy, Weikang Fan and Zak Romaszko at Sussex and Southampton universities. I demonstrate how the rapid turnaround of the cryogenic system and its novel mounting system allowed me to feedback trap performance data to the microfabrication team in a matter of weeks which allowed us to find faults in our microfabrication techniques. I describe one such problem that we fixed by studying RF-induced "glow" around the electrode structure of the ion trap, this allowed us to make microfabrication changes quickly such that the following batch of ion traps was functional. I also show the simulated trapping parameters from the trap simulation toolkit and compare the results of this simulation to the optimised trapping parameters on the working system. I also show the measured heating rates of each chip and show how they compare to other published results. I end by showing further work towards trapping on complex geometries using the 80 channel custom DAC and describe the creation and testing of a custom high-density electrical connector with built-in filtering.

Chapter 2

Background Theory

Our ultimate goal is to create a quantum system that can be manipulated and measured such that we can perform quantum operations on that system. As previously discussed there are many methods we can employ to create such a quantum system, including photons, neutral atoms and ions. What ever system we decide to create we need to fulfil the DiVincenzo Criteria previously mentioned, and for the focus of this research I focused on cryogenically trapped ions as the system of choice. Much work has been done to allow for ions to be used as a medium for creating a quantum computer. In 1978 both Wineland *et al.* [47] and Neuhauser *et al.* [48] independently demonstrated laser Doppler cooling, this allows us to lower the motional energy of the ion using laser light and helps keep the ion trapped in the surface ion trap. There are two main types of trap that can be used for confining charged particles such as ions. Penning traps, named after F. M. Penning, which use magnetic fields to confine the charged particle in two dimensions and static electric fields which confine in the third dimension. The other type of trap is known as a Paul trap, named after Wolfgang Paul, and it is these devices that I chose to pursue for the work described in this thesis.

In this chapter I start by showing the theory of the Paul trap and how it is able to confine charged particles. We then discuss the harmonic potential the ion experiences while being confined in the trap. Next we discuss the process of Doppler cooling and how we cool the ions in a surface ion trap. We end with a discussion of the ytterbium ion and its state diagram

2.1 Radio Frequency Paul Traps

For a charged particle to be trapped it should feel a restorative force when the partial is perturbed from its tapped position in all directions.

A positively charged particle, such as an ion, entering an external electric field will experience a force. We would ideally like to create a local electric field minima in all directions which would confine the ion to the position of that minima.

Unfortunately due to Gauss's law we know that in free space there can be no local minima or maxima to an electric field. The Laplace equation, here shown in cartesian coordinates reads:

$$\nabla^2 f = \frac{\partial^2 f}{\partial x^2} + \frac{\partial^2 f}{\partial y^2} + \frac{\partial^2 f}{\partial z^2} = 0 \tag{2.1}$$

We can see that for a solution to the equation, described as the force on the charged partial, such that the divergence of the field is zero and we can write it as follows,

$$\nabla \cdot \mathbf{F} = \nabla \cdot (-\nabla U) = -\nabla^2 U = 0 \tag{2.2}$$

where U is the electric field potential and $\mathbf{F}$ is the force experienced by the charged particle. We can see that apart from the very trivial solution of $\frac{\partial^2 f}{\partial n^2} = 0$ where n is (x,y and z) i.e no electric field, there is no minimum that can exist in free space in all spatial directions at the same time, this is known as Earnshaw's theorem.

We can, however, find a minimum in along one direction with static fields and satisfy the Laplace equation by having an suitable rotating potential along the other two directions.

We now need only to create a restorative field in the remaining two spatial directions to be able to trap the charged particle.

One method already mentioned is to create a magnetic bottle which will cause the charged particle to spiral along the magnetic field lines in two spatial directions while being "capped" in the third by static electric fields, this is known as a Penning trap [49].

It is, however, also possible to create a time varying electric field which generates an average force on any charged particle towards an effective minimum. This is a Paul trap [50].

Since the charged particle, in our case an ytterbium ion, has a finite mass and charge it will not instantaneously move when presented with an external electric field. If we generate a field that varies fast enough we can create an effective potential called a pseudopotential.

The pseudopotential is a quasi-static virtual potential that can be used to calculate the force a charged particle would feel when under the influence of that potential. The pseudopotential is derived from the motion of a charged particle in and oscillating electric potential as given by,

$$\Phi(x, y, z, t) = V(x, y, z) \cos(\Omega t) \tag{2.3}$$

where Φ is the motion, V is the RF voltage, t is time, x, y, z are the Cartesian coordinates and Ω is the angular frequency of the RF voltage.

This can be approximated to the pseudopotential as [51],

$$\psi = \frac{e^2}{4m\Omega^2} |\nabla V(x, y, z)|^2 \tag{2.4}$$

where e is the electron charge, m is the ion mass and ψ is the pseudopotential.

The pseudopotential can be combined with static DC electric potentials ($Vstatic$) to form a combined effective potential that can be used to calculate the force that a charged ion would experience under that potential,

$$F_{(x,y,z)} = ma = -e \frac{\partial \phi}{\partial(x, y, z)} \tag{2.5}$$

where,

$$\phi = \psi + Vstatic \tag{2.6}$$

and F is the force.

The simplest form of paul trap is the quadrupole trap, shown in Figure 2.1. If we imaging the charged particle in the electric field when in configuration (a) the ion experiences a force pushing it away from the top and bottom electrodes (trapping force) while feeling an attractive force towards the two side electrodes (anti-trapping force). This causes a momentum change in the ion and it travels towards the centre in the vertical direction.

Half a cycle later the fields switch such that the side electrodes are now generating the trapping force and the top and bottom electrodes are generating the anti-trapping force of Figure 2.1 (b).

Since the electric force is proportional to the gradient of the potential it is stronger the further away from the center the ion is positioned and weaker the closer to the centre it gets. If we choose from a particular set of frequencies and voltage potentials of the

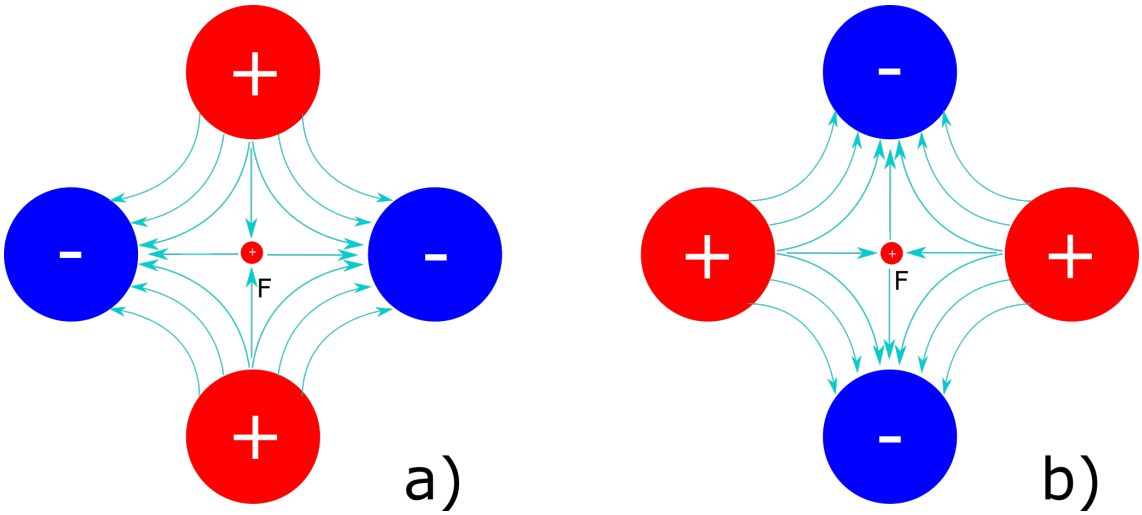

Figure 2.1: Quadrupole trap. (a) shows the RF electric fields and the force experienced by the ion when the RF electric potential is positive on the top and bottom electrodes during one half of the AC voltage cycle. (b) shows the RF electric fields and the experienced by the ion when the electrodes driven with the opposite polarity during the second half of the AC cycle.

oscillating field then the ion will move towards the centre of the trap enough that when the field switches every half a cycle the repulsive force experienced is stronger than the attractive force averaged over time. This gives a net attraction towards the centre of the trap.

The force generated by this AC electric potential confines the ion in the two remaining free spatial vectors not confined by the static electric field. There is no physical limitation to which spatial vector we can take to drive with the static DC electric potential and which two we drive with the AC electric potential, but for the remainder of this thesis we will refer to the axial direction as "z". This axial field is formed by the DC component of the trapping potentials and is named as such because the AC potentials form a cylindrically symmetric field centred along this axial vector.

The equation of motion in a quadrupole trap is well established and has been derived before by March [52] and others [53, 1]. It is governed by the Mathieu equation [54],

$$\frac{d^2u}{d\xi^2} + [a_u - 2q_u \cos(2\xi)]u = 0 \tag{2.7}$$

where u are the cartesian basis vectors (x, y, z), a_u and q_u are dimensionless trapping parameters and ξ is a dimensionless parameter given by,

$$\xi = \frac{\Omega t}{2} \tag{2.8}$$

where Ω is the angular frequency of the AC potential and "t" is time.

Solutions to the Mathieu equation can have quasi periodic results that can be found using the Floquet theorm. This gives values to the a_u and q_u which in turn determine stability regions for the Paul trap, these parameters are dependent on the voltage and drive frequency. Since with most ion Paul traps the driving AC field oscillates in the MHz range we call it the radio frequency (RF) voltage or field.

For the ion or any charged particle to remain trapped in one location the DC and RF electric potentials local minima must coexist in the same location in free space. If they are offset from each other then the DC field will drive the ions motion into the gradient of the RF potential and visa versa; this constant moving force between the DC and RF electric potentials creates micromotion which is a term given to the spiral movement of the ion.

The RF and DC electric potentials have created a potential well that the ion can be trapped within. This potential well has a few parameters that we can define such as the ion trapping frequency and the trap depth. The ion trapping frequency is the periodic motional frequency that the ion will experience when confined in the trap in that particular spatial vector which is determined by the symmetry of the trapping electrode structure, this is also known as a motional axis. For the Paul traps discussed in this thesis, one of the three motional axis is aligned along the axial vector and this typically has the lowest trapping frequency in the kHz range. The other two motional axis are the surface normal to the surface trap and the perpendicular vector to the surface normal and the axial vector. These last two trapping frequencies are typically in the MHz range. It is worth stating that for complex electrode structures the motional axis can change and are not always trivial to find by inspection alone, it is for these traps that more complicated numerical methods are needed.

The trap depth, usually expressed in eV, is measured as the potential difference between the local minima and the turning point in the effective potential when plotted away from the minima along the motional axes. As the trap will have three motional axis with potentially three different trapping frequencies, the trap will also have six trap depths, once for each direction away from the potential minima. For most simple trap geometries these trap depths are symmetrical in the axial and one radial direction. For the axial direction in-line with the normal to the surface trap we only define the trap depth

as the direction away from the trap surface as following the other direction would collide with the trap surface and as such the trap depth is much larger than the other depths so it can be ignored. This leaves us with three trap depths, one axial and two radial depths that determine the maximum energy that the ion can have to still remain trapped by the electric potential.

It is therefore important to calculate the correct DC and AC voltages for a given trap geometry, this is the subject of Chapter 3.

2.2 Doppler Cooling

Trapping an ion not only involves creating a set of electric fields necessary to contain the ion but also a method is needed to remove kinetic energy from the ion keeping it within the ion trap. Without a method of cooling the ion would slowly heat up, primarily from electrical noise perturbations, in the electrodes. If this heating of the ion brings its kinetic energy above the depth of the ion trap then the ion can be lost from the system.

We can use a process called Doppler cooling to take energy away from the ion with laser light detuned to the red side of an optical transition of the ion.

As the ion moves towards the laser the Dopper effect causes the detuned line transition of the ion to become sensitive to the detuned laser light. This allows the ion to more likely absorb the photons which gives the ion a momentum kick with a force equal to[55],

$$F = \frac{\hbar k s_0 (\Gamma/2)}{1 + s_0 + (2(\Delta_{eff})/\Gamma)^2} \tag{2.9}$$

where F is the force, $s_0 = I/I_s$ is the saturation parameter with I being the light intensity and I_s being the saturation intensity of the particular transition. Δ_{eff} is the effective detuning and Γ is the line width of the transition.

This force is directed opposite to the direction of travel of the ion causing it to slow down. The energised ion will then spontaneously emit a photon at a random direction and time, this emission also contains a momentum kick, but due to the random nature of the direction of emission the average momentum gain can be ignored as it tends to zero.

As the ion looses energy to the photon absorption and emission cycle its own kinetic energy decreases until it is of the same order as the photon moment kick. At this point the net gain in energy (absorption) and loss of energy (emission) balance out and the ion can be cooled no further by this method.

2.3 Doppler recooling and heating rate

There are quantum experiments where knowing the temperature of the quantum system is important [56, 57, 58] or the temperature of the system has a known effect such as decoherence that is unwanted and needs to be minimised. For an ion trap experiment there are a few methods for working out not only the temperature of the ion but also how well the experimental apparatus shields the ion from being heated up, this is known as the heating rate.

There are some methods such as sideband absorption [59, 60] which measures the sideband absorption spectrum to determine the heating rate. These methods are accurate to sub-motional phonon levels but they require the system to be close to the motional ground state $n \approx 0$. This rules out using these methods on ions that have even quantum numbers, and requires that we have a working sideband addressing regime which might not be the case when we are first trapping an ion on a new microfabricated ion trap.

There are methods of cooling ions down to the motional ground state using resolved sideband cooling [59, 61] which has been demonstrated on Ca+ ions [62], but this method was not used here as it was not required for characterising the microfabricated ion traps and it adds experimental complexity on top of the Doppler recooling method [63] that was used.

Under the Doppler Recooling method, the ion is cooled down for a long time period ($T >> \tau$ where T is trapping time with Dopper cooling lasers on and τ is the time period of the harmonic motion of the ion in the trapping potential) such that the system is in a steady state at the limit of the Doppler cooling regime. The cooling laser is then turned off, usually via the use of an AOM (acousto-optic modulator) such that the system is allowed to evolve and heat up for a specified time period t. After this time period has passed the laser is turned back on and the ion will undergo Doppler cooling once more.

The florescence of the ion is related to the velocity of the ion and the Doppler detuning this velocity has on the rate of photon absorption from the laser light. We can use a sensitive photon counting device such as a PMT (Photon multiplier tube) to measure over time the brightness of the ion and therefore how hot the ion became when the laser was turned back on.

The method followed for the work in this thesis is described in great detail in the paper by Wesenberg et al [46].

2.4 The Yb^+ Ion

There are many criteria when choosing the correct trapping ion. Some of these criteria are due to the ease of obtaining the element, the natural occurrence of the various isotopes, whether the sample will need enriching to favour the isotope needed and how easy it is to construct an oven capable of delivering the neutral atoms for ionisation.

The other criteria are quantum mechanical in nature. We ideally need an ion with a single outer electron to remove unwanted metastable states. The quantum qubit states of the ion need to be easily addressable with commercially available lasers and the states need to be able to perform the needed quantum operations to perform quantum computations.

There have been many successful ion candidates demonstrated such as calcium [64], barium [65] and ytterbium [4].

In this thesis we will be using the element ytterbium which has easy to address energy states, with wavelength transitions where there are commercially available diode lasers available.

Two main isotopes will be considered in this thesis, $^{171}Yb^+$ and $^{174}Yb^+$. Even isotope numbers such as 174 have no nuclear spin and therefore no hyperfine splitting of the energy states. This makes them unsuitable for quantum logic but due to the large abundance of $^{174}Yb^+$ (31.84%) in natural ytterbium and that due to the lack of hyperfine splitting it is experimentally easier to trap, $^{174}Yb^+$ is my first choice when trapping on a new ion trap. $^{174}Yb^+$ forms the main isotope used for performing heating rate measurements in Chapter 5.9.

2.4.1 Photo-ionisation

To remove a single outer electron we use two lasers to perform a two stage ionisation process [4, 2, 3]. Figure 2.2 shows a simplified ionisation diagram for the Yb atom.

A single laser can be used at 199 nm wavelength but these lasers are expensive and this method does not allow for isotope selection. So we choose to use two lasers a 399 nm to move the electron into the $^1P_1$ state, then a second 369.5 nm to remove the electron. The 369.5 nm laser is also used for fluorescence detection, laser cooling and state preparation.

2.4.2 $^{174}Yb^+$ Energy level structure

Figure 2.3 shows the optical transitions of $^{174}Yb^+$. The three principle laser wavelengths are shown, 369.5 nm, as already mentioned, is used for second stage ionisation, state detec-

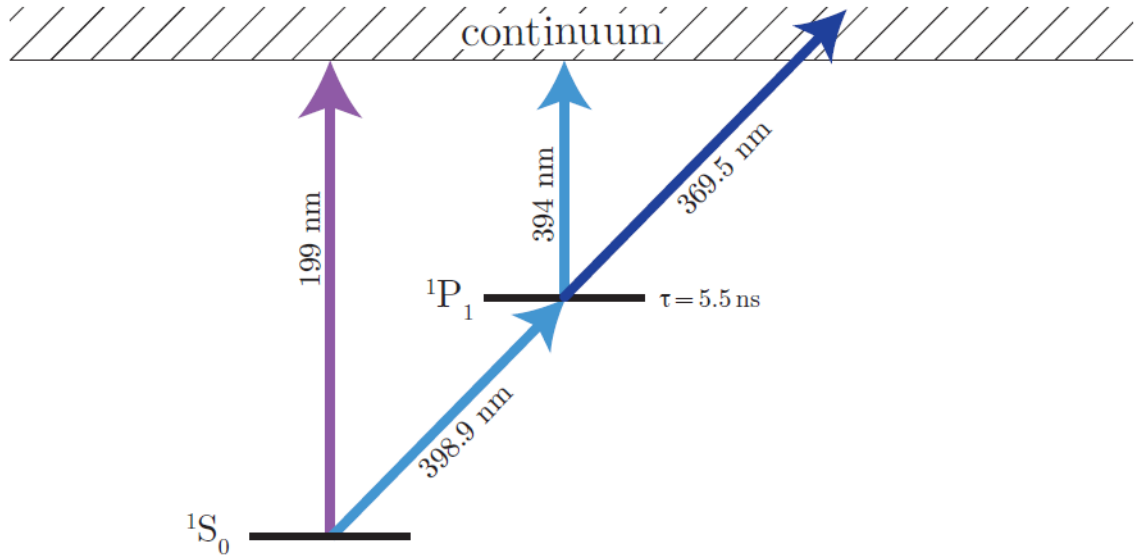

Figure 2.2: Simplified energy diragram for a Yb atom showing both single and double photon ionisation[1, 2, 3]

.

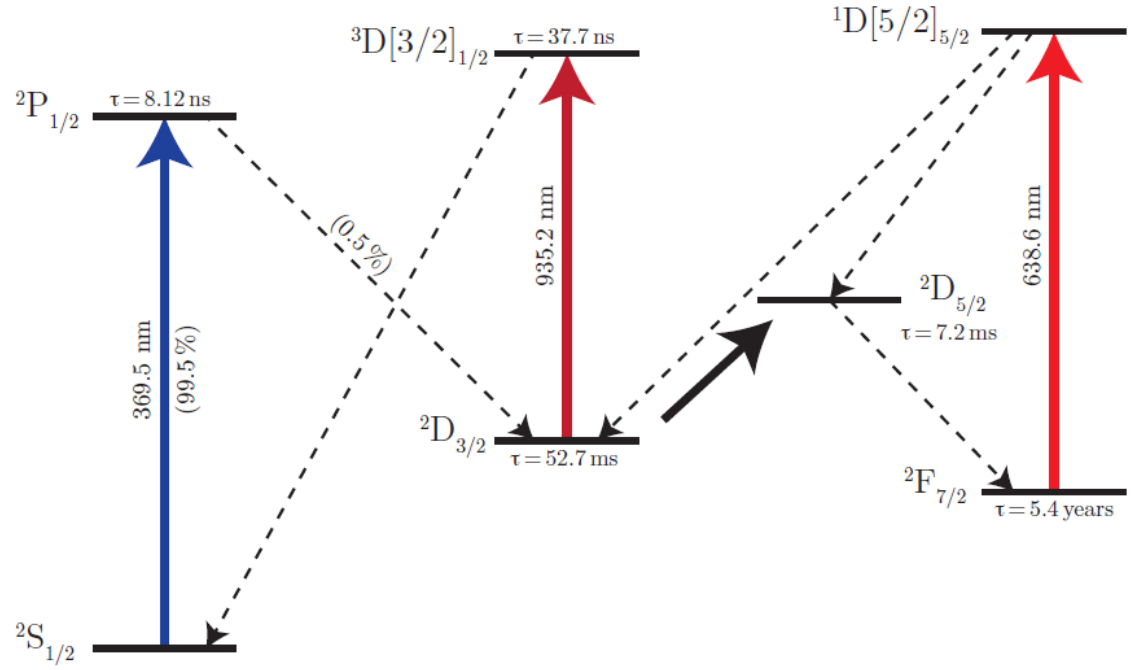

Figure 2.3: Energy state diagram of $^{174}Yb^+$ shown are the three principle laser wavelengths and state life times. The dashed arrows show optical transitions where the solid arrow shows a transition mediated by high energy collisions [4, 1, 5, 6, 7, 2, 8]

.

tion and Doppler cooling. 935.2 nm is used for optical pumping back to the $^2S_{1/2} \Rightarrow ^2P_{1/2}$ transition. The 638.6 nm laser is used to bring the ion back from the $^2F_{7/2}$ state, which

has a very long half-life on the order of years [66].

2.4.3 $^{171}Yb^{+}$ Energy level structure

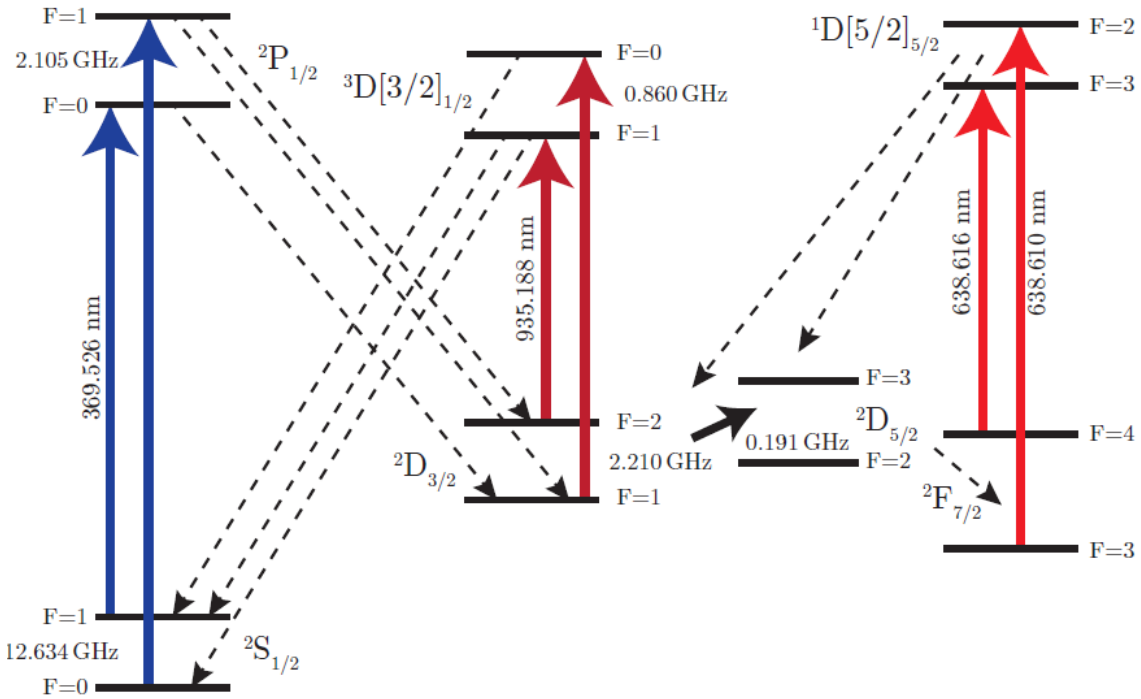

Figure 2.4: Energy state diagram of $^{171}Yb^{+}$. Shown are the hyperfine states caused by the nuclear spin. Also shown are the frequencies of the hyperfine splitting in GHz [4, 1, 5, 6, 7, 2, 8]

.

Figure 2.4 shows the state diagram of the $^{171}Yb^{+}$ ion. Shown is the hyperfine splitting caused by the odd isotope having a nuclear spin. The $^2S_{1/2}$ clock state has a frequency splitting of 12.634 GHz and forms the basis for a hyperfine qubit[53, 42]. The form of qubits we choose to develop in our lab is with the application of microwave radiation and magnetic field gradients [67, 68]. The microwave radiation used is tuned to the 12.634 GHz hyperfine transition. The 2.105 GHz splitting on the $^2P_{1/2}$ energy state is addressed with an electro optical modulator (EOM) on the 369.5 nm laser. The 2.210 GHz splitting on the $^3D_{[3/2]_{1/2}}$ state is driven by power broadening the line transitions, this is achieved by increasing the flux of the the 935.2 nm laser light by at least five times the saturation parameter, how much over saturation is not very critical as long as both transitions are covered. High flux 935.2 nm laser light, also, does not cause charge build up on the surface traps as the wavelengths is below the ionisation energy of gold surface electrodes, so the beam size is not critical. A good description of the quantum logic operations and the

quantum gates we aim to create can be found in the thesis by Joe Randall[42] and the works of others [69, 70] from which our work is derived.

Chapter 3

Field Simulation Toolkit

Since we need to test and refine ion trapping parameters such as applied DC voltages and RF electric fields it is useful to be able to simulate those fields and calculate their effects on the ion's motion.

This is especially important when the ion trapping system will be used for testing different trap geometries and materials which will drastically alter the local electric field patterns.

Also, since the cryogenic system is designed for rapid trap testing and deployment, it is important that the path from trap design to calculated parameters be as swift, and require as little human input as possible, to minimise the turnaround time of trapping and optimisation on different trap designs.

In this chapter a description of computational methods for electromagnetic field simulations will be discussed. A comparison between different approaches that can be used with their strengths and weaknesses will also be shown.

Following this, a description of the existing field solver simulation method, previously used by our group, will be given along with the issues that arise from using this method. A new method is then given, based on the "ScuffEM" solver.

This new approach is experimentally validated in Chapter 5.9 but the accuracy results are also given here to justify the new tool path. .

3.1 Computational methods for electromagnetic field simulations

As computers have increased in computational power and storage, there has also been much research and development into new methods for calculating physical properties of objects in software.

Everything from heat flow and fluid dynamics to material stresses and electromagnetic fields have been modelled in software to aid in the design and testing of physical systems.

For ion trapping, the physical system we wish to solve for is the electromagnetic (EM) field, in particular the electric fields around the surface electrodes of an ion Paul trap. Since we will be shuttling adiabatically well into the slow regime where the rate of shuttling is much slower than the ions vibrational trapping frequency and the RF drive frequency; we can treat the RF field as static when computing the pseudopotential with appropriate scaling and the DC potentials calculated can be considered static. To calculate the EM fields we need to solve Laplace's equation.

There are two broad classifications of methods used for solving the EM fields: analytical methods and numerical methods[71].

Analytical methods include,

1. Separation of variables [72]
2. Series expansion [71]
3. Conformal mapping [73]
4. Integral solutions, such as Laplace and Fourier transforms [71]
5. Perturbation methods [71]

these methods yield exact solutions to the Laplace equation. In the cases of series expansions, infinite series must be used otherwise they will only approximate solutions. They are, however, limited to simple problems or a particular subset of physical systems. For example the gap-less approximation demonstrated by Oliveira and Miranda[74] and by House[75] is an analytical method for solving the electric field pattern above the surface of an ion Paul trap. The method used during this thesis comes from the paper by House. The gapless approximation method used by House, treats each electrode as a rectangle with a voltage potential applied and no gaps in between adjacent electrodes. This method gives

reasonable results for solving the required DC and RF electric fields, has been demonstrated [44] and was also used on the Cryogenic system as a baseline comparison for the other more complex methods.

Numerical methods include,

1. Finite difference method [76]
2. Method of weighted residuals [77]
3. Moment method [78]
4. Finite element method [79]
5. Transmission-line modeling [80]
6. Monte Carlo method [81]
7. Method of lines [71]

these methods work by finding approximations to the physical system, this is useful when the partial differential equations cannot be easily linearised to use the analytical methods. These approximations can be refined to give a result that conforms with a required accuracy to the physical system. Numerical methods are generic and can be applied to most physical systems but there are distinct advantages and drawback to each method.

3.1.1 Integral and Differential Forms

Before solving EM problems it is often helpful to sub-categorise them into their integral or differential forms. We can define an operator equation for describing the problem to be solved as[71],

$$L\Phi = g \tag{3.1}$$

where g is the known excitation source, L is the operator that can be either in the integral, differential or mixed form and Φ is the unknown function to be determined.

For solving electrostatics we can use the Poisson equation. Substituting in $\Phi = V$, $L = -\nabla^2$ and $g = \frac{\rho_v}{\epsilon}$ gives the Poisson equation,

$$-\nabla^2 V = \frac{\rho_v}{\epsilon} \tag{3.2}$$

where V is the voltage potential, $-\nabla^2$ is the Laplacian operator, ρ_v is the volume charge density and ϵ is the volume permittivity. This is the differential form of the operator equation for electrostatics.

We can also express this equation in integral form as[1],

$$V = \int \frac{\rho_v dv}{4\pi\epsilon r^2} \tag{3.3}$$

where the substitutions were $g = V$, $\Phi = \frac{\rho_v}{\epsilon}$ and $L = \int \frac{dv}{4\pi r^2}$.

The numerical methods previously mentioned are categorised by the method used for the operator equation. The two methods that have been used before [82] are the Finite Element Method (FEM) which uses the operator equation in its differential form and the Boundary Element Method (BEM) which uses the integral form of the operator equation [83].

3.1.2 Discretization

To solve these large complex EM systems numerically we need to convert the partial differential equations (PDE) that contain multivariable functions and their partial derivatives into multiple small regions that can be approximated by ordinary differential equations (ODE) which can be solved analytically. The process of splitting the problem into small regions is called discretization[71, 83].

With FEM the problem is discretized by volume. Figure 3.1 shows three types of discretized mesh for a FEM linear ion trap, the figure shows a two dimensional slice to aid in visualising the mesh.

FEM requires the discretization of the whole domain where electric field data is required. For this reason FEM cannot handle open domains or regions outside the closed domain. This requires a virtual boundary to be created at a distance from the region of interest where we can apply appropriate boundary conditions such as a perfectly matched layer (PML) where the electric field vector is continuous and smooth across the boundary, or put another way, any EM wave impinging on the boundary suffers no reflection back into the non-PML region.[71].

FEM tends to result is non-smooth results between data points along the mesh[83]. This non-physcial result can be improved by increasing the mesh density as shown in (b) of Figure 3.1. Increasing the mesh uniformly to such a high order, however, increases the

[1] Under Spherical Coordinates

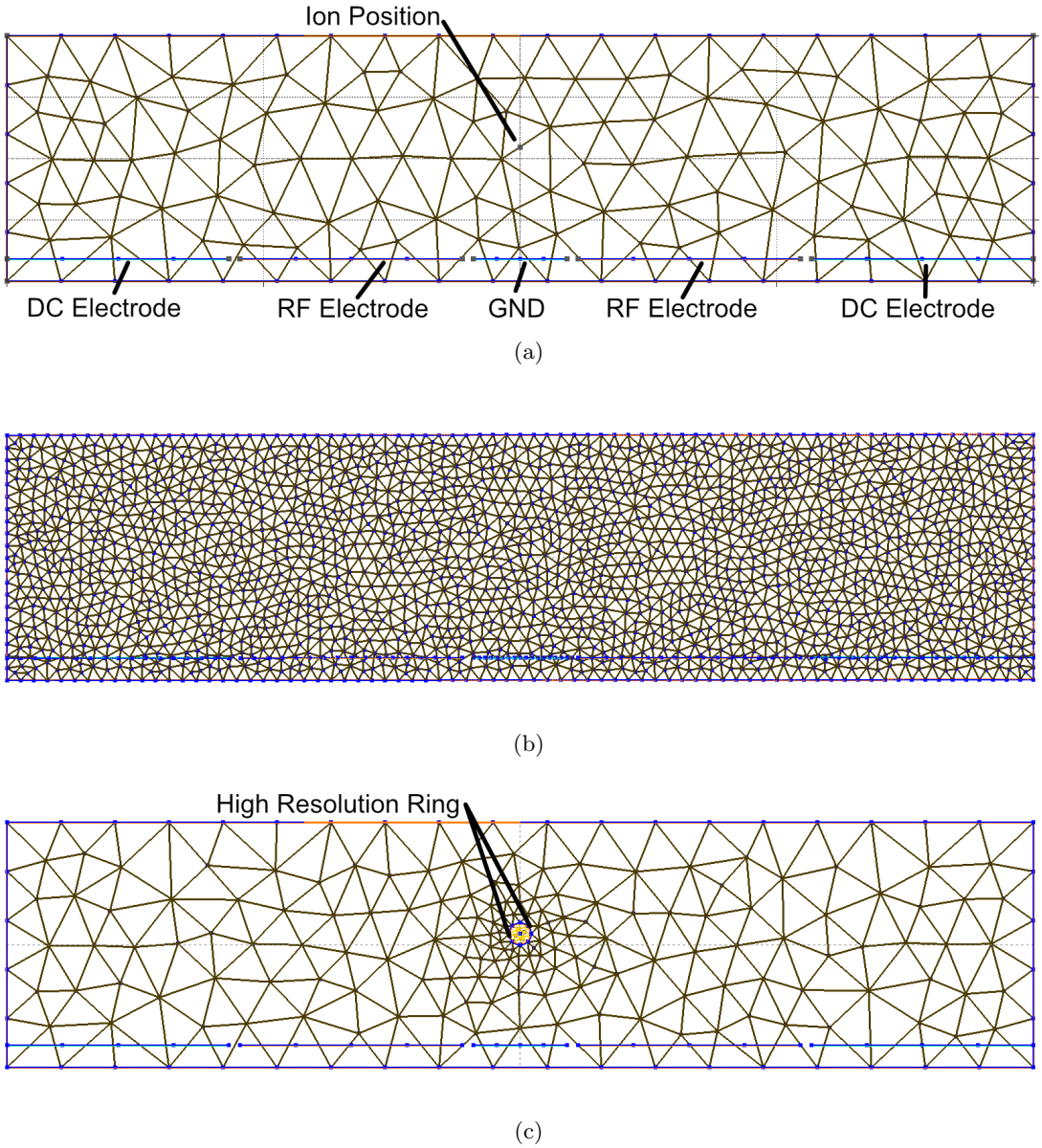

Figure 3.1: (a) shows a two dimensional slice of the three dimensional FEM discretized mesh at low resolution (323 elements). (b) shows a uniform high resolution mesh (3946 elements). (c) shows the use of a high resolution ring to aid in directing high resolution mesh generation at the predicted position of the ion (471 elements).

computational time for a solution. In the example shown in Figure 3.1 (b) the solution took over two hours to complete using the Comsol software suite.

An alternative approach is to selectively refine the mesh generation to a region of interest using a non-physical primitive such as a cylinder which forces the mesh to be refined in a local region but is not physically present and takes no part in the field solving step. Figure 3.1 (c) shows an example of this refinement which was then solvable within

15 minutes with the same local accuracy as the global refined mesh (b).

Since FEM discretizes a region by volume it is able to handle inhomogeneous volumes such as complex dielectrics and boundaries between different volume media. It is also able to manage dielectrics in an ion trap and is useful for calculating the trap capacitance and loss tangent within a microfabricated ion trap before manufacturing.

Given that the important region of a typical surface ion trap is dominated by the volume of free space between the trap surface and the ion compared to the volume of the trap structure FEM solvers tend to give poorer results compared to BEM solvers for the same problem[82].

In a BEM solver only the boundaries of the bodies in the region of interest are meshed. Figure 3.2 shows the same simple linear ion trap that was used in the FEM example meshed for a BEM solver. As can be seen only the boundary surfaces are meshed and the volumes are not. This allows BEM solvers to work with open domains and regions that extend to infinity without the need for creating arbitrary volume meshes[83].

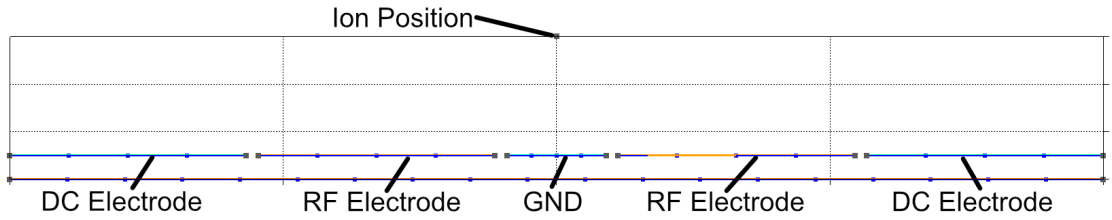

Figure 3.2: A two dimensional slice of the three dimensional BEM discretized mesh. Only surfaces are meshed in a BEM problem. Shown are the DC electrodes, RF electrodes and centre ground.

BEM solvers are also better at handling the derivatives of the field function such as stesses, fluxes or moments. BEM is also able to generate the field data and its derivatives at any point in the domain of the problem unlike FEM which can only generate data at the nodes of the mesh[83, 82]. This ability to calculate the field data at any point is crucial when attempting to calculate RF field nulls when optimising the trapping DC values and when attempting trajectory simulations.

3.2 Ion Trap Electric Field Solving

Until recently a program called BEMSolver was used to calculate the trapping fields of the microfabricated ion traps.

BEMSolver, created by Singer *et al.* [82], is a BEM solver for arbitrary geometries and runs in a ROOT environment which was created by CERN [84].

BEMSolver can read trap geometries from *.dxf files. one of the standard file types used in AutoCAD™, the program used to design our microfabricated ion traps.

Figure 3.3 shows the BEMSolver workflow. After importing the BEM geometry. the BEMSolver program generates the surface mesh and solves the electrostatic field potential at an array of points above the trap's surface, saving the potential data into a *.dat file. These *.dat files are then loaded into a Mathematica™sheet where the static electric potential data is interpolated and the partial differential is calculated to generate a ponderomotive potential. This ponderomotive potential is then used to calculate the RF null position for this particular trap geometry and if new electric field data is needed a new set of data points is generated with the BEMSolver by editing the BEMSolver files. If the geometry needs altering, for example to change the ion height or trap depth for a given electrode potential, then the original *.dxf files need to be manually altered and the process starts from the beginning.

This process is completely manual and requires the editing of *.cxx files that necessitates programming experience. Also in 2017 the BEMSolver download link was retired so it is not currently possible to download the solver package.

To this end it was decided that a new solver workflow was needed, built around a BEM solver engine which was well documented and could be modified to allow for an automatic work flow. As an extension goal the new solver should also allow for optimisation routines to be created and direct control of the DC voltages on an experiment that would yield the required DC and RF electrical potential minima for a stable trapping region.

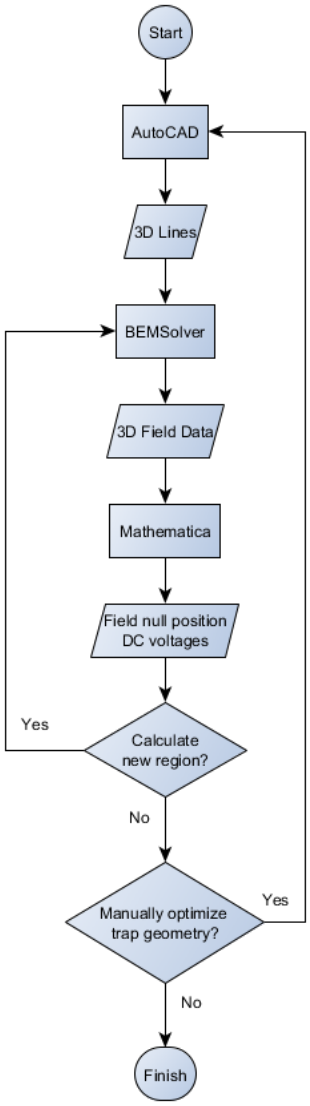

Figure 3.3: Workflow for the BEMSolver field solver. This is a manual process that starts by importing the *.dxf output geometry files from AutoCAD™and converting them into 3D lines that represent the outer bounds of the electrodes, then importing those lines into BEMSolver where the electrostatic field at defined points above the surface of the trap are calculated and saved into *.dat files. The *.dat files are then loaded into Mathermatica where the ponderomotive potential is calculated so that we can solve for the ions position and calculate DC values. If new field data is required or the trap geometry needs altering the original *.dxf files are altered then reimported into BEMSolver.

3.2.1 ScuffEM

It was decided that ScuffEM, created by Homer Reid [85, 86], which is an open source, well documented and actively developed BEM solver, would form the core solving engine

of our new workflow.

ScuffEM has a few features that are desirable for ion trap design and extend what was capable with BEMSolver. ScuffEM can handle arbitrary meshed geometries by either Gmesh or Comsol meshing engines. ScuffEM is capable of RF and DC source field solving, so high frequency components such as RF or microwave antennas could be designed within ScuffEM. ScuffEM is also capable of calculating complex multi-layered implicit dielectric layers quickly under the approximation that each layer extends to infinity and only has a defined thickness, this approximation is valid for most ion trap designs as the total microfabricated thickness is around 600 µm with a length and width of 10 mm.

The first step was to test the accuracy of ScuffEM against the gapless approximation. While a gapless geometry is not physically realisable it does allow us to compare the accuracy of the numerical BEM method.

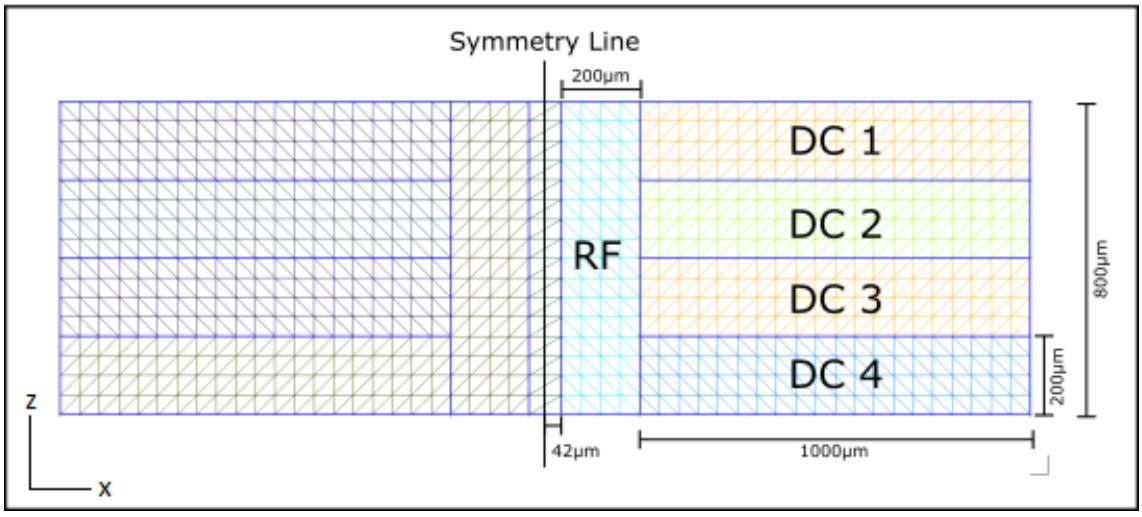

Figure 3.4: Meshed ion trap design with no gaps between electrodes. Since this layout is symmetrical along the z axis computational time can be reduced by defining a symmetrical boundary at this midpoint.

Figure 3.4 shows the layout of a simple surface linear ion trap with no gaps between the electrodes. This same layout was also modelled by the potential distribution of a rectangular electrode in the gapless approximation [75],

$$\phi(x,y,z) = \frac{V}{2\pi}\left\{ \arctan\left[\frac{(x_2-x)(z_2-z)}{y\sqrt{y^2+(x_2-x)^2+(z_2-z)^2}}\right] - \arctan\left[\frac{(x_1-x)(z_2-z)}{y\sqrt{y^2+(x_1-x)^2+(z_2-z)^2}}\right] - \arctan\left[\frac{(x_2-x)(z_1-z)}{y\sqrt{y^2+(x_2-x)^2+(z_1-z)^2}}\right] + \arctan\left[\frac{(x_1-x)(z_1-z)}{y\sqrt{y^2+(x_1-x)^2+(z_1-z)^2}}\right]\right\} \tag{3.4}$$

,

where (x_1, z_1) and (x_2, z_2) are the Cartesian coordinate pairs of the two diagonal corners of each electrode and (x, y, z) are the coordinates to solve the electrical field potential for. V is the voltage applied to the electrode.

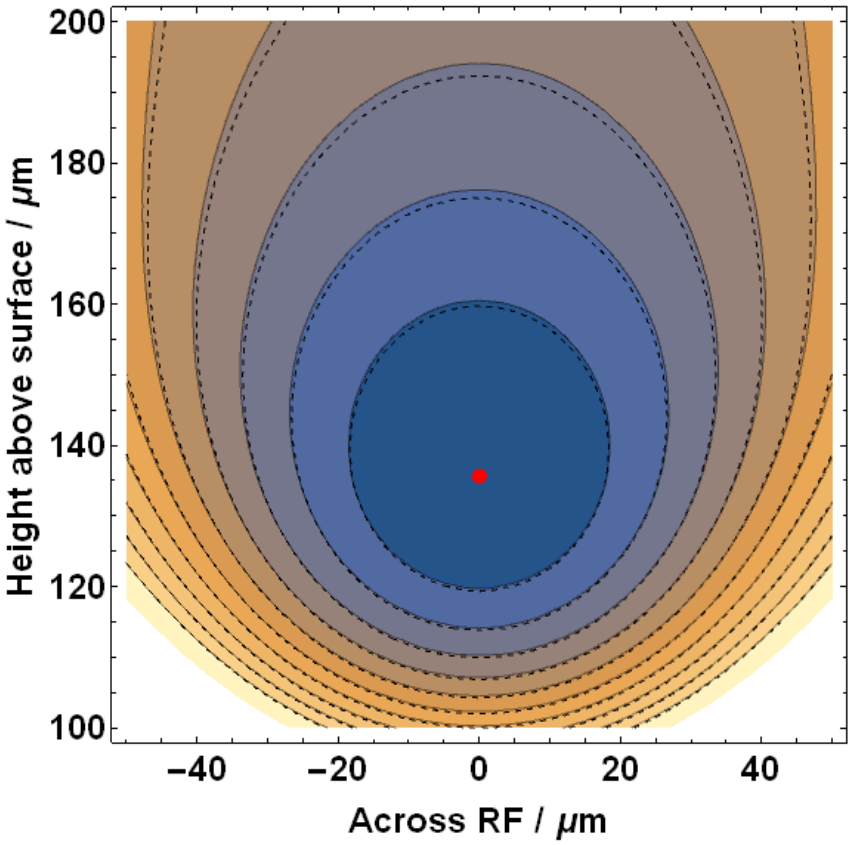

Figure 3.5: Plot of the ion trapping position from the RF electrode electric fields. The dashed line contours are the gapless approximation result, the solid line and colour contours are from ScuffEM. Calculated ion height of 135.6 µm for the gapless approximation, 136.1 µm for ScuffEM. Red dot represents the ion position by gapless approximation.

As can be seen from Figure 3.5, the ScuffEM solver gives an ion height of 136.1 µm compared to 135.6 µm using the gapless approximation method3.4. Comparing the two

methods gives an error in the ion height of 500 nm, this is primarily caused by the gapless approximation method treating all areas as grounded electrode outside the defined regions, where ScuffEM treats all non-defined areas as vacuum. ScuffEM can give more accurate result by adding a ground plane outside the electrode layer, but this increases computational time. Total simulation time for this structure was 4.68 s.

In Chapter 5.9 more detail will be given on the trapping parameters but a brief example will be given here to demonstrate the accuracy when modelling with the ScuffEM solver work flow. A 150 µm ion-height linear sapphire surface trap was modelled using the ScuffEM solver which resulted in a simulated ion height of 157 µm. RF and DC values were calculated from the field simulation to give a 0.5 eV RF trap depth (Radial) and 0.1 eV DC trap depth (Axial). RF peak voltage of 213 V at 21.3 MHz was calculated. DC voltages of DC1 = 5.83 V, DC2 = −4.26 V, DC3 = −4.26 V and DC4 = 5.83 V were also calculated, where DC1-4 are using the name nomenclature as in Figure 3.4. The measured axial secular frequency for this trap was 166.5(1) kHz, the two other axial frequencies were 1.023(1) MHz and 1.224(1) MHz.

After trapping and micromotion compensating applied DC voltages the final trapping parameters were measured and are given in Table 3.1.

	ScuffEM Simulated	Measured
Ion Height	157 µm	156(2) µm
RF Voltage (for 0.5 eV trap depth)	213 V	207(5) V
DC1,4	5.83 V	5.76(1) V
DC2,3	−4.26 V	−4.34(1) V

Table 3.1: Table of a 150 µm surface ion trap with sapphire substrate, comparing simulated parameters values to measured values after micromotion compensation.

As can be seem from Table 3.1 the simulated values are close to the measured ones for the trap in question. The next step was to automate as much of the new work flow as possible.

3.2.2 LIBSCUFF

It was decided to create a wrapper c++ program that would call the ScuffEM API libraries (LIBSCUFF). This program would perform the following steps automatically,

1. Read *.dxf layout.
2. Mesh electrodes.
3. Call LIBSCUFF and calculate electric fields.
4. Export intermediate files for field viewing.
5. Calculate pondermotive potential and find RF null.
6. Calculate DC voltages for required trap depth.
7. Export results.

with optional extra steps,

1. Perform ion trajectory simulation.
2. Calculate the required DC potential changes over time to form voltage ramps for slow adiabatic shuttling.
3. Directly control a custom voltage source that drives the electrodes.

Additional design requirements include using libraries that have minimal dependencies to keep the build chain as simple and possible to aid in debugging compilation errors. The program should also be modular so that each step can be performed and tested without requiring the completed program this allows the user to choose what steps are required.

3.2.3 Reading from *.dxf

The AutoCAD™trap layouts are two dimensional layer structures defined by 2D line loops. It is therefore necessary to create a layer definition file for the trap layout that will define the vertical layer structure.

Listing 3.1: Layers.txt - required file

```
GND 0,0
RF* 100,1
DC* 100,1
```

Listing 3.1 shows an example "Layers.txt" file, the first name on every line is the same as the layer name in AutoCAD™. If a "*" is added after the name then this acts as a whildcard and includes all layers with the same starting string, for example RF* includes

RF1,RF2...RFn. The first number in each line after the space is the height, in microns, for that layer. The second number is a flag to set that layer as an "active layer". Any layer that is active is simulated by applying 1 volt to the electrode while all others are grounded. Deactivated layers are always grounded. After all active electrodes are simulated the electric field data can simply be scaled by a multiplier voltage later in the work flow.

Dielectrics are named separately as the method used by ScuffEM for multi-layered implicit dielectrics only allows for infinite long and wide layers so no surface geometry is needed from AutoCAD™.

Listing 3.2: Dielectrics.txt - optional file

```
Sio2  0,100,3.9,1
```

Listing 3.2 shows an example "Dielectrics.txt" file where the first name becomes the layer tag name for the output data, it is only used for this purpose. The first and second numbers are the starting layer height and ending layer height respectively. For a multi-stacked dielectric the starting height of successive layers should equal the ending height of the previous layer. The third number is the relative permittivity (ϵ_r), in the example given it is 3.9 for silicon dioxide. The last number is the relative permeability (μ_r).

To load the *.dxf file we use "dxflib" by RibbonSoft as it is "light weight" and doesn't rely on any other external dependencies. We create a class ("FileLoader") to load the layers from the *.dxf file and also load the layers expected from the "Layers.txt" file. We then cycle through the layers loading the "DL_POLYLINE" data as triplets for the starting and ending coordinates for each line segment forming a closed loop, there must only be one closed loop for each layer. This closed loop is then defined as an "EL" class for electrode with the same name given in "Layers.txt".

3.2.4 Mesh electrodes

To handle the meshing of the electrodes we call the Gmsh library "gmsh.h". We add each electrode ("gmsh::model::add($< ELname >$)") and draw the points and then lines to form the electrode in the Gmsh format. ScuffEM can either accept separate meshes for each electrode or a single mesh with physical groups. To reduce the number of files needed and to make the file strucure cleaner, it was decided to go with a single mesh file

with named physical groups. The mesh density is set to an average of 20 elements along the width or length which we found gave good accuracy results in ScuffEM.

3.2.5 Call LIBSCUFF

Now that we have the meshed intermediate file with the assigned physical groups for each electrode we call LIBSCUFF to calculate the surface charge density and build the Greens function for each active electrode set at one volt and all other electrodes set to zero volts. This results in multiple intermediate files which are saved to a "cache" folder so that running the program again with an unaltered *.dxf file will load the pre-calculated BEMMatrix which results is faster field computation.

Now that the BEMMatrix from LIBSCUFF has been generated we can either export a set of field datapoints for loading into Mathematica™or allow our program to continue calculating the pondermotive potential and the ion trapping position. To calculate the gradient of the electric field we use,

$$f'(a) = \lim_{h \to 0} \frac{f(a+h) - f(a)}{h} \tag{3.5}$$

which is the right-handed form where a is a position in space above the trap electrodes in three dimensions, $f(a)$ is therefore the electric potential calculated by ScuffEM at position a and h is a small step in one of the Cartesian directions. The smaller the step size the higher the accuracy of the gradient, within the limitations of floating point precision on a domestic AMD64 instruction set computer. A value of 0.5 (500 nm) is used and gives an accurate enough result without taking too long to complete when taking multiple measurements over a given volume or vector such as the axial line of symmetry. By minimising this function we find the local minima of the field which requires us to make an estimate for the starting position of the iterations.

Once we have a ion position from the RF field data we analyse the DC field data first by setting the negative voltages to a fixed value (-1V). Then we step the positive voltages up from 0 V in 1 V steps until the the electric potential at the previously calculated position becomes positive. The step size is then halved and the positive voltage is lowered with this new step size. This process continues until the step size is less than 305 µV as this is the accuracy limit with out 16bit custom voltage out card.

With the DC and RF starting values calculated we then load "State.txt" which contains the ion mass (mass number), RF frequency (in MHz) and required RF trap depth and DC trap depth in electron volts.

Listing 3.3: State.txt - required file

```
mass 174
freq 21.4
RF 0.5
DC 0.1
```

Listing 3.3 shows an example "State.txt" file for a Yb^{174} in an ion trap driven by a 21.4 MHz source. The goal trap depths are 0.5 eV for the RF and 0.1 eV for the axial DC.

It is now that we have all the data required for trapping. The data is exported to a "Results.txt" file that contains the four electrode trapping voltages and the RF voltage and frequency. This program has been used to trap successfully on the cryogenic system which is covered in Chapter 5.9.

3.2.6 DC Voltage Control

We built a custom 80 channel 16-bit digital to analogue card for the cryosystem that is covered in Chapter 4. This card in controlled by the computer using an FTDI FT4222H interface chip that can be programmed using available C++ libraries, "FTD2XX.h" for low level control such as power saving and data flow control and "LibFT4222.lib" for Serial Peripheral Interface (SPI) data for programming the two 40 channel DACs.

There are two modes that the voltage control software can be switched. In static mode the program reads a "Voltages.txt" file which contains the fixed voltages for any output pin from the DAC board. Listing 3.4 shows an example "voltages.txt" file where four pins are defined with their voltages. Any pins not defined default to zero volts.

Listing 3.4: Voltages.txt - required file

```
pin17 4.22
pin9 -2
pin44 -2
pin50 4.22
```

3.2.7 Trajectory simulator and shuttling

Following the work of Singer[82] we also developed a trajectory simulator and shuttling ramp generator for use with LIBSCUFF. To control the voltages ramps for the purpose of shuttling slowly ($\ll$ axial secular frequency) we have to solve the DC potential for multiple steps along the trap axis from a given start to end point. Given the limitation on DC voltage level, accuracy and bandwidth (which is limited by our DC filtering) we have to solve the voltages for multiple electrodes such that any step in the voltages is smooth and slow enough for our limited bandwidth (50 kHz).

This class of problems is known as an inverse problem where we try to solve for the voltages of each electrode U_j where the total potential $\Phi(x_i) = \Phi_i$ is a superposition of the field Φ_i at each position x_i along the shuttling direction such that,

$$\Phi_i = \sum_{j=1}^{N} A_{ij} U_j, i = 1, ..., M \tag{3.6}$$

where N is the total number of active electrodes, M is the number of step points along the shuttling axis and $A_{ij} = A(x_i, j)$ is a unit-less matrix of voltage potentials along the shuttling axis at positions x_i for each electrode U_j where the electrode is held at 1 V while all other electrodes are set to 0 V.

Since M is much larger than N for most microfabricated ion traps, the matrix inversion tends to lead to diverging solutions[82] due to singularities in the inverse of A_{ij}. The solution is to use the Tikhonov regulation method[87]. This modified method has been fully implemented already by Singer[82] in the SVDREG numerical package which was added to the trajectory simulator and shuttling program. With this package we can solve for a harmonic potential along the shuttling axis $\Phi(x) = a(x - x_0)^2$ where a is the potential well curvature and x_0 is the required ion position. x_0 can be stepped through time to generate simple shuttling ramps.

The trajectory simulator is based on the very common Störmer-Verlet method used by many trajectory solvers and molecular dynamics programs[88]. For the ion in an electric field the second order ODE is,

$$\ddot{q} = F(q) \tag{3.7}$$

where $F(q)$ would represent the force on the ion in the electric field at a given position q and $\ddot{q}$ is the acceleration. If we define $v = \dot{q}$ and $\dot{v} = F(q)$ then v would be the velocity. If we define h as the step size for the trajectory solver and substitute,

$$v_n = \frac{q_{n+1} - q_{n-1}}{2h} \tag{3.8}$$

into the two step Störmer-Verlet equation,

$$q_{n+1} - 2q_n + q_{n-1} = h^2 F(q_n) \tag{3.9}$$

we get two equations,

$$\begin{aligned} q_{n+1} &= q_n + h\left(v_n + \frac{h}{2}F(q_n)\right), \\ v_{n+1} &= v_n + \frac{h}{2}\left(F(q_n) + F(q_{n+1})\right) \end{aligned} \tag{3.10}$$

where v_n and q_n are the velocity and position at step "n" respectively. v_{n+1} and q_{n+1} are the velocity and position at the next step respectively. For our program we use the C++ library ODEINT which contains multiple built-in stepper algorithms with an easy callable class structure.

Since the DC electrodes are not necessarily connected to the same numbered DC wire from the DAC board we need to let the program know the mapping of the DAC channels to electrodes. In static mode that was mentioned before, the "Voltages.txt" file defines fixed voltages for given wires.

When the voltage generator is used in dynamic mode, however, we must supply a full mapping of each electrode to each wire in shuttling order. Reversing the shuttling order reverses the shutting direction so either direction can be given. Listing 3.5 shows an example mapping file for a 12 electrode linear surface ion trap. Each pair of pins represents a pair of electrodes either side of the RF lines in the same axial position. When the program runs either a static position can be given at any pair position (1,2,3...) or a min-max position and a shuttling rate can be given to perform shuttling. All voltage ramps are stored in the "cache" folder as *.dat files.

Listing 3.5: Mapping.txt - required file

```
pin17 pin9
pin44 pin22
pin16 pin74
pin12 pin66
pin33 pin47
pin51 pin67
```

By utilizing the shuttling ramp generator and trajectory simulator I was able to do simple shuttling on the cryogenic system while simultaneously viewing the virtual trajectory on the main pc. This was performed within the first few hours of trapping. The benefit of this method is to allow for quick assessment of the trap quality, for example missing connections and floating electrodes, by checking for deviations to the trajectory path on the EMCCD camera. Details from the experiment are given in Chapter 5.9. We hope to, in the future, use this method to characterise complex junction traps and perform shuttling across electric field barriers in trap-to-trap shuttling by extending the software's capabilities.

3.3 Conclusion

I have compared briefly in this chapter the differences between FEM and BEM numerical solving methods.

I discussed the previous BEM solver, BEMSolver, that was used to simulate the electric fields above the surface ion trap.

I have showed the motivation to create a new BEM solver work flow based on ScuffEM, that is almost fully automated with added features such as dielectric modelling and automatic trapping parameter generation. This will allow us to simulate new designs rapidly along with the crygenic system that allows for rapid chip testing.

I also showed the creation of the shuttling ramp generator and coupled trajectory path simulator using the Störmer-Verlet method.

Chapter 4

Experimental Setup

Due to the fact that ions are light and charged particles they can be manipulated very easily with applied electromagnetic fields. These applied fields can be intentional - trapping and shuttling fields for example - but they can also be unwanted, for example noise or charge buildup on dielectric surfaces. It is for this reason that we need to control the environment that the ion is positioned within very precisely, and all effort must be made to ensure best practices for noise control and minimisation are employed.

We need to construct a vacuum system that is able to maintain the low pressures and low temperatures that we will need when performing trap characterisation. In this chapter we will focus on the external apparatus that is needed to perform this characterisation task, and in the next chapter we will focus on the internal components. Figure 4.1 shows an overview of what will be covered in this chapter.

This chapter will cover the laser setup that generates and controls narrow bandwidth lasers to give the precise wavelengths that are used to ionise, Doppler cool and manipulate the ions, in section 4.1. These lasers consist of three principal wavelengths (369.5 nm, 935.2 nm, 399 nm) which are generated by two diode lasers and one diode pumped Ti:Sapphire laser.

One of the lasers used for fluorescence needs to be controlled precisely in both frequency and amplitude, for this laser we need to create a double pass acousto-optic modulator (AOM) setup followed by an electro-optic modulator (EOM). This setup allows us to use a single laser for multiple systems simultaneously as we gain amplitude and frequency independence through the AOM and EOM. This will be covered in section 4.2.

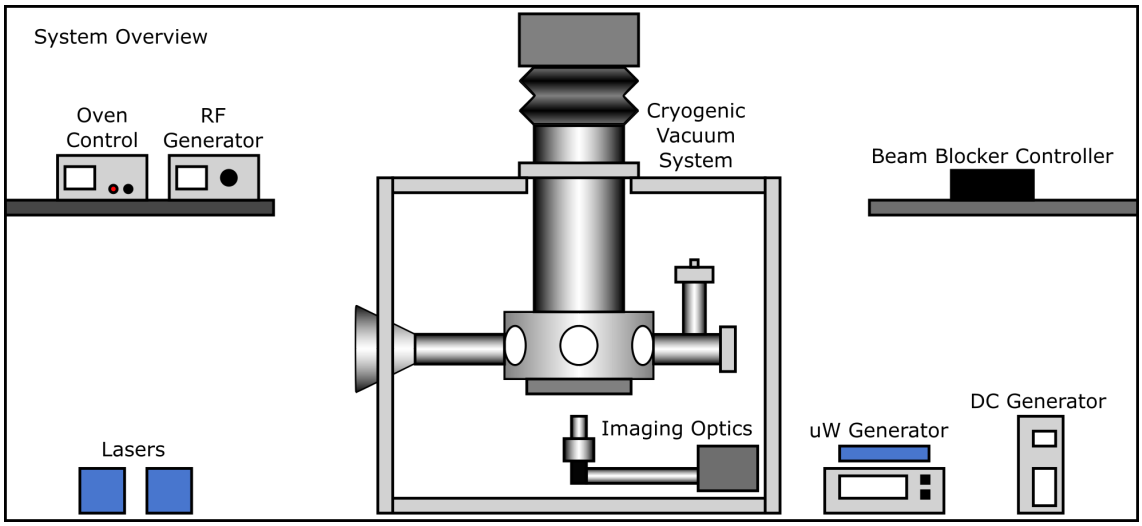

Figure 4.1: Overview of the hardware that will be covered in this chapter, the cryogenic vacuum system will be covered in Chapter 5.

The three lasers also need to be locked to the wavelengths of the internal states of the ion. There are three principal locking mechanisms used in the cryogenic setup and these will be covered in section 4.3.

Due to the mounting height of the vacuum chamber, it is necessary to create a launching platform for the laser optics before entering the system. This requires the use of an upper and lower optics table, these optical tables will be covered in sections 4.4 and 4.5 respectively.

The ion emits light by fluorescence at an emission rate of approximately 20 MHz. This light needs to be collected efficiently and imaged. This requires the use of optics and filters with a camera that can measure low photon counts (100's of photons). For some experiments the use of a Photon-multiplier tube is required for counting photons. These pieces of equipment are covered in section 4.6.

Since ions are trapped and controlled in Paul traps there is a requirement to generate and control the radio frequencies used in the system. Some of these frequencies are used for trapping alone (Trapping RF) and others are used for controlling the ions' internal states (Coherent RF and microwaves). Section 4.7 describes the setup of these sources and their amplification before being fed into the cryogenic chamber.

The neutral Ytterbium atoms that are ionised and trapped need to be loaded into the ion trap without excessive coating of the Ytterbium on the trap electrodes. The cryogenic oven design is covered in the next chapter but the oven controller is described in section 4.8. This controller needs to control the power that enters the oven to allow the Ytterbium to sublimate at a precise time.

The chapter will finish with a description of the DC generation and control setup in section 4.9. This setup is used to create the DC voltages for trapping and shuttling of ions.

4.1 Lasers

As previously described there are three wavelengths needed to trap, store and control $^{171}Yb^{+}$ ions. 399 nm which is used for isotope selection and the first step of the two stage ionisation process. 369.5 nm which is used for ion fluorescence, Doppler cooling and the second step of the two stage ionisation process. 935.2 nm which is used to re-pump from the $^{2}D_{3/2}$ state to allow the ion to continue fluorescing and so play a role in Doppler cooling. More details on the internal state of the Ytterbium ion are found in Chapter 2.

There is a fourth wavelength, 638.6 nm, which is used to bring the ion back after collisions with the background gas can transfer the ion into the $^{2}F_{7/2}$ state. Due to the probability of high energy collisions in the cryogenic environment being extremely low, this laser was never added to the experimental setup, and no detrimental effect was noticed during use as the ion lifetime was approximately 8 hours which was deemed long enough for the experiments performed. If longer experiments were needed in the future the 638.6 nm laser could be added to increase the lifetime.

369 Laser

The 369.5 nm laser is a commercial laser from M Squared Lasers and is comprised of a Lighthouse Photonics Sprout-G pump laser, an M Squared SolsTiS module and an M Squared ECD-X frequency doubler. This laser is capable of high-power narrow-linewidth (< 50 kHz) operation and features both analogue and digital interfaces for precise control and locking.

Figure 4.2 shows the setup of the M Squared Laser. The Lighthouse Photonics Sprout-G pump laser sits on the floor below the optical table and generates 12 W of 532 nm laser light. This is passed up through an optical feed to an alignment and output box that is situated on the optical table. The output of this laser is then guided through two alignment mirrors and an iris, contained in their own box, through a window on the M Squared SolsTiS module. This module uses a titanium sapphire rod as the gain medium, which is pumped by the 532 nm light. This rod then emits 738 nm laser light.

The 738 nm light is passed through a "tap-off" module that contains a fused silica plate that separates off approximately 30 mW of light to be used by the wavemeter and locking setups. This is described further in section 4.3.

After passing through the sampler, more mirrors are used to align the beam into a series

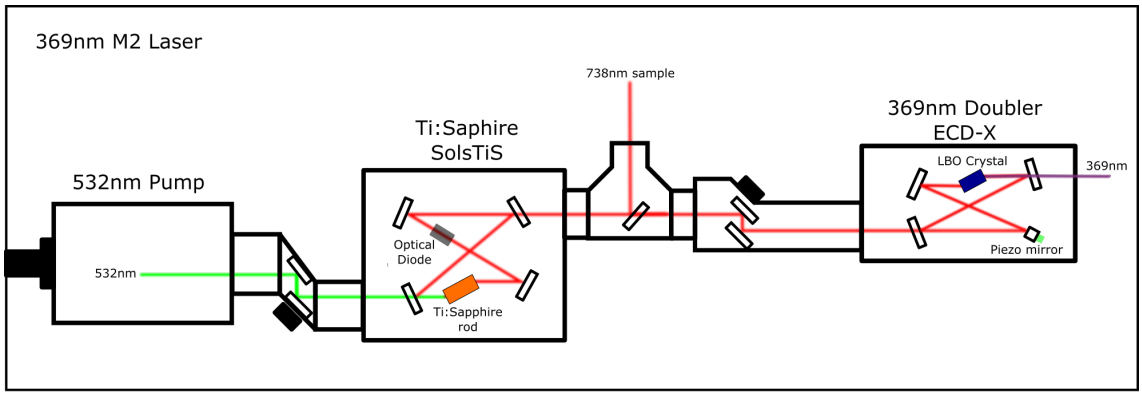

Figure 4.2: Lighthouse Photonics Sprout-G pump laser delivers 12 W of 532 nm light to the Ti:sapphire M Squared SolsTiS module. This module is comprised of a titanium sapphire rod laser and generates 738 nm laser light. This then gets shaped and directed into an M Squared ECD-X frequency doubler which contains a Lithium triborate (LBO) crystal that doubles the laser frequency, emitting 369.5 nm wavelength light.

of beam-shaping lenses that then pass the light into the M Squared ECD-X module. The doubler module contains a Lithium triborate (LBO) crystal and a piezo controlled mirror that utilises the non-linear properties of the LBO crystal to double the laser frequency, giving out around 1.2 W of 369.5 nm laser light.

399 and 935 lasers

The 399 nm laser and 935.2 nm lasers are both commercial lasers from TOPTICA Photonics. The 399 nm laser is a diode laser[1] with a corresponding controller rack comprised of the SC110 Scan controller, DTC110 Temperature Controller, DCC Current Controller and the DC110 Diode Laser Controller.

The 935.2 nm laser is also a diode laser[2], it also has a controller rack with the same modules as the 399 nm laser.

Both these lasers are used by three experiments including the cryogenic one. So the output of each laser is sampled and coupled through a multi-mode fiber to a wavemeter[3]. The remaining light is then split equally three ways and coupled into polarisation maintaining fibers to each experiment.

[1] TOPTICA DL pro HP_029050
[2] TOPTICA DL pro_020275
[3] High Finesse WS-7

4.2 AOM and EOM Setup

Since the lasers are shared between multiple setups we need to agree upon a fixed frequency for each laser to be locked to, which is determined by the isotope being used. For the two main isotopes of Ytterbium (174 and 171) we have two sets of the three principal laser wavelengths. One set is fixed to the wavelengths for $^{174}Yb^{+}$ and the other is set to the wavelengths for $^{171}Yb^{+}$.

For the 369.5 nm laser, however, the wavelength and amplitude needs to be adjusted for each experiment precisely and also rapid on-off control is needed. This is because the 369.5 nm laser is used for heating rate and quantum logic related experiments with microwave radiation. To this end the 369.5 nm laser requires an AOM and EOM setup for each experiment.

There are two main methods of setting up a double pass AOM. The first involves the use of a polarisation beam splitter, the AOM, a mirror and a quarter waveplate. The beam, therefore, passes through the quarter waveplate twice which rotates the beams polarisation by 90 degrees and is therefore separated from the incoming beam by the polarisation beam splitter. This method cannot be used for our AOM[4], because it has a high efficiency polarisation dependence. If the first pass was optimised the return pass would be completely unoptimised.

So it was decided to set up a spacial displacement style double pass as shown in Figure 4.3. The incoming beam starts by passing through a half wave plate which allows control over the polarisation to optimise the first path through the AOM. The angle of the AOM is adjusted and the beam is angled using the incoming mirror to maximise the first-order positive-side spot, this is checked by using a temporary iris and power meter. The beam is then passed through an 200mm spherical lens which keeps the beam from diverging when it reaches the prism. At the prism the beam is reflected back but with a vertical offset of approximately 8mm. This reflected beam then passes through the lens again and is focused into the AOM.

The double passed AOM beam will now have no spatial offset in the horizontal plane

[4] AR coated Isomet 1206C-833

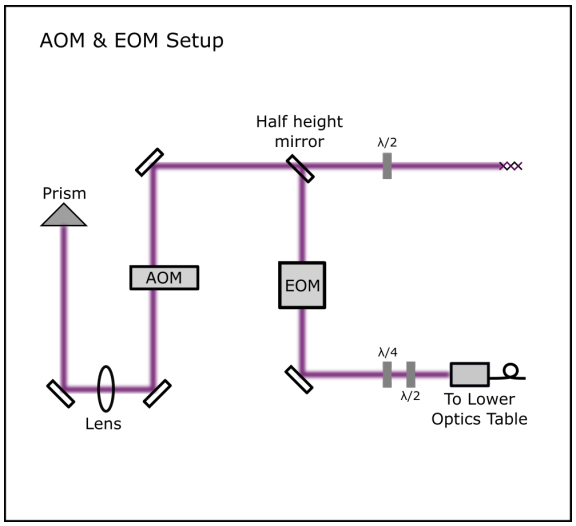

Figure 4.3: AOM and EOM setup depicting the incoming beam path (Top right) passing over a half height mirror and entering the AOM. This light is then collimated by a lens onto a prism that returns the light with a vertical offset. The returning beam then gets redirected by the half mirror through the EOM and polarisation maintaining optics.

when varying the frequency of the AOM driver. This allows us to add additional optical components without frequency variations uncoupling them, it also gives us twice the AOM's frequency addition to the laser beams frequency.

The AOM is driven by a dedicated AOM driver[5] which allows for the AOM to be controlled via analogue voltage outputs from a PCI FPGA card described in section 4.3. The AOM driver has a gate input designed to turn the AOM off and on quickly, however it was found that the AOM does not fully extinguish when turned off as the driver output does not go to zero amplitude. This would disrupt experiments as residual laser light would enter the system. Therefore an additional RF switch[6] was placed after the driver that allows the RF output to be properly isolated from the AOM, see Figure 4.4.

To address the hyperfine transitions impinged with the 369.5 nm laser of the $^{171}Yb^{+}$ ion as discussed previously in Chapter 2, an EOM[7] is added which generates optical sidebands of 2.1GHz.

To maintain the required polarisation for the polarisation maintaining fibre, the beam passes through a quarter and half waveplate which allows us to optimise the polarisation.

[5]Isomet 630C-110G
[6]Minicircuits ZASW-2-50DR
[7]QUBIG EO-T1055M3

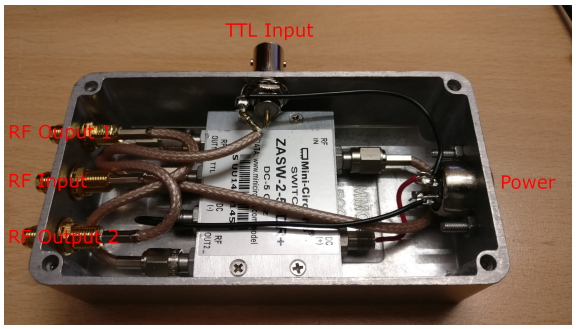

Figure 4.4: AOM switch in shielded box. Labelled are the TTL control that switches the input to output 1 or 2, the RF input and two RF outputs and the power port.

This is duplicated on the output side of the fiber to give full final polarisation control which is required for $^{171}Yb^{+}$ state preparation and readout.

4.3 Laser Locking

Since the excitation probability of the ion state varies with frequency, we need to control our laser wavelengths precisely. For the 935.2 nm and 399 nm lasers, the frequency control needed is not as strict as that for the 369.5 nm laser. This is because we power broaden the 935.2 nm and 399 nm line widths, >100 MHz for the 935.2 nm transition and >10 MHz for the 399 nm transition.

There are multiple techniques that can be used to lock the lasers to fixed frequencies; the three methods used on the cryogenic experiment are wavemeter lock, beat lock and self-stable reference cavity lock.

A wavemeter lock allows us to confine the wavelengths to within ±60 MHz which is the absolute stability of the wavemeter[8] above 370nm. The wavemeter is continuously read at 50ms intervals by the main computer, it then passes those values, via TCP sockets, to a NI Realtime machine which has a PCI-6143 PCI card in it. This card has 8 analogue input/outputs with a maximum sample rate of 250kS s^{-1} with 16-bit resolution. This machine runs a LabVIEW script that takes the wavemeter wavelengths and using a software PID function creates a analogue voltage control signal which gets sent to the piezo control input on the two TOPTICA controllers, and keeps the two lasers locked to a set wavelength.

The M squared laser has a json TCP socket interface which is accessible over a local network interface. The json interface allows for control over the wavelength of the laser. By sending an error value, rather than a voltage, through the json interface the 369.5 nm laser can be locked to the wavemeter.

This style of wavemeter lock is adequate for trapping ions but when fine control is needed, during experiments that are sensitive to wavelength variation, better locking schemes are required. Two systems developed by another PhD student Tomas Navickas have been tested and used on the cryogenic system.

The first method used was an optical beat lock between two M squared 369.5 nm lasers in the laboratory. One laser was locked to a Rubidium vapor cell via a reference cavity.

[8] High Finesse WS-7

This laser was tuned to the correct wavelengths for addressing $^{171}Yb^{+}$ while the second laser, connected to the Cryosystem, was tuned for $^{174}Yb^{+}$. There exists a frequency separation of a few GHz between these two isotopes, so by overlapping a sample of their 738nm beams and impinging the light on a photodiode you can detect a beat interference signal which represents the frequency separation. This signal can then be locked to and used to create an error signal that feeds back into the laser to maintain a laser lock. Under tests, this system was capable of sub MHz stability but was prone to unlocking over long time periods of greater than three hours. This method was used in some of the experiments described in later chapters.

The other method of locking used was a cavity lock achieved by modulating the laser light with a 100 kHz tone, this light was then sent to a self-stable temperature controlled reference cavity, manufactured out of low thermal expansion material and kept in a vacuum. As the laser light modulates it forms transmission peaks on the photodiode at the cavity. These peaks are then amplified by a lock-in amplifier[9] and sent to a TOPTICA Digilock 110 module. The Digilock module contains a software PID loop that generates an output voltage that is sent to the 369.5 nm laser. This allows the laser to be locked to the absolute stability of the cavity. Under tests this setup showed the same level of stability as the beat lock and gave under 1MHz stability over a seven hour period without unlocking.

[9] Femto LIA-MVD-200-H

4.4 Lower Optics Table

Unless explicitly mentioned all mirrors are Ultra-broadband dielectric mirrors[10] from Newport.

The M squared laser shown in Figure 4.5 outputs 738 nm laser light from its side and 369.5 nm laser light from its right hand end. The 738 nm light is split twice by fused silica samplers, the first path is coupled into a polarisation maintaining fiber and passed over to the locking setup which was described in section 4.3. The second path is coupled into another polarisation maintaining fiber which goes to the wavemeter for monitoring of the laser wavelength. The 369.5 nm light is emitted at around 1.2 W, which for a 1.4 mm beam waist is beyond the damage threshold for many coatings and fiber materials. So the first beam splitter uses a fused silica plate that takes around 30% of the total beam, this process is performed again, leaving around 108 mW of power. The remaining power is then split by an beam splitter which takes 10 mW into the AOM and EOM setup and leaves the remainder for other experiments.

The output couplers for the 369.5 nm, 399 nm and 935.2 nm lasers are situated on the far right of the optics table. The 369.5 nm polarisation is critical so there are quarter and a half zero order waveplates after the coupler for polarisation control.

The beam passes through a mechanical shutter beam block which is described in detail in section A.

The beam then passes through a pinhole beam shaping setup as described by a Thorlabs tutorial [89]. This setup uses two identical aspherical lenses and a pinhole that is used to remove unwanted fringes from the Gaussian beam. The first we calculate the 99% defraction-limited spot size by calculating,

$$D = \frac{\lambda \times f}{r} \tag{4.1}$$

Where D in equation 4.1 is the spot size, λ is the wavelength, f is the focal length of one the lenses and r is the beam radius at the $\frac{1}{e^2}$ intensity point.

Two 200mm lenses were used and the incoming beam waist is 1.37mm. Therefore, the calculated spot size was 53.9 µm. The next step is to increase this size by 30% to give the size of the required pinhole. This gives us a pinhole of 70 µm so a pinhole of 75 µm, which is the next available size up was chosen. The pinhole reduces our available power by

[10] Newport PN 10Q20BB.3

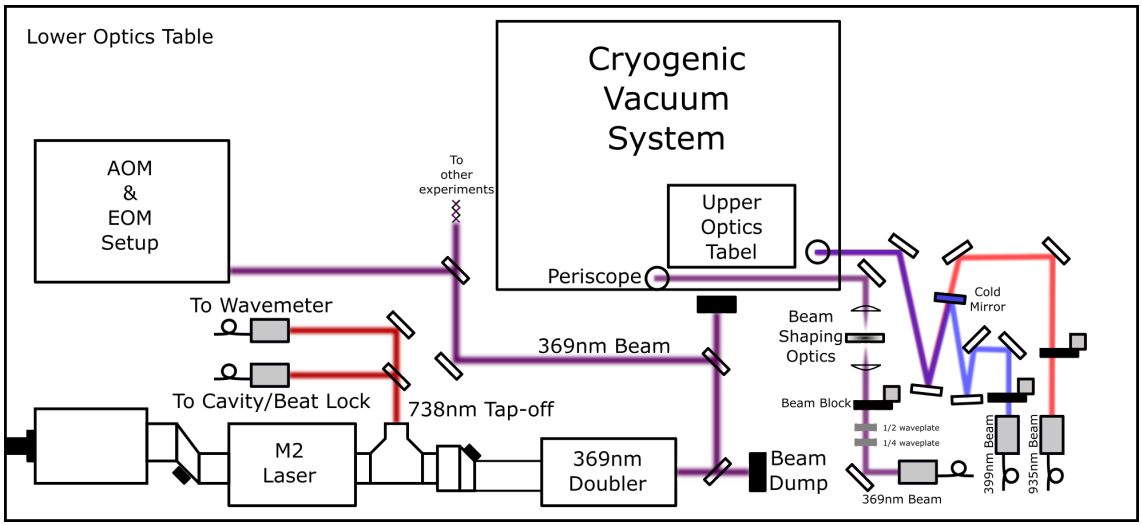

Figure 4.5: Diagram showing the layout of the lower optics table. Depicted is the M squared laser and the optics taking the 738 nm light to the wavemeter and locking setups, the main 369.5 nm output is split and sent into the AOM and EOM setup. On the right side of the table the output couplers for the 399 nm and 935.2 nm lasers are positioned along with the output coupler for the 369.5 nm laser after returning from the AOM and EOM setup. Also shown are the beam shaping optics for the 369.5 nm laser and the beam overlap of the 399 nm and 935.2 nm lasers which then pass to two periscopes for the upper optics table.

approximately 18% but it generates a clean Gaussian beam profile which reduces scatter.

After the beam shaping optics the beam continues on to a periscope that raises the beam up to the upper optics table, see section 4.5.

The 399 nm and 935.2 nm beams reflect off two mirrors that give total degrees of freedom for the overlapping step that takes place on the cold mirror[11] which allows the transmission of wavelengths above 700 nm and reflects wavelengths below. By using the two preceding control mirrors the beams can be overlapped by checking their dot positions on a contact card at two positions, one close and the other far away. Once these two beams have been overlapped they pass to another periscope that raises them up to the upper optics table.

[11] Thorlabs M254C45

4.5 Upper Optics Table

The upper optics table is built around a Thorlabs MB3030/M optical breadboard that measures 30x30cm.

As shown in Figure 4.6 the combined 399 nm and 935.2 nm beam and the separate beam of 369.5 nm light is passed from the top of the two periscopes which originate from the lower optics table. The 369.5 nm beam comes up diagonally towards an all axis translation stage which consists of two 45 degree mirrors.

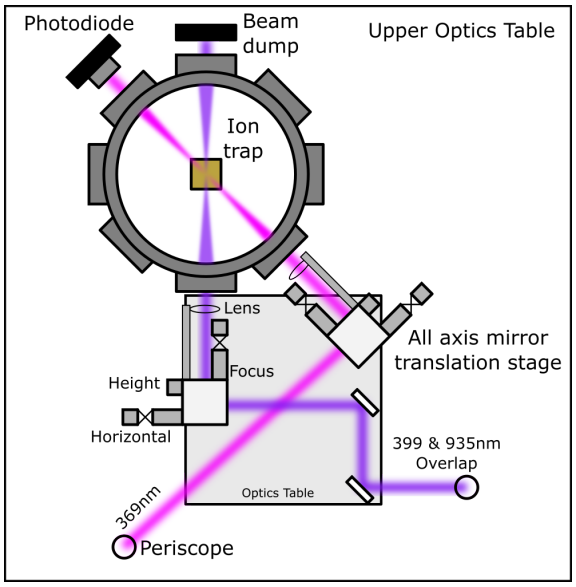

Figure 4.6: Upper optics table features a optical breadboard with two full axis translation stages. These stages allow for full lateral and angular control of the beam through the vacuum system windows and across the ion trap. The two lenses allow for focusing of the beam waist at the ion position. The photodiode is used with a 369.5 nm filter to detect the pass-through beam power.

The bottom mirror is fixed at 45 degrees but the top mirror is rotatable. The mirrors are mounted on three linear translation stages labeled as Horizontal, Height and Focus in Figure 4.6. They are constructed from three linear translation stages with digital micrometers. Using these linear controls we gain full x, y and z translational control and x and y plane rotation control from the rotation of the final 45 degree mirror.

The lens that is mounted to each all-axis stage is an AR coated, 200 mm focal length, spherical lens that is used to focus the beams at the ion's position. The 369.5 nm beam

is focused down to a 55 µm waist. The dual beam of the 399 nm and 935.2 nm can only be optimised for a single wavelength, 399 nm is picked for optimisation as it has a photon energy above the work function of most of the materials inside the vacuum system and could cause charge buildup which would disrupt the charged ions.

The photodiode[12] is battery biased non-amplified type, which is used with a 369.5 nm filter[13] to monitor the laser power after it has passed through the system. This is used to amplitude lock the AOM power when running experiments as variations in power would cause incorrect results. The diode sensor has a surface area of 75.4 mm^2 which gives a diameter of 9.8 mm. The typical ion height is in the range of 50 µm to 200 µm and a typical ion trap size is ≈10 mm, this falls within the dimensions of the photodiode and allows the diode to be fixed without the need to track the beam as it is moved when optimising the ion fluorescence.

[12] Thorlabs DET100A2

[13] Semrock FF01-370136

4.6 Imaging Optics

The imaging optics were originally designed by a former PhD student, Darren De Motte [1], but since some of the setup has changed, in particular the Camera[14], Photon multiplier tube[15] (PMT) and lens positions, I will give a brief summary of the setup here.

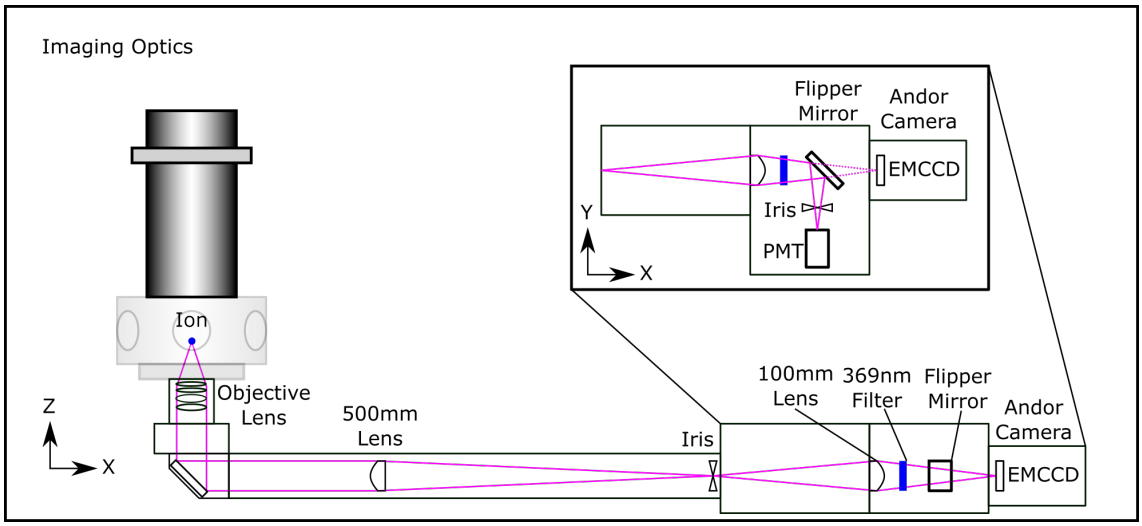

Figure 4.7: Imaging setup. Shown is the objective lens, two singlet asperical lenses with the iris at the focal point. After the 100mm lens there is a 369.5 nm filter and a motorised flipper mirror. This mirror allows for switching between the EMCCD camera and the PMT device.

Figure 4.7 shows the layout of the imaging system. The custom objective lens[16], has a numerical apature (NA) of 0.4. It collimates the light from the ion and sends it down to a 45 degree mirror which directs it along the optical table. The 500mm aspherical lens[17] is 488mm from the iris which, itself, is 89mm from the second 100mm aspherical lens[18]. This setup was simulated in OSLO [1] to give a total magnification factor of 77.45, which is the required magnification to image a diffraction limited ion (0.52 µm) to 5x5 pixel area with each pixel being 8 µm.

The camera is an Andor iXon Ultra 888 Electron multiplying Charged-Coupled Device (EMCCD) which features fast readout rates (26 frames per second full sensor) and a high UV quantum efficiency (greater than 30% at 369.5 nm). The camera has built in cooling which lowers the sensor to −80 °C greatly reducing the noise floor and improving the signal

[14] Andor iXon Ultra 888
[15] Hamamatsu H8259-01
[16] Sill Optics S6ASS2245
[17] Thorlabs LA4782-UV
[18] Thorlabs LA4545-UV

to noise ratio. Since the camera has a large sensor size of 13.3mm X 13.3mm, you can perform some shuttling operations without needing to move the camera optics.

The 369.5 nm filter[19] and flipper mirrors are both on motorised mounts[20] inside light tight boxes just before the camera and PMT. This allows for quick removal of the filter for beam alignment with the ion trap surface and less disturbance of optical components. Also when switching to the PMT for photon counting operations, the mirror can be lowered remotely which opens up combined camera and PMT experiments without manual operator modifications. The iris before the PMT is used to occlude surface scatter and other unwanted 369.5 nm light from the PMT. The iris is moved and closed until there is a maximum ratio between a bright ion and the background photon count on the PMT readout yielding the best signal to noise ratio.

[19] Semrock FF01-370136

[20] Newport 8892-K

4.7 RF and microwave generation

4.7.1 Trapping RF

To trap Ytterbium ions we require a high voltage (100-200V) stable RF frequency that creates the trapping fields in the radial direction as described in the previous chapter. To generate these fields we first need a variable frequency generator[21] that can generate these RF signals. The output of this generator is then amplified by a RF amplifier[22]. This passes through a directional coupler[23] that is placed in the reverse direction such that the coupled port is coupling power from the reflected direction out of the cryogenic system. This amplified RF power then enters the system towards the cryogenic resonator. Figure 4.8 shows an overview of this setup.

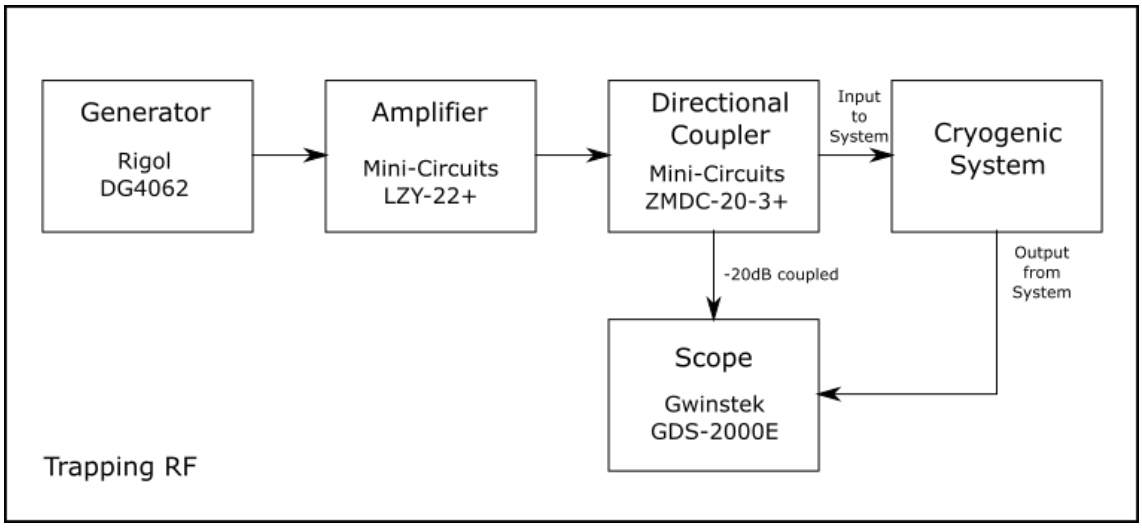

Figure 4.8: System diagram showing the RF generator and amplifier. A directional coupler is used for detecting the reflected RF power from impedance mismatching inside the vacuum system.

Inside the cryogenic system there is a capacitive divider that samples the RF power and passes it out of the system. This output is connected into a scope[24]. The scope is used to monitor the reflected power from the system and also to monitor the trapping RF voltage at the chip. The RF generator is controlled via a Standard Commands for Programmable Instruments (SCPI) interface over Ethernet by the main PC. This allows

[21] Rigol DG4062
[22] Mini-Circuits LZY-22+
[23] Mini-Circuits ZMDC-20-3+
[24] Gwinstek GDS-2000E

for optimisation on the trapping RF by minimising the reflected power and varying the output power to give a corresponding trapping RF potential. While this process can be performed manually it is beneficial to automate the process as when applying RF power to the system, the heat load causes the centre frequency and amplitude to vary.

4.7.2 Coherent RF and microwaves

To be able to trap and perform coherant operations on $^{171}Yb^{+}$ it is necessary to generate coherent RF and microwave radiation. This process has been described previously in Chapter 2. There are many methods for generating the required microwave and RF voltages, the method employed on the cryogenic system was developed by PhD students Adam Lawrence and David Bretaud and an overview is given here. Details on the RF and microwave emitters are given in the following chapters.

The RF voltages are generated by an arbitrary waveform generate[25] (AWG) which features a switchable DAC between 14-bit at $8\,\mathrm{GS\,s^{-1}}$ or 12-bit at $12\,\mathrm{GS\,s^{-1}}$. It also features a spurious free dynamic range (SFDR), which is the ratio between the signal of interest and the largest unwanted distortion signal, of 90dBc even when generating thousands of tones simultaneously.

The AWG has two channels, one channel is used with an RF amplifier[26] and feeds into the cryogenic system. This generates the coherent RF for $^{171}Yb^{+}$ state manipulation. The other channel is connected into the "I" input of the "IQ" mixing stage of a vector signal generator[27]. This high performance vector signal generator features very low phase noise -143dBc/Hz and a very large "IQ" mixing bandwidth of upto 4GHz. Combining these two devices allows for the generation of multi-tone 12.6GHz signals that will be used for $^{171}Yb^{+}$ state manipulation. Both devices are controlled by a secondary computer which generates pulse sequences on both channels which can be triggered with TTL pulses from the main machine. This allows for complex gate operations to be performed, although this is not the focus of this thesis.

[25] Keysight M8190A
[26] Mini-Circuits LZY-22+
[27] Keysight E8267D

4.8 Oven Controller

The ovens are constant current driven by a programmable DC powersupply[28] that is controlled from the main PC via a LabVIEW script using a SCPI interface over a serial RS232 COM port.

This allows the oven to be ramped up slowly over the time span of around 2-4 seconds which reduces the likelihood of damaging the tungsten filament in the oven when starting from cryogenic temperatures, more on the oven design will be given in the next chapter. It also allows fine control of the current and therefore the power of the oven over time. The SCPI interface allows for reading of the current and voltage levels, this is used to calculate the current power level in the oven, as well as programming the fixed current set point.

As the oven warms up the voltage across the winding's increases. This is monitored by the LabVIEW script which then lowers the current to maintain a constant power level. The atom flux is fluoresced by illuminating the ion beam with 399 nm laser light and monitoring the atom flux with the imaging EMCCD camera previously described. It is then possible to calibrate the power over time relationship with the appearance of atom flux on the camera.

To reduce the warm-up time of the oven the starting current was initially set to 0.4A which is near the upper current limit for the tungsten wire. With an initial resistance of 32Ohms, when cryogenic, that gives a starting power of 5.12 Watts. The oven rapidly warms up and as the power level reaches 6 Watts the current is lowered automatically to maintain the power set-point. With these parameters it was calibrated for trapping levels of atom flux within 31 seconds, from cold, or 9 seconds from pre-heat, where the oven had been used previously within the last 30 minutes and residual heat remained.

[28] RS Pro IPS-2010

4.9 DC Setup

For the control, confinement and shuttling of small charged particles such a ions, very precise and noise free voltages are required. This is usually achieved with the use for digital to analogue converters (DAC) which are microchip devices that give out analogue voltages for given digital input words or serial strings of data.

This DAC board was created due to the need for creating large numbers of controllable voltages for trapping and shuttling control. While there exist many manufacturers of FPGA and DAC output cards, most of these have low numbers of analogue output channels (8 or 16 most common) where we require 60 or more. They also are extremely expensive, and they do not always offer direct control interfacing for 3rd party software which will be important for shuttling control later. While DAC systems with products such as M-Labs ARTIQ do exist they were still in development when this project started and prone to overheating problems. It is for these reasons that a custom DAC board was created and it was used successfully on the cryogenic system.

The first setup used on the cryogenic system was the field-programmable gate array (FPGA) PCI[29] which has eight 16-bit analogue output channels each capable of $1\,\mathrm{MS\,s^{-1}}$ update rate. This card can output -10 V to +10 V and deliver a sink-source current of 2.5 mA. This card was then connected through a breakout box that adapts from the high density D-SUB connector that is on the back of the PCI card to SMA cables into a 5th ($\approx$ 80 dB/decade) order resistor-capacitor (RC) filter. The filter is a low-pass topology with a 3 dB cutoff at 32 Hz, this is to suppress high frequency noise at the ion secular frequencies and also low frequency noise from sources such as the mains which are dominant at 50Hz and its first harmonic at 100 Hz. This filter was created by Darren De Motte and more details of its construction are given in his thesis[1].

The second setup employed contains the same filter device used in the first setup but the FPGA PCI card was replaced with a self designed DAC board that featured two AD5370 DAC's from Analogue devices. These DACS feature 40, 16-bit channels each for a combined 80 channels with the two combined. This DAC was chosen for its large number of output channels while still maintaining 16-bit resolution. It also features a resistive ladder style topology which guarantees full monotonic performance over the 16-bit range.

[29] National Instruments PCIe-7842R

This guarantees that the output will always rise in voltage when given the corresponding code to rise and vice versa.

The DACs have a slew rate of $1\,\mathrm{V\,\mu s^{-1}}$ and a maximum settling time of $20\,\mu\mathrm{s}$ for a full scale (1 least significant bit (LSB) to full scale range) voltage jump. It also features an Integral nonlinearity (INL) of 4 LSB, this means that for a given input code (programmed voltage) the maximum/minimum actual output voltage would be upto 4 LSB different from the programmed value. Equation 4.2 calculates the voltage step of 1 LSB for a given bit depth and voltage range.

$$V_{1LSB} = \frac{\Delta V}{2^{Bd}} \tag{4.2}$$

Where V_{1LSB} is the voltage step of a single bit, ΔV is the rail to rail voltage range of the DAC and Bd is the Bit depth of the DAC. For the AD5370 this gives a V_{1LSB} of $305\,\mu\mathrm{V}$. So the maximum voltage error would be $1.22\,\mathrm{mV}$.

The DACs also feature a differential nonlinearity of 1 LSB, this is the measure of the maximum error, in LSB, between each step in the voltage code. So a value of 1 LSB or less would guarantee monotonicity.

The DACs are programmed using the serial peripheral interface (SPI) which is a full duplex synchronous master-slave standard. The DAC's each require a word length of 24 bits to update a single channel, 16 bits for the DAC word, 6 bits for the address and two bits for the mode which determines how the data is interpreted (voltage change or register update). The maximum SPI clock rate is 50 MHz which gives a programming time for a single channel of 480nS , but due to internal calculations made by the DAC for the C and M registers and the output registers the whole process actually takes 600nS per channel. Programming can be streamed continuously as long as the final word sent to the DAC allows for the required 600nS window time to elapse before ending the data clock.

Figure 4.9 shows an overview of the system structure of each of the 40 channels in the DAC. The X1A, X1B, M and C registers are all 16-bits long and are the only directly programmable registers in the DAC with exception of the control register not shown in the figure. X1A and X1B have the same role for storing the voltage word, so only one register can be used at a time but the two allow for fast switching between two prestored

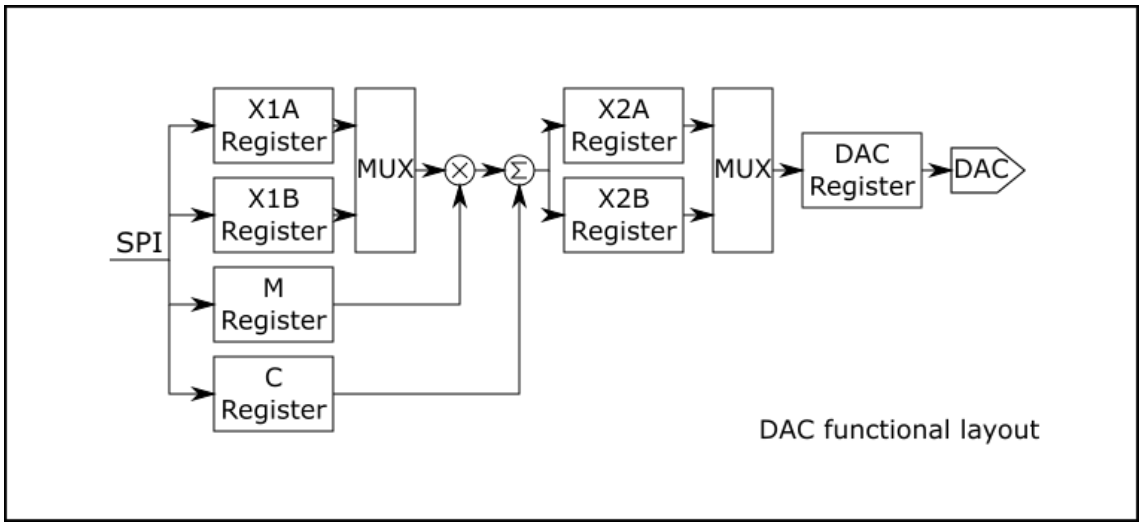

Figure 4.9: DAC system overview, X1A and X1B 16-bit registers contain the voltage word before processing by the DAC's internal architecture. The M 16-bit register contains the multiplier offset value and the C 16-bit register contains the sum offset value. Also shown is the processing path, either the X1A or X1B register is selected via an input control register (not shown). The X1A or X1B register is then passed through the multiplier and sum offset encoders into the second set of voltage registers X2A and X2B. These registers can then be activated and sent to the DAC output.

states. The M register is a multiplier register that allows for maximum full scale errors to be calibrated out. The C register is a zero scale offset register for calibrating out zero scale errors. By using both these registers it is possible to calibrate the full range for each channel individually which drastically reduces temperature and humidity driven offsets after settling. After passing through both multiplier and sum encoders the resultant word is then stored in the internal X2A or X2B registers. This is the process previously described that requires roughly 120nS and therefore limits the programming window to a minimum of 600nS total. The use of the two voltage word registers is to allow for fast switching between the two prestored states. It is possible to program the first register for a given voltage then program the second register, after this has been performed you can send a simple switch register command to the DAC and all or some of the outputs will rapidly switch between the two voltage states. The DAC code that is used to work out the output voltage is given by

$$DACCODE = \frac{INPUTCODE * (M + 1)}{2^{16}} + C - 2^{15} \tag{4.3}$$

The INPUTCODE is the 16-bit word stored in the X1A or X1B register, M and C are, as previously described, the multiplier and offset register values respectively. Using DACCODE we can then use

$$VOUT = 4 * VREF * \frac{DACCODE - (4 * OFFSETCODE)}{2^{16}} + V_{SIGGND} \tag{4.4}$$

to calculate the actual voltage out of each DAC channel. VREF is the voltage of the voltage reference, in our case this is 5V. V_{SIGGND} is the signal ground potential, this is 0V with our setup. OFFSETCODE is then used to scale the 0 to 65536 word to a given voltage range, in our case this maps 0 to -10V and 65536 to +10V. The M, C and OFFSETCODE words are all reprogrammed for each channel after calibrating, the only registers programmed when performing ion shuttling operations or trapping are the X1A and X1B registers and the control register for swapping between X1A and X1B.

Each DAC has an input/output pin called LDAC. This pin, when held high, stops the DAC from changing its output but allows it to perform all required calculations, effectively precaching the output for synchronisation. Both DAC's can hold this pin high when they are updating their registers and the control board also can hold this high. This allows us to change different numbers of channels on each DAC simultaneously which would normally cause a synchronisation problem as the DAC with less channels to update would finish first and the voltages would go live before the second DAC had finished. We can also hold LDAC high ourselves until the required time has arrived, synchronising with an external process. After LDAC has gone low there is a 3 µs delay before all DAC channels will update to the new voltage levels.

Figure 4.10 shows the top and bottom of the completed DAC board. The board is powered from a $\pm 15V$ linear power supply which was home made and built into a separate box for isolation reasons. It is connected with twisted pair shielded wire to minimise noise pickup. There is a jumper selector on the bottom for selecting between the internal 5V regulator[30] or USB powered from the interface card[31]. The USB powered option is for development reasons when the DAC board is on the workbench where you no longer require the $\pm 15V$ supply and you are only checking the data communication protocols without powering up the DAC outputs. For normal operation the selector is switched to

[30] Diodes AZ1117-5.0

[31] FTDI FT4232H

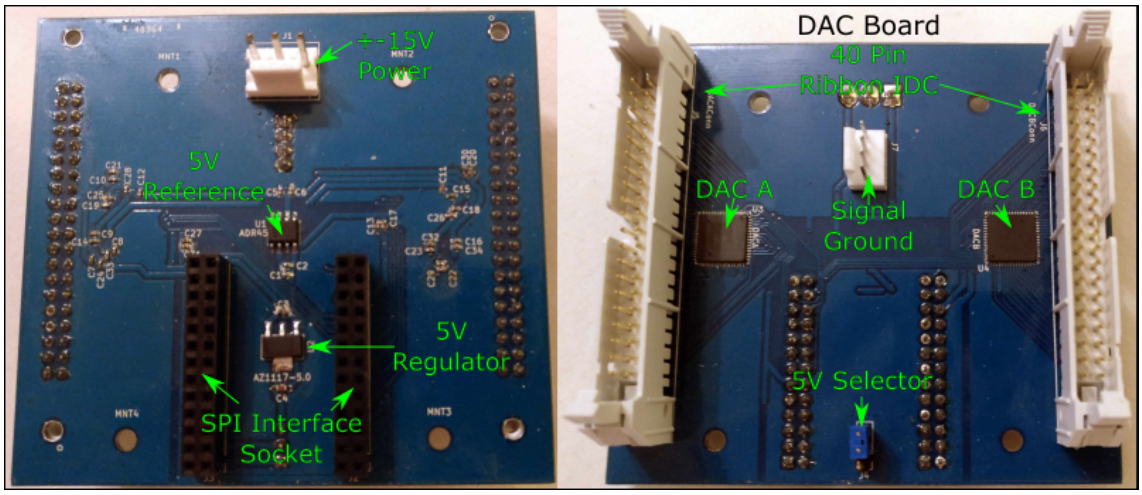

Figure 4.10: Image showing the top and bottom of the completed DAC board. Shown is the connector for the main voltage rails of the DACs that are from a linear $\pm 15V$ power supply. Also shown is the 5V reference that the DAC voltage output is relative to and the 5V regulator that powers the digital logic. The SPI socket is for the data communication card or cable. On the bottom of the board is the signal ground connector and the two DACS. There is also a 5V selector jumper for selecting between USB powered or 5V regulator powered for the interface card.

the internal 5V regulator that supplies the digital power from the linear power supply which has less noise than the USB port.

There is also an ultra stable 5V voltage reference[32] which features 1mV accuracy (0.02%) and 2 ppm/°C temperature stability. It also offers 25ppm drift over 1000 hours.

The signal ground needs a good connection to the shielded DSUBs and the case, for this reason a four pin connector labelled as "Signal Ground" in Figure 4.10 was added where the four pins are grouped together with a copper braid that is bolted to the case.

The DAC board requires two SPI interfaces, one for each DAC, to be addressed. The reason for choosing two interfaces rather than using the chip select pin on a single bus was to double the data rate when programming both DACs simultaneously. These interfaces can be connected using the socket to another master controller such as the M-Labs ARTIQ system, which was a design consideration. But for use with the cryogenic system the socket

[32] Analog Devices ADR4550BRZ-R7CT-ND

is connected to a daughter board[33] by FTDI which is shown in Figure 4.11.

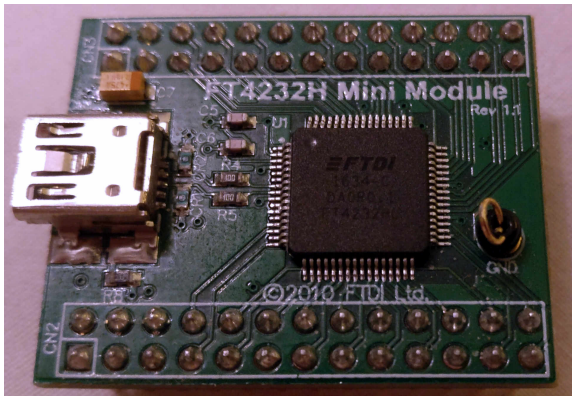

Figure 4.11: FTDI USB Module with quad Multipurpose universal asynchronous receiver-transmitter / Multi-Protocol Synchronous Serial Engine (UART/MPSSE) interfaces.

This board contains an FT4232HL chip which is a USB to quad Multipurpose universal asynchronous receiver-transmitter / Multi-Protocol Synchronous Serial Engine (UART/MPSSE) adaptor. Two of the interfaces are set as full-speed SPI with 50MHz clocks, one for each DAC. The other two interfaces are left as general purpose input/output (GPIO) which is used for LDAC control and BUSY flag reading from the DACs to the computer. The FTDI chip was selected for its full speed multi-channel SPI with additional GPIO abilities, its low cost, small footprint and detailed C++ programming libraries.

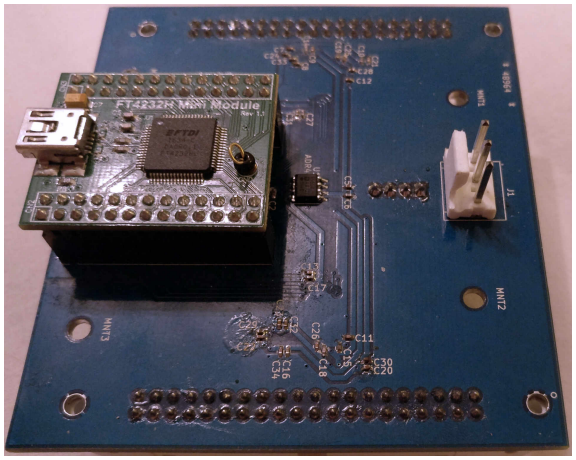

Figure 4.12: Full DAC PCB and FTDI daughter board, case and IDC cables not shown.

Figure 4.12 shows the entire DAC board with FTDI daughter board. The entire setup is mounted in a aluminium case with two Insulation-displacement connector (IDC) ribbon cables connected to two 50 pin DSUB connectors on the case. The power socket and USB socked are positioned on the top of the board to provide interference shielding to the

[33] FTDI FT4232H

DAC outputs below. The board also features separate digital and analogue grounding for interference minimising reasons.

This chapter has given an overview and details on the external experimental setup required for trapping and controlling an Ytterbium ion in a cryogenic vacuum system. Details on the internal setup within the cryogenic environmental will be given in the next chapter.

Chapter 5

Cryogenic Vacuum System

To control and manipulate small charged particles we need to create an environment that reduces the influence from collisions with other gas molecules, and stray magnetic or electric fields that would cause them to move in unpredictable ways. Since indevidual Ytterbium ions have low masses and are charged we have to create an environment that is engineeringly challenging.

Firstly we have to create a vacuum that all the required equipment will be housed in. This chamber has to be able to create vacuum pressures in the 1×10^{-11} mbar range for the ion to be isolated enough to perform useful processes on. Processes we need to be able to perform are things such as heating rate measurements, shuttling or quantum logic gate operations. We also need to shield the ion from electromagnetic interference, this is performed by creating a Faraday cage around the ion.

While reducing the effect of the environment on the ion, we also need to be able to control the ion with applied RF and DC fields, along with magnetic field gradients for quantum logic operations. The RF trapping fields are of the order of 100-300 V peak and in the frequency range 10-30 MHz. We also need to pass large currents into the system to drive magnetic field generating coils that create the field gradients needed for gate logic operations. Finally DC fields are needed to axially confine the ions position on the ion trap, the fact these voltages are low (-10-10V range) makes them easier to generate than the RF voltages, but to be able to shuttle or change the absolute position of the ion requires us to have many connections, of the order of 100 connections for a single X-Junction.

Ion trapping requires lasers and microwaves for different isotopes, we also require co-

herent RF magnetic fields. These fields have precise angular and positional requirements, polarisations and powers which must all be controlled.

Thought must also be given to the mounting structure within the chamber. Unlike macroscopic ion traps, such as blade traps [90], surface ion traps are made on thin wafers of dielectric such as sapphire or silicon only 600-800 µm thick [34]. This makes them extremely fragile, small shearing forces can easily fracture the trap rendering it useless. So we require a mounting structure that is non destructive and reusable, but able to hold the ion trap in place for the precise alignment of lasers and ion flux from the atomic ovens. The ovens also need to be created that give a well defined flux of neutral Ytterbium to the chip without excessively coating the surface which requires precise alignment and positioning.

These broadly are the requirements of all ion trap experiments, but due to the need for us to create a fast turnaround testing system for modelling, characterisation and designing new ion traps, we require a setup that also utilises cryogenics. This brings benefits in the time it takes to reach ultra high vacuum (UHV) and the material choices we can use internally, as well as increasing the ion's lifetime, but it also brings many drawbacks. By dropping the temperature to approximately 4K we have to design around thermal contraction, heat load caused by the various connections to the outside and protecting the ion traps from crystallisation of remnant gases which in the extreme can damage the trap's surface.

This chapter deals with these challenges and the engineering used to overcome them to create a cryogenic surface ion trap experiment that was used to characterise two different ion trap designs which is the subject of chapter (ion trap characterisation).

5.1 Cryogenics

Cryogenics allows us to cool the chip and surrounding area down to 4K. By cooling down the entire internal setup we lower the gas pressure via three main methods, cryosorption, cryotrapping and cryocondensation [9].

Cryopumping can generate very low pressures of $< 1 \times 10^{-12}$ mbar but it is an inherently weak process mainly reliant on van der Waals forces unless chemically active absorbers are present which dominate (chemisorption). This means that cryopumping is only useful after the majority of the residual gasses present in the system have been removed. Initial pumping is done by a turbo molecular pump which can pump the system down to 1×10^{-7} mbar. Care should be taken to not introduce any materials to the system that show excessive outgassing at $\approx 1 \times 10^{-7}$ mbar as this can inhibit the cryopumping process or cause coating of delicate equipment such as the ion trap before reaching the intended final temperature of 4-12 K.

The first method of cryopumping is known as cryocondensation. When the cold surface is bel ow the triple point of a particular gas it can directly sublimate, from gas to solid when it touches the cold surface. Predicting the rate of cryocondensation is a complex process that involves multiple stages, after the impinging gas particle or molecule joins the surface it is absorbed into the crystal lattice, it can then start to form a crystal growth site leading to multiple crystal layers. This site grows with more impinging gas at a rate which is dominated by the diffusion of the gas into the crystal lattice [91].

Figure 5.1 shows the equilibrium vapour pressure curves for common gasses. You can see that the most abundant gasses at 4K will be helium and hydrogen. Hydrogen contamination can cause problems by bonding with the trapped ion forming a molecule, this effectively decreases the lifetime of the ion within the system [92].

The second method of cryopumping is by cryosorption (also known as physisorption). It is the process by which a low kinetic energy gas particle losses enough energy when impinging with the cryogenic surface that it sticks to the surface via van der Waals forces even if its phase transition temperature is above that of the cryogenic surface. This means the the molecular concentration on the surface is far higher than the normal gas transition concentration for that temperature by cryocondensation alone [9]. This is crucial for

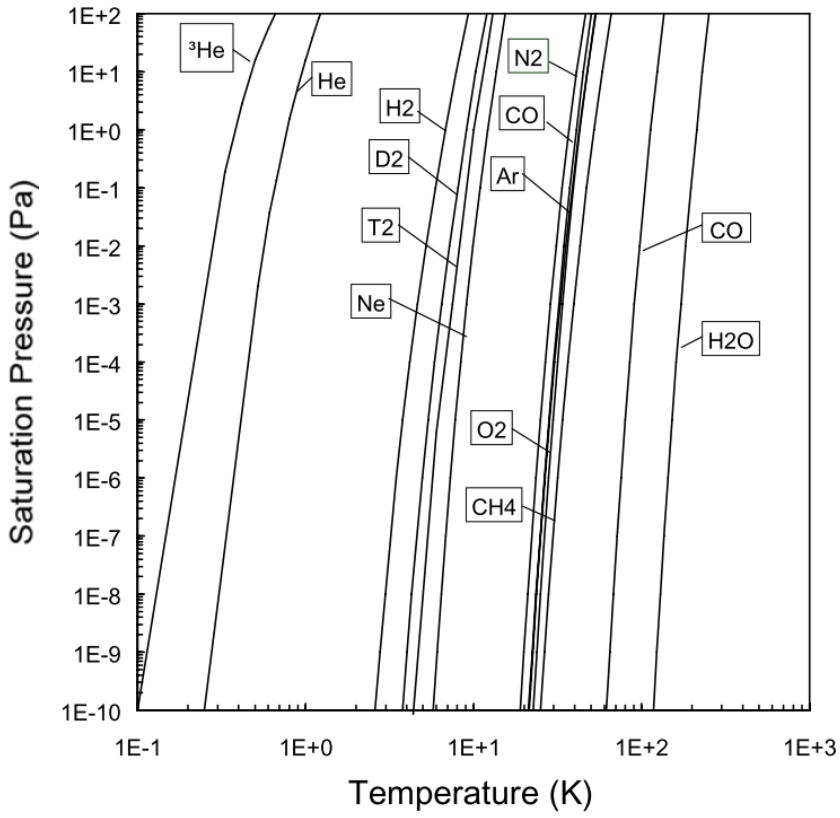

Figure 5.1: Figure showing equilibrium saturation curves of common gasses. Adapted from [9]

pumping out helium and hydrogen which would normally not be pumped sufficiently by cryocondensation alone [93, 94, 95].

The final method of cryopumping is cryotrapping. This is formed when a gas which normally cannot be trapped either by cryocondensation or cryosorption becomes trapped within layers of other gasses via the two main methods already described. Essentially the non-trappable gas gets stuck between layers of crystallised molecules and is therefor effectively taken out of the system. This process is the weakest of the three as the equilibrium pressures are so low to begin with, but this process can be accelerated by injecting another gas into the system with the purpose of trapping a normally otherwise difficult gas, for example Ar injection to remove He. This process is not done with our cryogenic system.

5.1.1 Cryogenic Noise Reduction

Johnson-Nyquist noise [96], sometimes called thermal noise is electrical noise created by the random thermal vibrations in charge carriers (principally electrons). This thermally generated charge movement causes small random electrical signals to propagate through

any electrical connection that exhibits resistance. Electrical connections include the wiring for the RF and DC electrodes and the surface of the electrodes themselves.

The spectral density of this type of noise is directly proportional to the real component of the complex impedance and the temperature [97] and is given by,

$$S_V(\omega) = 4k_B T R(\omega) \tag{5.1}$$

where $S_V(\omega)$ is the one-sided noise spectral density, k_B is the Boltzmann's constant in joules per kelvin, T is the temperature in kelvin and $R(\omega)$ is the real part of the complex impedance of the system (Sometimes written as $\Re(Z)$ where Z is the complex impedance).

It can be seen that by reducing the temperature of the system the noise spectral density is reduced proportionally. Since the resistance of the system is also temperature dependent [98] the two effects combined give a large reduction in Johnson-Nyquist noise at cryogenic temperatures.

A fundamental limit on the heating rate of the ion is related to the Johnson-Nyquist noise level [99] and the electrode ion separation distance and it was found to scale as d^{-4} [100].

The reduction in temperature also reduces the anomalous heating of the ion. Anomalous heating is a subject of much study and there are many theories as to the cause, this is why it is still called anomalous heating. It shows an ion electrode separation dependence orders of magnitude larger than that which can be explained by Johnson-Nyquist noise alone. Surface treatments such as pulsed laser cleaning [101], ion-beam bombardment [102, 103] and surface annealing along with cryogenic temperatures [104, 12] have shown orders of magnitude improvement over non-treated and non-cryogenic ion traps. This suggests that anomalous heating is the result of surface contamination and a patch potential model gives the exponent to the ion-electrode separation as -4. Recent studies in 2018 [100] have refined this exponent, with variable ion hight traps, giving values of -3.79 ± 0.12.

5.1.2 Superconductivity

By operating in the 4-12K range we can also make use of superconductors. Superconductivity is the property exhibited by some elements and alloys where bellow a critical temperature and current the element or alloy exhibits no resistance to the flow of current [105].

Superconductors are generally split into two categories, Type I and Type II. Type I superconductors are described by the BCS Theory [106] and normally comprise of base elements. Type II superconductors are normally alloys or ceramics and tend to have higher critical temperatures and currents.

By using superconductors we can lower the dissipated power from currents flowing through wires, this is especially important with the magnetic field coils as they sink 10-20A and metals such as copper would dissipate heat into the first stage of the cyrocooler. Also by having no resistance the superconductors would not exhibit Johnson-Nyquist noise as the resistance is zero. There are still inductive (flux) and capactive (charge) noise sources but studies show that the amplitude levels are lower [107].

The primary two types of superconductor used on the Cryosystem are NbN (Niobium nitride) and NbTi (niobium titanium). NbN has a critical temperature of around 16K and NbTi has its at around 10K. NbTi is the main superconductor used in copper coated litz wire form (multi-stranded core) for the cryogenic resonator, that generates the trapping RF voltages, and magnetic field coils due do to its very high critical field strength of around 15T.

5.2 Cryocooler and Vacuum System

The majority of the work for designing the vacuum chamber, the choice of cryocooler, the low vibration interface and first generation oven was performed by a previous PhD student Darren De Motte [1]. A brief overview will be given here for completeness. The work on the internal structures such as the chip mounts and RF/microwave emitters etc is the subject of this thesis and will be given in detail.

5.2.1 Cryocooler

The first step in designing a cryogenic vacuum system is deciding upon a suitable cooling method. The method chosen must meet the following criteria

- Low Vibration (<100 nm)
- High power capability at cold interface (>1 W)
- Low upkeep cost
- Small installation size
- Trap mount cold interface temperature below 10 K

Low vibration is required to stop the cryogenic setup from artificially causing ion motion and therefore heating of the ion chain when it comes to performing quantum logic operations. Also excessive vibration amplitude (>50 µm) could disrupt shuttling as the typical trap geometry is of the same order. Excessive vibration would also reduce the collection efficiency of the system as the ion would move out of focus for the imaging optics. The ion requires laser access for state preparation and detection, ionisation and Doppler cooling. This means that we require optical access for both readout (imaging) and lasers. Optical windows are therefore required and this adds thermal loading to the cold stage. Due to the large number of DC wires required for complex ion traps (100 connections) and the need for multiple coax cables, there is a high thermal sink path through the conductors into the cryogenic system. Therefore the system requires at least the capability of sinking 1W of thermal power.

To operate with commonly available superconductors such as NbN and NbTi we require the final stage temperature to be bellow 10K.

There are four main methods used for cryogenically cooling vacuum systems. The two main methods that use liquid cryogens are bath and continuous flow cryostats. Bath cryostats use a large bath of cryogen liquid, usually liquid nitrogen or helium, as the primary cold interface. As the cryogen evaporates it maintains its temperature and that of the equipment mounted to the bath. Bath and flow cryostats show very low vibration and have been used successfully for ion trapping experiments [39, 108, 109]. The drawback of bath and flow cryostats, also called cryocoolers, are that they require refilling as the cryogen evaporates, causing downtime while the bath is refilled. This creates a high running cost for experiments and prohibits uninterrupted running.

Continuous flow cryostats use a flow of liquid cryogen. This flow passes an interface where the cryogenically cooled equipment is mounted. Unlike bath cryostats they can opperate without stopping to be refilled but they still require an uninterrupted supply of cryogen which creates a higher operating cost.

The other main method of cryocooling is by using a closed cycle cryostat. Closed cycle cryostats use a gaseous cryogen that is cycled between high and low pressure and reused to form a heat pumping cycle. Closed cycle cryostat tend to have higher vibrations when used directly (10-100µm) but by using appropriate vibration interfaces this can be reduced with minimal loss in cooling power. Closed cycle cryostats have also been used successfully for ion trapping experiments [41, 110, 40] and can be used indefinitely, ignoring leaks from the closed cycle system and general maintenance.

After careful consideration the Gifford McMahon closed cycle cryostat was chosen, its properties are found in Table 5.1.

This cryostat was chosen for its high cooling power and low 1st and 2nd stage temperatures which allows for the use of common type II superconductors. Figure 5.2 shows the heatmap for the crystat. It is worth noting that the first stage can sink from 0-60W and still maintain 1.5W of cooling on the second stage. This is important for thermally anchoring the DC and RF wiring and the atomic oven as the first stage is the mounting point for both.

5.2.2 Ultra Low Vibration Interfaces

Closed cycle cryostats have the largest vibration amplitudes of the different types mentioned. This large motional vibration can cause problems with ion trapping as displace-

Cryostat	Gifford McMahon
Model	Sumitomo SHI RDK-415
Cooling power at 2nd stage	1.5W at 4K
Cooling power at 1st stage	35W at 50K
Quoted base temperature	3.5K
Measured base temperature [1]	2.5K
Vibration*	10-100um
Vibration after buffer gas interface	<15nm

Table 5.1: Cryostat details and measured results. Vibration is spread spectrum with dominant peaks at 50Hz and 100Hz.

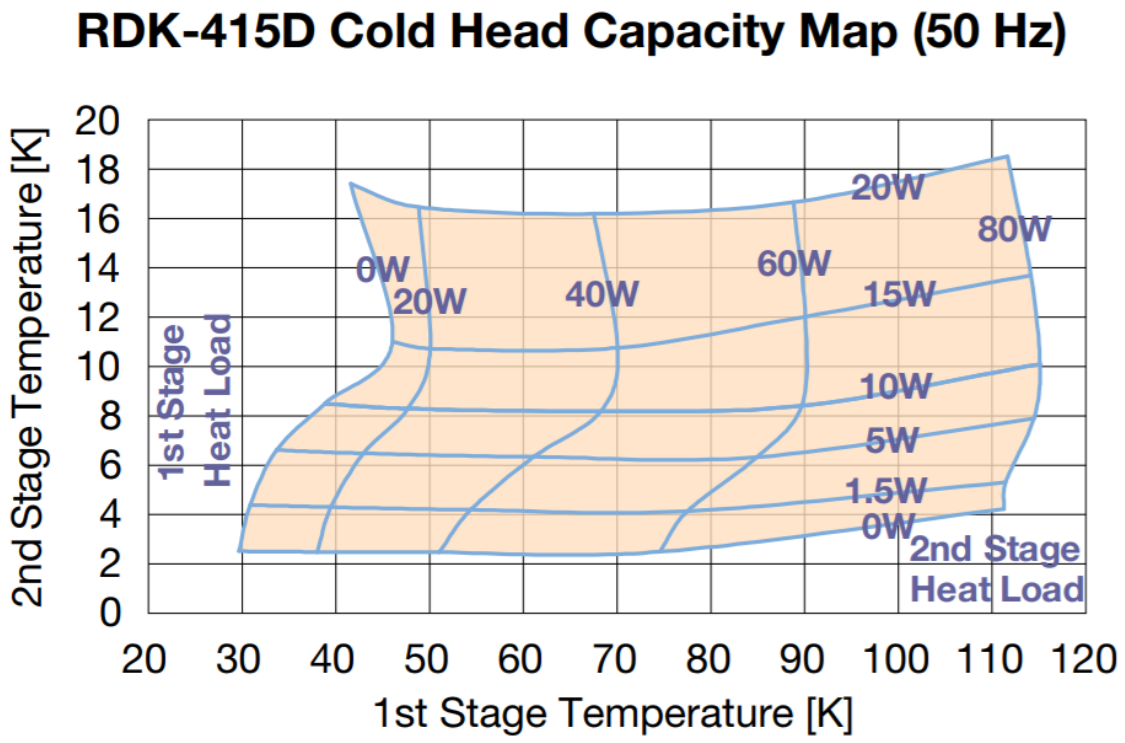

Figure 5.2: Figure showing the heat map profile of the SHI RDK-415 running at 50Hz. This map shows the equilibrium temperature for a given heat load. Adapted from [10]

ment in the ion's motion may cause heating of the ion and any motional mode quantum operations would be disrupted by this displacement.

There are multiple methods of buffering the vibration of the cryostat while still coupling the cooling power. One method uses copper braid to connect the cryostat to the mounting plate of the UHV system. This method offers a high thermal coupling efficiency but also has the highest vibrational coupling [111].

Other methods involve using a liquid cryogen such as helium as the buffer medium. These methods require close monitoring when starting up the cryosystem as the buffer liquid rapidly evaporates and requires constant refilling until the system equalised at cryogenic temperatures. Also the lowest vibration is only achieved when turing off the cryostat and using the buffer as a bath cryocooler, this would not therefore allow for continuous operation. This kind of setup would not allow for high temperature operation (50-100K) as the liquid buffer medium would evaporate.

5.2.3 Gas Buffered Ultra Low Vibration Interface

It was decided that the type of ultra low vibration interface that would be required for this system would use a buffer gas as the heat exchange medium. The type used was a ColdEdge Technologies Ultra Low Vibration Interface (ULVI).

Figure 5.3 shows a cross sectional view of the vacuum system and the ULVI. A buffer gas of CP Grade Helium (99.999%) is fed at 35 mbar into the top of the ULVI and it surrounds the entire cold edge of the cryostat forming a jacket of Helium between the cryostat cold edge and the outer cold wall of the UHV chamber. There is a clearance of 3mm between the inner cold edge and the outer UHV wall with the addition off concentric ring heat exchangers which increases the surface area and improves the thermal efficiency of the system. There is no mechanical link between the cold edge of the cryostat and the UHV vacuum system, the only physical connection between the two is the rubber bellows at the top to contain the helium buffer gas.

With this setup we achieve only a 20% drop in cooling efficiency at the 2nd stage while delivering <15nm vibration. This leaves us with a 2nd stage heat pumping power of 1.2W at 4K which is still more than adequate for our experiments.

The cryostat is mounted on an overhanging equipment table that is directly positioned over the optics table and bracketed to the walls of the lab. This completely separates the vibrational motions of the cryostat from the optical table and completes the ULVI setup.

5.2.4 Vacuum System

Now that we have the design for the ULVI we can create the outer vacuum system that will house the ion trap and other equipment at 4K. Figure 5.4 shows the entire assembled vacuum setup including the ULVI (top), imaging optics and vacuum chamber (bottom) and other ancillary cabling/equipment.

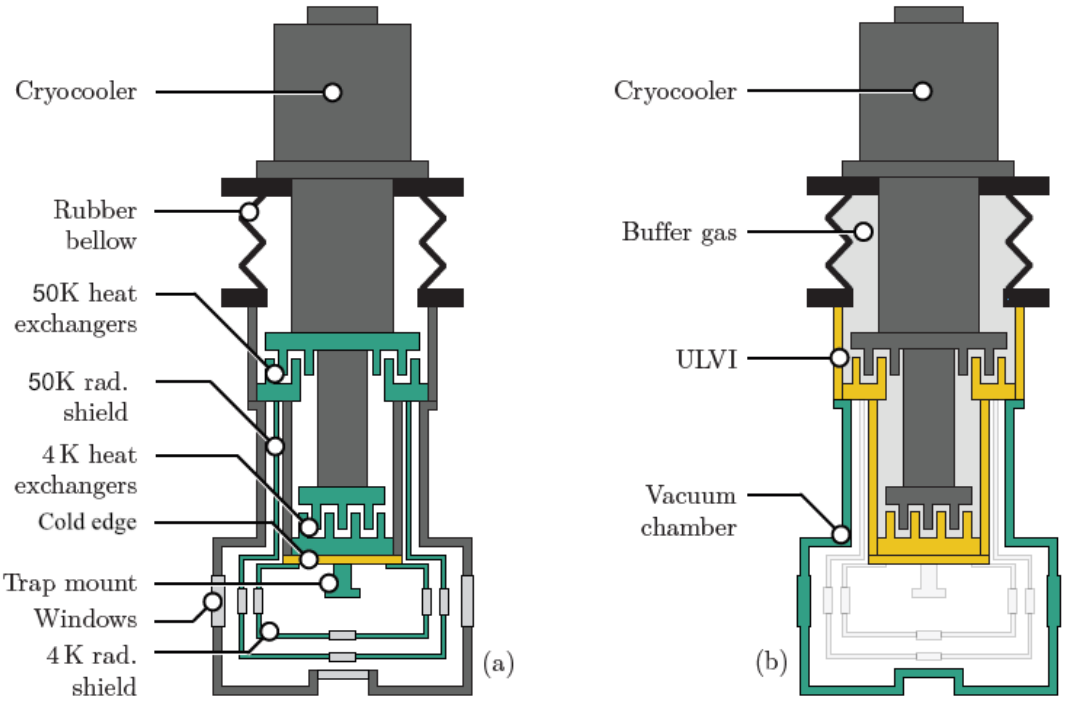

Figure 5.3: (a) Schematic diagram showing the entire vacuum system. (b) Highlighted digram showing the buffer gas and heat exchangers. Adapted from [1]

The whole setup is centred around a spherical octagon[1]. Connected to the octagon is an ion pump[2], right angled valve[3], ion gauge[4], 2 x 50 pin DSUB feedthroughs, a 6 pin high voltage feedthrough[5] and four CF40 flange quartz silica viewports that are AR coated for 369.5 nm, 935.2 nm and 935.2 nm wavelengths. For connecting the RF and microwave inputs the system also has two 1.33" one-port SMA feedthroughs[6] and one 2.75" two-port SMA feedthrough[7]. These RF and microwave feedhthroughs are rated to 18 GHz.

Due to the fact that the system exhibits cryopumping it is possible for microleaks to go undetected while the gasses are frozen to the cryogenic components within the system. Under an uncontrolled shutdown of the system these gasses can cause an over-pressure event within the system which is a safety risk. For this reason an over-pressure burst disk[8] is fitted that ruptures at a pressure of 1.7 bar.

The main imaging window consists of a custom CF160 quartz silica window. This

[1] Kimball Physics PN MCF600-SphOct-F2C8
[2] Varian StarCell 9191145)
[3] K.J.Lesker VZCR40R
[4] Varian 9715015
[5] K.J.Lesker EFT0265063
[6] Allectra 242-SMAD50- C16
[7] Allectra 242-SMAD50-C40-2)
[8] Allectra 461-PBD-C40

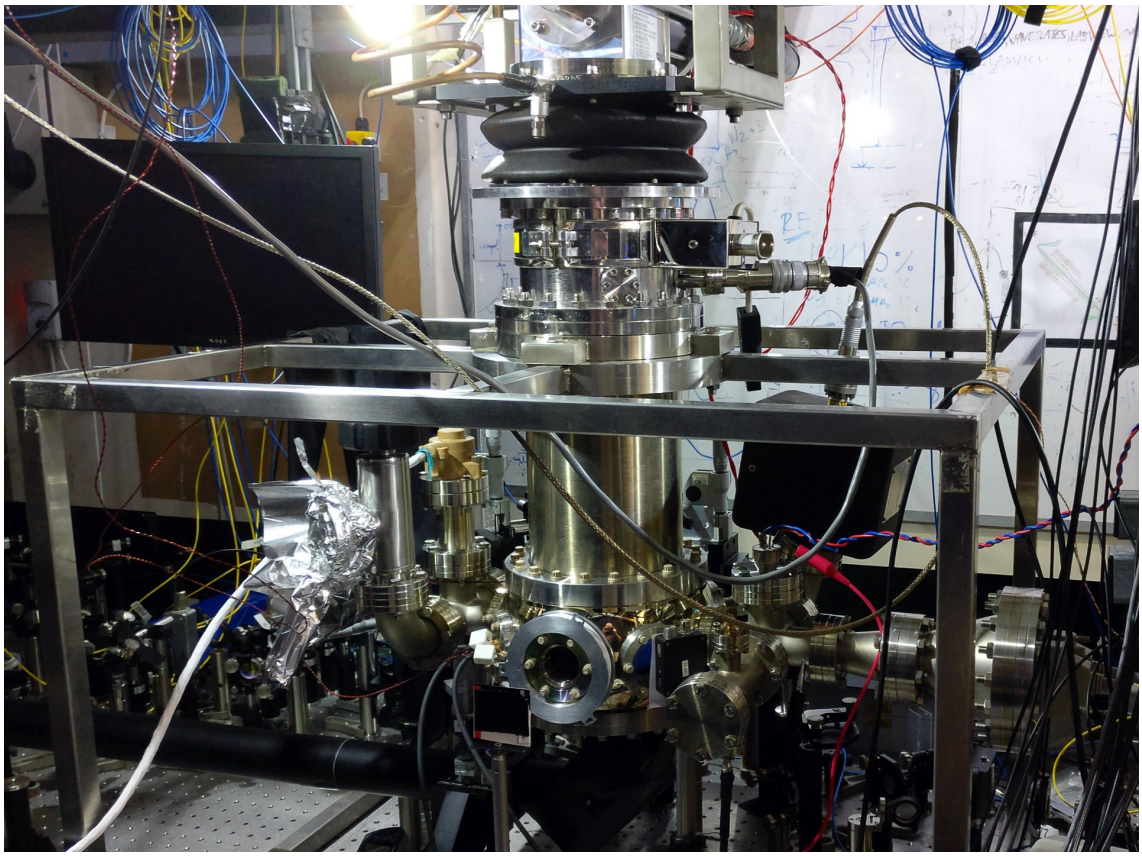

Figure 5.4: Picture showing the fully assembled vacuum system. Clearly visible are the ULVI (top) and the vacuum octagon and imaging optics (bottom).

viewport is designed for a 35mm ion trap surface to window distance and gives a 12 x 12 mm lateral field of view.

5.3 Internal Vacuum Components

5.3.1 Radiation shields

As previously described the majority of the internal structure is cooled down to 4K including the surface trap. If we did not contain the setup within radiation shields two undesirable effects would take place. Firstly external radiation and gas particles from the outer vacuum system and windows would have an unimpeded path to the 4K components. This would add heat load to the cryostat and reduce our useful power budget for the system. More importantly since we wish the cryogenic system to allow for rapid chip testing we do not go through the lengthy baking processes that room temperature systems typically go through that takes three weeks to complete [53]. This means that the non-cryogenically cooled room temperature components within the vacuum system will exhibit a relatively large amount of outgassing resulting in a room temperature vacuum equilibrium pressure of 1×10^{-7} mbar. These gas particles would then freeze on the 4K components resulting in a progressive buildup of a dielectric medium on the surface of the ion trap. This process has been experimentally observed on this cryogenic system.

It is therefore important to surround the cryogenic components in radiation shields. These shields extend the first and second cryostat stages, 50K and 4K respectively, to completely encase the internal components from "line of sight" exposure to the room temperature parts. Figure 5.5 shows a rendering of the two shields without the inner components for clarity. Also shown are the imaging windows and laser access windows.

Figure 5.5 also shows the cold edge that comes from the second stage of the ULVI interface. Wires and cables (not shown) for the DC access and RF/microwave access come through the bottom two access windows shown in the figure, these openings are bevelled with smooth edges so to not cause shorts by cutting through the insulation of the DC wires. The radiation shields are made out of polished oxygen free high conductivity (OFHC) copper as it has a low emissivity which helps minimise black body radiation and it will form a uniform low temperature surface due to its high thermal conductivity which helps improve cryopumping.

Each radiation shield has a large 20 mm radius by 3 mm thick quartz fused silica imaging window which is AR coated for optimal 369.5 nm transmission. The inner shield's imaging window is positioned just 10 mm from the ion position, this brings a risk that any impinging laser light can cause photoelectric charge buildup on the large dielectric surface. This charging would cause problems as the exact level of the charge and its position would

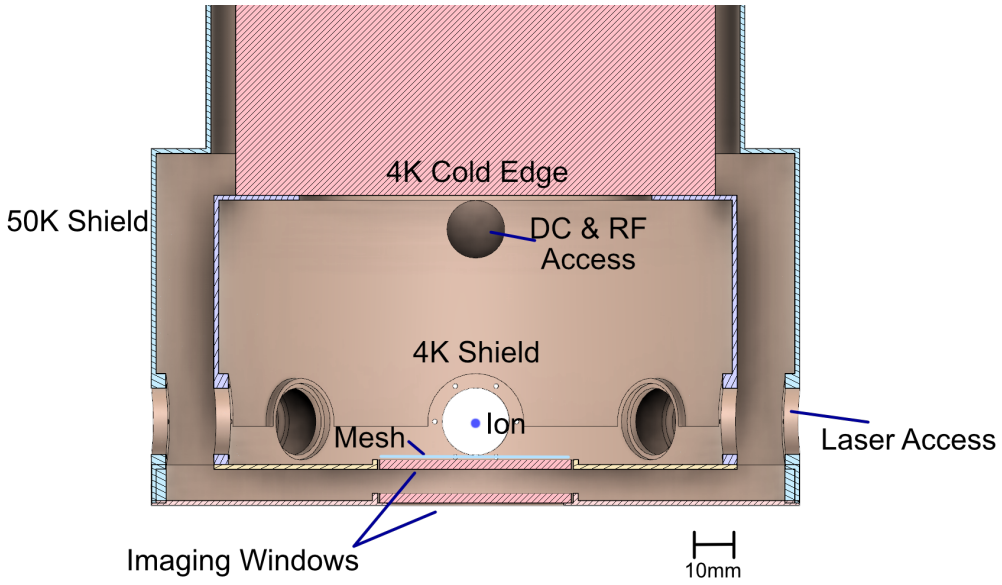

Figure 5.5: Cross-sectional render showing inner and outer radiation shields, 4K and 50K respectively. Also shown are the laser access windows, imaging windows and cold edge of the 4K stage.

be unknown and it would deflect the charged ion. So it was decided to add a fine wire mesh as a Faraday cage to the inside face of the inner most window. While this will block some light from the ion and reduce collection efficiency, the relative obscured surface area is less than 2% of the total window size so the charge screening effect outweighs the loss in photon efficiency. Each window is held in place by gravity as the leading edge of the shield is smaller than the diameter of the silica. This allows the window and copper to expand and contract free of each other and stops the window from shattering.

5.3.2 Laser Access Windows

The principle axis for the system is defined as the axial direction of the linear trap mounted in the system. If a complex geometry trap is used such as an X Junction then one of the linear arms of the trap is designated as the principle axis. The overlapping beams of 399 nm and 935.2 nm come through the window at 0° to the principle axis. The 369.5 nm laser enters through the 45° window to give maximal Doppler cooling in two principle directions. The atomic ovens are mounted at 90° so that no Doppler effect occurs for the 399 nm beam.

To allow for laser access we need to create openings in the radiation shields. These openings would also allow for any non-cryopumped gasses to enter and freeze on the ion

trap. We therefore need to place windows on the inner radiation shield which will block any gasses from entering but allow for the transmission of light.

A method for mounting the windows was then devised that involved creating two PTFE rings that would hold the window gently while two bolts held the rings to the copper shield. This was to allow for thermal expansion and contraction of the silica windows without fracturing them. Table 5.2 shows the thermal expansion of the three materials used for the window mounts.

Material	Expansion coefficient per °C
Copper	17×10^{-6}
PTFE	86×10^{-6}
Fused Silica	0.55×10^{-6}

Table 5.2: Thermal expansion of fused silica, PTFE and Copper

Figure 5.6 shows the window holder. The windows[9] are approximately 2mm smaller in diameter than the window hole in the radiation shield, this allows for thermal expansion without direct coupling between the fused silica and copper and allows them to expand independently.

Figure 5.6: Window holder comprised of two PTFE rings and two bolts that gently hold the window vertical and grip the copper shield.

The two windows used for the 369.5 nm laser path are coated for high UV transmission to reduce the back reflections that would cause increased scatter when imaging the ion trap.

[9] Thorlabs WG40530-C

5.3.3 Internal wiring

To connect ion traps to the outside we need to wire up between 20 to 100 DC connections plus four coax connections depending upon the requirements of the trap.

Due to the large thermal differential between the room temperature side of the cryo-system and the 4K stage we need to use long cable runs to reduce the heat load on the system. The first generation of DC cabling was made out of AWG 36 (0.127mm diameter) enamelled copper wire. This wire was made into a bundle of 100 wires by wrapping the wire between two fixed points 2m apart. Copper rings, to help thermally anchor the bundle, were then placed every 2cm along its length to hold the bundle together.

We can calculate the heat load through this copper bundle using

$$\dot{Q} = \frac{A}{L} \int_{T_1}^{T_2} \lambda(T) dT \tag{5.2}$$

where $\dot{Q}$ is the heat load in W, T_1 and T_2 the two temperatures that form the temperature differential between the two ends of the wire. $\lambda(T)$ is the thermal conductivity of the material. A is the area of the cross-section and L is the length of the wire.

After some experimentation it was decided that larger diameter wire would be needed and that expansion points should be added, which involved leaving small loose sections every half a turn around the radiation shield. These changes were made to make the DC connections more robust when cycling to cryogenic temperatures.

Increasing the diameter of the wire, however, would also increase the thermal load on the system as can be seen from Equation 5.2. So the material was changed from copper to phosphor-bronze wire[10] which has an order of magnitude lower thermal coefficient.

The coax cables used for the RF and microwave delivery in the system are RG316 standard coax cables[11] with a PTFE core and silver plated copper inner and outer conductors. The outer fluorinated ethylene propylene (FEP) coating was removed to improve thermal anchoring by metal-to-metal contact between the copper radiation shield and the silver plated copper mesh of the coax. Figure 5.7 shows the cable wrapping process, on the left the cables start at the top and wind down around the 50K shield in a double helix pattern to the bottom where they enter in through a port hole to the 4K shield inside. The cables then continue to wrap around the 4K shield back up where they enter the inner radiation shield.

[10] Lakeshore WSL-32-250

[11] RS PRO 794-7206

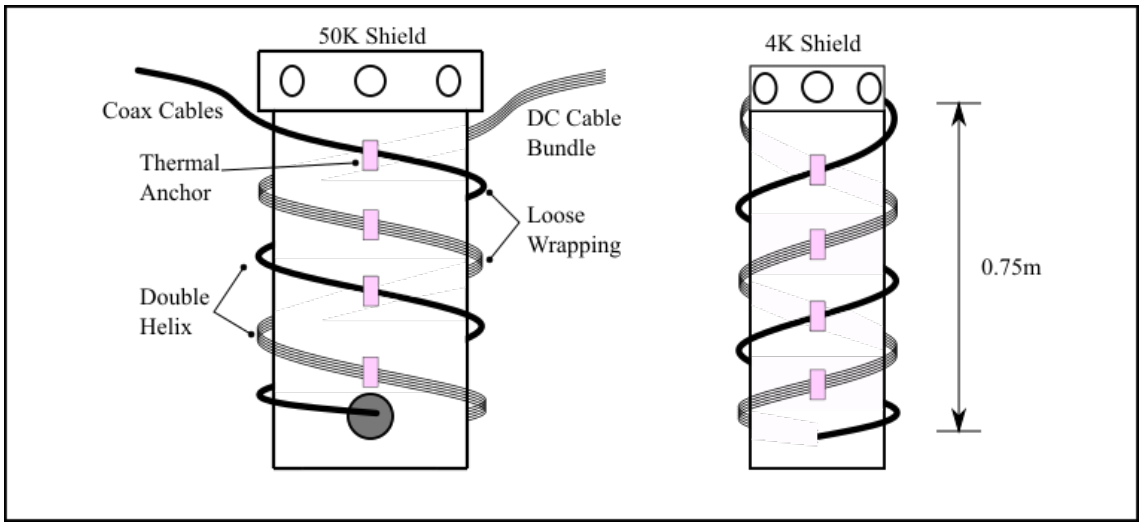

Figure 5.7: Diagram showing the cable wrapping process, on the left the cables are loosely wrapped around the 50K shield in a double helix pattern with thermal anchoring every full turn. On the right the cables pass through from the 50K shield down to the 4K shield where they spiral up and through the radiation shield towards the mounting structure.

Two silicon temperature sensors[12] are mounted inside the vacuum system, one is used for monitoring the 4K cold edge and is mounted directly to the 4K inner shield. The second sensor is connected to the copper chip mount and is used to monitor the temperature as closely as possible to the ion trap. Both of these sensors are connected using quad-twisted phosphor-bronze wires[13] which allows for sensitive temperature measurements.

[12] Lakeshore DT-670B-CO
[13] LakeshoreWQT- 36-25

5.4 Cryogenic Chip Mount

A primary purpose for the cryogenic system is the rapid testing of surface ion traps. To this end we need both a method of creating good thermal contact between the chip and the 4K cold edge and also a method of rapidly ($<$ 24 Hours) changing the chip within the system.

5.4.1 First Generation Chip Mount

The first generation chip mount was created by a previous PhD student Darren De Motte. It involved a custom PEEK receptacle which mated with a ceramic chip carrier shown in Figure 5.8.

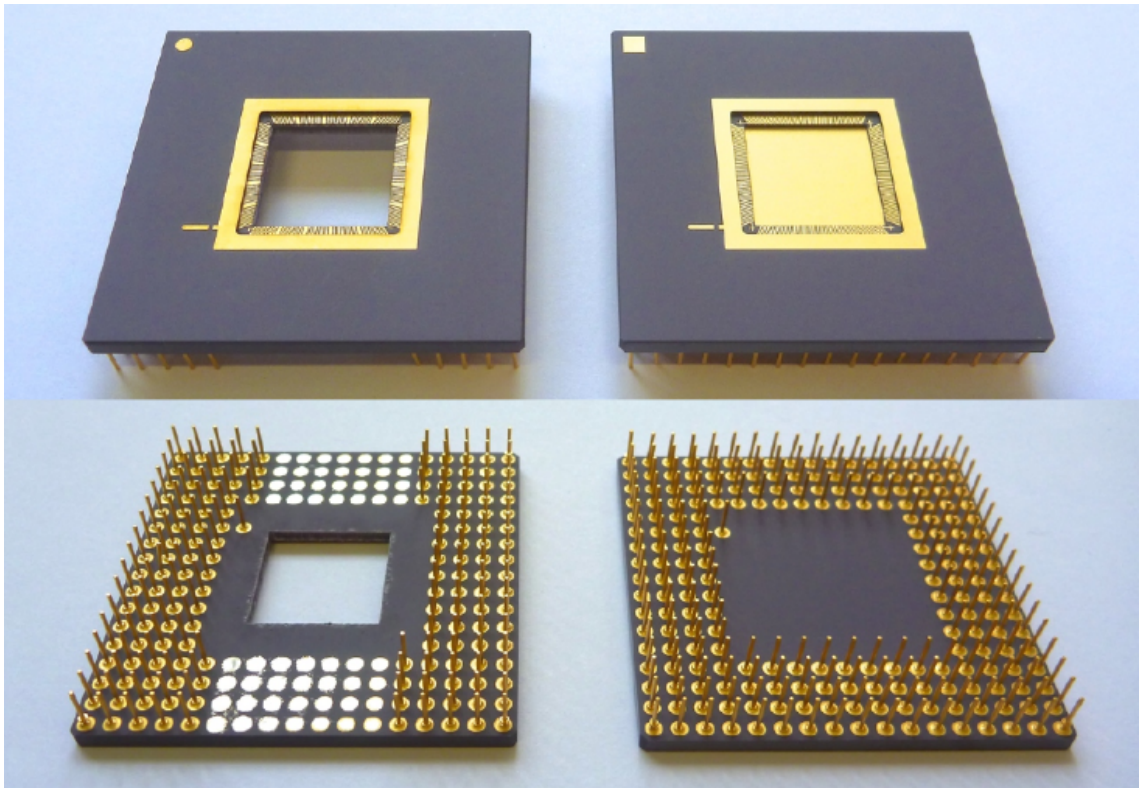

Figure 5.8: Modified and unmodified ceramic pin grid array (CPGA) 208-pin chip carrier (Global Chip Materials PGA10047002). Adapted from [1]

More details on this mounting structure can be found in Darren De Motte's thesis [1]. This mounting structure was unsuccessful primarily due to the insertion force required to push all 208 pins into the mating structure. The force required was beyond what could be achieved by hand and sometimes would split the ceramic mount in half. This left multiple pins unconnected which would leave trap pads floating and make it impossible to form a

workable trapping potential.

5.4.2 Second Generation Chip Mount

The second generation chip mount had to meet a few criteria

- Allow for rapid chip swapping to directly meet the criteria for the system as a whole for testing and developing ion surface traps.
- Be easy to connect without the need for excessive force
- Allow for easy connection testing to check the continuity of the DC connections.
- Be small enough to fit within the inner radiation shield
- High thermal conductivity
- Modular construction to allow for multiple copies of the mount to be created, so that the next ion trap to be tested can be preloaded, cleaned and wirebonded before being swapped with the current trap.

The chip mount is formed of two parts made out of OFHC copper. Figure 5.9 shows the top and bottom chip mounts. The bottom section is mounted to the cold edge of the ULVI interface. It includes a screw mount for the silicon temperature sensor and a 6 mm hole for mounting of a 25 W internal heater[14].

The bottom mount is permanently mounted within the system and not normally removed when traps are changed. The heater is used to keep the chip at a higher temperature, compared to the cold edge and radiation shields, when cooling down the system. Cryopumping is dominated by the coldest parts within the system. Allowing the radiation shields and cold edge to remain 9K lower than the chip by using the chip mount heater, we can reduce the surface coating of cryopumped gasses during cooldown.

The top mount is attached to the PCB which houses the single stage filter and RF SMP connector for the trapping RF. The top mount attaches to the bottom mount with two vented screws. The ion surface trap is mounted directly onto the top copper surface for optimum thermal connection.

[14] Lakeshore HTR-25

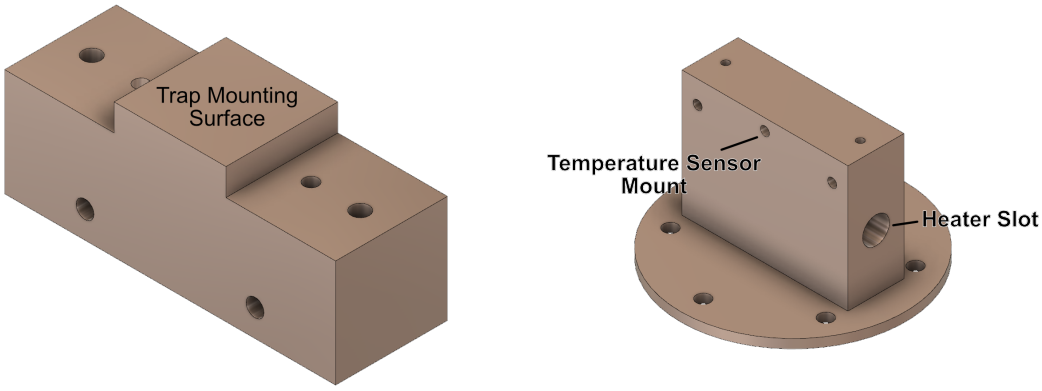

(a) Top Mount (b) Bottom Mount

Figure 5.9: Design of the top chip mount (a) that is removable with two screws for fast chip swapping. The bottom chip mount (b) that is fixed with six screws into the cold edge. Both parts are made out of OFHC copper.

5.4.3 Ion Trap Mounting Methods

There are multiple methods that can be employed for mounting the surface ion trap to the top chip mount.

Epoxy based methods rely on gluing the chip with a two part silver epoxy[15] that is UHV compatible to the copper mount. This method works well for room temperature systems as the chip mount and trap only have to survive the baking process which raises the temperature to around 200 °C. For cryogenic systems, however, there is a large amount of contraction from 300K to 4K and the thermal expansion coefficients of sapphire or silicon are different to that of the copper mount. This results in either the ion trap fracturing or falling off the chip mount entirely. There is also a risk of surface contamination from the two part epoxy as it cures. This is caused by the liquid epoxy being drawn up onto the surface of the trap before it has cured by capillary action, which renders the trap unusable. The other drawback of this method is that the trap cannot easily be removed from the mount making the trap non-reusable.

Surface clamping methods were tried after the epoxy method. These methods involve using metal clamps to physically hold the trap to the surface of the copper mount. They suffer from two major drawbacks however. Firstly the mounts cover some proportion of the chips surface, this means that there is less access for laser light and there must be sufficient surface area to accept the clamp without causing shorts. Secondly, without using

[15]EPO-TEK H21D

any form of underside conductive liquid or soft metal layer, thermal contact is reduced as micro fissures and imperfections on the copper mount will reduce the amount of surface contact between the trap and the mount. Figure 5.10 shows three generations of surface clamps that were tried.

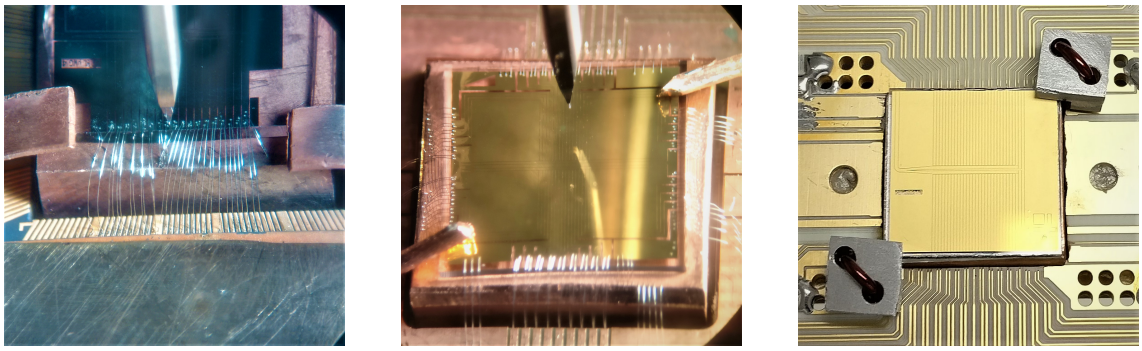

(a) (b) (c)

Figure 5.10: Three generations of surface clamps. (a) metal clamps made from copper sheet, (b) clamps made from copper wire, (c) clamps milled from an aluminium block and tightened with copper wire.

The final method used was indium foil bonding. This method of clamping uses a diebonder[16] to melt a 100 µm thick, 99.999% purity, indium foil sheet[17] under the trap, bonding the trap to the copper mount (see appendix for details of the bonding procedure).

The diebonder used features 5 µm accuracy, a vacuum placement head and vacuum base holder. Dual heaters heat both the base and the head equally allowing for equal thermal stress and faster bonding times. It also features customised temperature profiling which was used to find the optimum flow profile for the indium foil. The flow profile used is shown in Figure 5.11. The initial ramp up rate is $1\,^{\circ}\mathrm{C\,s^{-1}}$ to a fixed temperature of 160 °C which is above the melting point of pure indium (156.6 °C [112]). After holding this temperature for 10 seconds the indium melts and excess indium is ejected out sideways. Then a slower cool down period begins at a rate of $0.5\,^{\circ}\mathrm{C\,s^{-1}}$ until the mount is at room temperature. These ramp parameters were adjusted over multiple bonding cycles to create a bond that would survive the cryogenic cooling process. The most critical parameter was the cooling rate of the diebonding process, if the bond is cooled too quickly it can break the indium seal.

Figure 5.12 shows the three stages of the bonding process. A heated head force of

[16] Finetech FINEPLACER pico ma
[17] Goodfellow IN000230

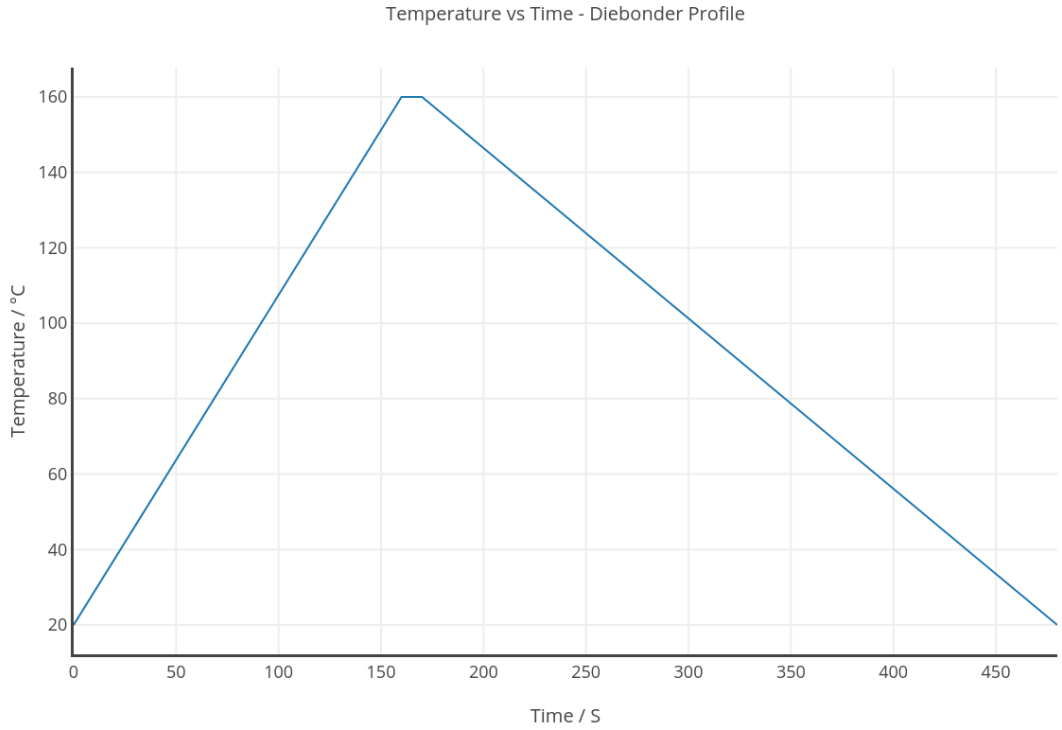

Figure 5.11: Flow profile for the diebonder. Starting profile gradient of $1\,^{\circ}\mathrm{C\,s^{-1}}$, 10 s holding time at 160 °C then a $0.5\,^{\circ}\mathrm{C\,s^{-1}}$ cool down ramp.

1N is applied throughout the heating profile. Once the mount has cooled and before the heated head is removed the excess indium is removed with a scalpel. Then the diebonder vacuum pump is turned off and the mount is ready for wirebonding.

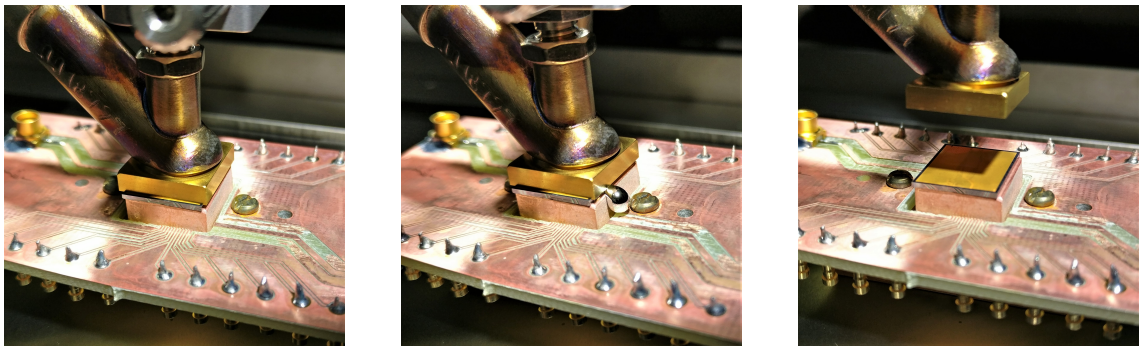

(a) (b) (c)

Figure 5.12: Diebonding process, (a) shows the chip under the heated head before the indium has melted. (b) shows the melted indium ejected out from the sides of the trap. (c) after cooldown and excess indium removal the heated head is raised off the trap.

The diebonded chip mounting method was found to be not only the fastest method of bonding a cryogenic ion trap but also the most reliable. Ion traps have been cycled 10

times from 4K to room temperature with no signs of damage or degradation. Diebonding also results in no problems with optical access and there are no signs of surface damage to the surface of the trap from the diebonder. Diebonding is also reversable by heating up the mount and removing the chip when the indium has remelted, this allows for calibrated traps to be placed in other vacuum systems after testing.

5.4.4 Cryogenic PCB and Wirebonding

Since each ion trap can have very different connection requirements it was important to develop a method of creating the custom PCBs in house. We have a high grade milling machine[18] available to the lab. This machine is able to mill 50 µm isolations with 7.5 µm absolute accuracy on double sided boards.

The PCB material used was Rogers 3003 laminates. These are ceramic filled PTFE laminates that show low loss upto 10GHz and have high thermal dielectric constant stability. These laminates also have a matched thermal expansion coefficient to copper, this allows us to bolt the PCB to the copper mount without relative movement or stress which protects both the PCB and the wirebonds to the ion trap from damage. Normally [53] an electroless nickel electroless palladium immersion gold (ENEPIG) process is performed on the copper surface to protect against oxidisation and give a good surface to wire bond to. Since each PCB is only created when it is required for each trap being tested it was found to be acceptable to leave the pure copper surface as the PCB does not have sufficient time to oxidise before it is placed in the system.

A decoupling (shunt) ceramic capacitor is added on the PCB for each DC electrode with a value of 2 nF. The capacitor' job is to give a short path to ground for any induced RF on the DC electrodes of the ion trap. This ensures that the DC electrodes appear well grounded at 20 MHz. Each DC connection is made to the internal DC wires via socket pins[19].

The high voltage RF signal is delivered to the PCB via the coax cables from the cryogenic resonator. The coax is connected to the PCB by SMP connectors[20] [21] which give a smaller profile than SMA connectors and were tested at cryogenic temperatures without signs of disconnection or degradation.

[18] ACCURATE 627
[19] MAC 8 PD-10
[20] Rosenberger 19K201-302L5
[21] Rosenberger 19S101-40ML5

The final step for chip preparation is wire bonding the PCB traces to the trap electrodes. 25 µm diameter aluminium wire is used with a wedgebonder to triple bond (3 wire bonds per electrode) the PCB traces to the surface electrodes.

Figure 5.13 shows the fully assembled trap that has been indium diebonded to the chip mount and wirebonded, not visible are the decoupling capacitors which are on the underside.

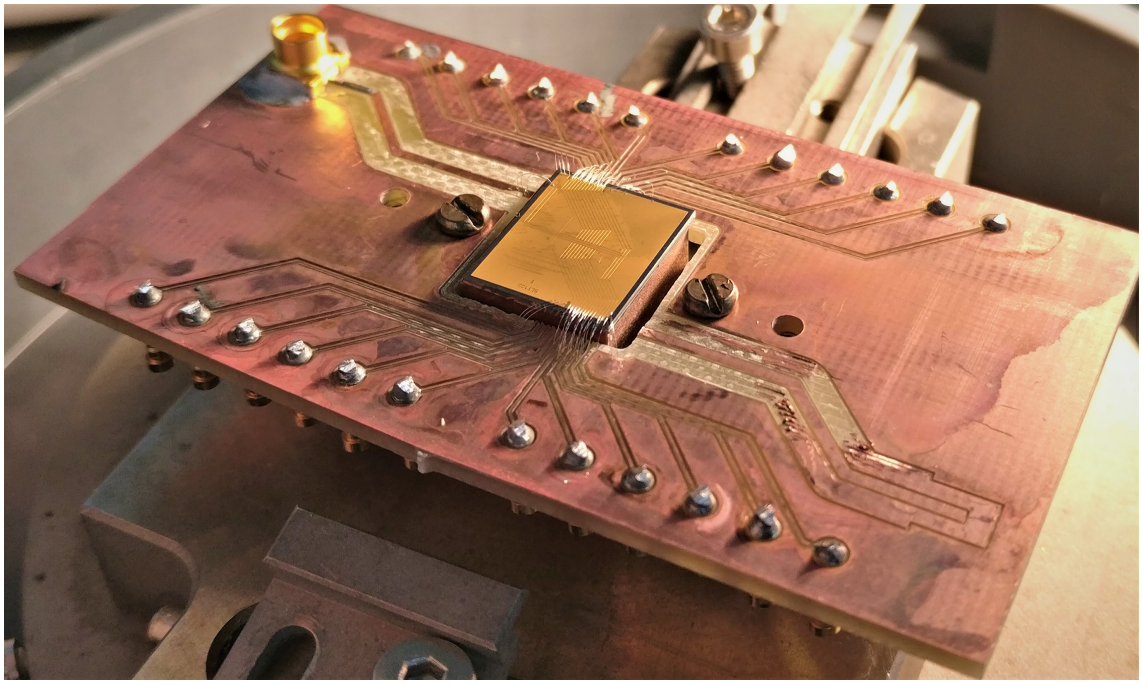

Figure 5.13: Fully assembled trap with PCB and chip mount. Custom PCB is milled from Rogers 3003 substrate. Trap in the picture is a linear surface trap with 24 DC connections and one RF connection. RF SMP connection can be seen in the top left of the image.

5.5 Atomic Oven

To be able to trap reliably we need a method of generating an atomic flux of ytterbium atoms on demand. A lot of work has been done in this direction [53, 1] and the cryogenic ovens in use were created by PhD student Darren De Motte and can be found in his thesis [1] but a brief overview will be given along with the modifications done since.

There are two main methods of creating an atomic flux, one method involves ohmicly heating a sample of the atomic element used for trapping, in this case ytterbium. Ohmic heating has been shown before by multiple systems [44, 53, 113, 114] and involves the application of a large current (7-15A) through a metal tube which contains the atomic element. The applied current causes ohmic heating in the metal tube which heats up and at a critical temperature causes the atomic material to sublimate. The atomic flux is then directed to the ion trap where the appropriate lasers and electric fields are present to trap the ionised atom.

Other methods involving laser ablation have also been demonstrated [41, 109]. Laser ablation uses 1.5 mJ laser pulses that ablate the surface layer of the atomic sample which can then be trapped by an appropriately placed ion trap. Laser ablation methods suffer due to the fact that not only wanted atomic material is ejected from the sample which then is free to coat or disrupt the ion trap. Also laser ablation methods are non directional so the ejected material has a wider field of view than that of oven based sources.

There is a limitation on the available heat budget that can be dissipated into the cryostat. We can increase the available cooling power by mounting the oven onto the 50K shield rather than the 4K shield, as the available power budget for the 50K shield is around 35W. We can increase the efficiency of the atomic oven by directing the power into the ytterbium rather than dissipating it in the wires and metal contacts of the power delivery system and surrounding environment.

The first step is to isolate the oven from the environment by using ceramic spacers (Macor) to reduce the thermal coupling from the core of the oven to the copper shield that the oven is mounted in. The second step is to increase the electrical resistance of the oven compared to its wiring. With a typical oven setup [53] the total connection wiring makes up about 3 Ω while the oven tube only accounts for about 0.1 Ω. So by first principles we can calculate the power dissipated by this oven by,

$$P = I^2 \times R \tag{5.3}$$

where R is the resistance of the conductor, I is the current and P is the dissipated power. So for a given input current we can work out the fractional power dissipated by the wires verses the power dissipated in the oven. So for a $3\,\Omega$ wiring loop and $0.1\,\Omega$ oven resistance it is clear that the faction of power dissipated into the core of the oven is only 3.2%.

In contrast, by using tungsten wire wrapped around a ceramic core we can increase the resistance around the area of the ytterbium sample and increase the efficiency. Since the original work by Darren De Motte the number of turns of tungsten wire was increased to 55 turns, this increases the resistance to $32\,\Omega$, also plug-sockets have been added to the ends of the tungsten wire to allow for refilling which was done during the course of this PhD.

The connecting wires are longer for the cryogenic system compared to a room temperature system[53] so as to be properly thermally anchored, so the total wire resistance is measured at $5.1\,\Omega$ which is higher than for a room temperature system. So with an oven resistance of $32\,\Omega$ and a wiring loop resistance of $5.1\,\Omega$ we get a fractional power dissipation for the oven of 86.2%. This increase in directed power along with the physical design that limits the power coupling into the environment, allows this oven to work in the cryogenic environment with a trapping time (time of oven on till trapped ion) of 9 s with a wire current of 0.4 A and a wire resistance of $32\,\Omega$.

Increasing the current further does reduce trapping times but it also results in more thermal overshoot where the atom flux grows beyond that required to trap and either multiple ions are trapped, which might be undesirable, or excessive coating of the surface of the ion trap occurs unnecessarily.

5.6 Cryogenic RF Resonator

One of the principle requirements to trap ions on a Paul trap a high voltage (100V to 300V peak) RF signal in the 10 MHz to 30 MHz range. There are multiple methods of generating these voltages and in this section we will describe the novel simple design used on the cryogenic system and its measured parameters.

5.6.1 Resonance and Q

In AC circuit theory the fundamental parameter, impedance, is the complex form of the relationship between voltage and current dictated by Ohm's law $Z(\omega)$ [115]. It is defined as,

$$Z(\omega) = R + iX \tag{5.4}$$

where R is the real component of the impedance (resistance), it is the dissipative component of the complex impedance. X is the reactance, it is the imaginary part of the complex impedance and is non-dissipative.

Positive and negative reactances relate the phase angle ϕ, of the instantaneous voltage $v(t)$) to the instantaneous current ($i(t)$. In capacitors, which have negative reactances, the voltage lags the current by 90° and conversely in inductors, which have positive reactance, the voltage leads the current by 90°.

When an inductor and capacitor are placed in parallel we form a resonant circuit, sometimes called a tank circuit [115]. Due to the inverse nature of the current and voltage of the two components when energy enters the combined system it is passed from inductor to capacitor and vice versa at a given frequency f_0 which is related to the component values by,

$$f_0 = \frac{1}{2\pi\sqrt{LC}} \tag{5.5}$$

where L and C are the inductance and capacitance respectively.

With perfect components this resonant frequency would have an infinitesimally small bandwidth, that is to say it is perfectly monochromatic. In reality no component is perfect, capacitors show an effective resistance caused primarily by dielectric losses and inductors have conductor resistance and induced losses such as eddy currents[115, 11].

This dissipation causes the bandwidth to increase making the resonant frequency broader compared to its perfect counterpart.

Bandwidth is characterised by the quality factor (Q), defined as,

$$Q = \frac{E_s}{E_d} \tag{5.6}$$

where E_s is the energy stored and E_d is the energy dissipated per cycle. Q is more often redefined as,

$$Q = \frac{f_0}{\Delta f} \tag{5.7}$$

where f_0 is the frequency of resonance and Δf is the full width half maximum (FWHM) bandwidth of the resonant peak [115]. Since losses come from dissipative parts of the components we can see that the Q will lower as the losses increase or as the components become less "perfect".

5.6.2 Resonant Gain

If we create a series resonant circuit as shown in Figure 5.14 where R1 is the combined loss of L1 and C1, we can analyse the voltage across L1 and C1.

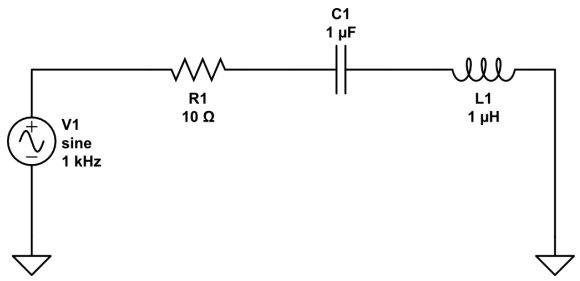

Figure 5.14: Series resonant circuit, where R1 is the combined losses of both L1 and C1.

Since we know that the reactance of the inductor is[115],

$$X_L = \omega L \tag{5.8}$$

we can use ohms law to work out the voltage across the inductor as,

$$v_L = \omega L i \tag{5.9}$$

where i is the instantaneous current and v_L is the voltage across the inductor. From ohms law this current can be defined as,

$$i = \frac{v_s}{Z(\omega)} \tag{5.10}$$

where v_s is the instantaneous source voltage and $Z(\omega)$ is the impedance of the series circuit. Combining equations 5.9 and 5.10 and simplifying at resonance where $X_C = -X_L$ we get,

$$v_L = \omega L \frac{v_s}{R} \tag{5.11}$$

so we can see that it is possible to have a larger voltage across the inductor or capacitor than the source voltage. If we also define Q at resonance as[115],

$$Q = \frac{\omega L}{R} \tag{5.12}$$

then it can be seen that,

$$v_L = Q \times v_s \tag{5.13}$$

so the Q of the system is equivilant to the voltage gain of the LCR circuit. This is how our resonator will create the high trapping voltages we require. Also since the resonator has a low bandwidth it forms a narrow-band band-pass filter which reduces coupled noise from entering the system.

5.6.3 Resonator Design

Due to the trap construction being that of flat metallic surfaces separated by a dielectric medium the ion trap can be modelled as a dominantly capacitive component with an effective series resistance (ESR). It is therefore possible to form a resonant circuit with this capacitance and benefit from the properties of voltage gain as previously described.

The problem to solve now is how to supply the drive power to any resonant circuit and how to maximise the Q as this is our primary voltage gain effect.

There has been much work on helical resonators [116] and their use in ion trapping [117]. It can be seen from Equation 5.12 that to increase the Q we can either increase L or lower R. While different designs can be imagined for the ion trap we still need to trap with the chips that are available to us so we can consider C to be fixed in the short term. Due to the ion stability parameter (q) being frequency dependent as discussed in Chapter 2, we have a limited range of frequencies available to us if we wish to maintain

the required trap depth. This means that to have a stable trap with a trapping RF that satisfies the stability parameter (q), we can change L slightly but most of the Q gain will come from reducing R.

In helical resonators the effective inductance per unit length is much higher than that for an air wound coil or a coax resonator by a factor of typically 10-100 [115, 116]. This means that for a required inductance L less conductor length is required. This reduction in length reduces R substantially which is why helical resonators can typically have Q factors in the 10's of thousands.

Since we are operating a cryogenic system we can utilise the properties of superconductivity to reduce R from conductive losses to zero, the only losses would be from flux coupling effects and radiation resistance which are substantially lower [11]. Much work has also been done towards cryogenic resonators, including cryogenic helical resonators [92], and wire wound resonators [118, 119]. While cryogenic helical resonators have the best Q factors they are physically large, not an inherently scalable technology, and would require significant alterations to the current cryogenic setup to implement.

Wire wound resonators are the best choice for the cryogenic system and it is here that we began testing different topologies. We started by replicating the resonator design by Gandolfi *et al.* [118].

This resonator design is a series LC circuit where the C comes from the ion trap and the L is a wire wound coil such that the resonant frequency of the two was 10.1 MHz. As previously described a series resonant circuit at resonance ($X_C = -X_L$) has a very low impedance which is usually in the order of a few ohms. For our circuit it was measured at 4.3(1) Ω at room temperature, using a vector network analyser (VNA)[22], details of the measurement process are covered in Chapter 5.9.

5.6.4 Matching Networks

Due to the requirement for having 2m long cables for RF delivery due to thermal anchoring reasons and minimising heat load on the cryostat, we need to use coax cables as they are a properly matched transmission line and therefore they do not add residual inductance or capacitance when properly matched at both ends. This ensures maximum power transfer to the resonator. At the source the amplifier and generator are both matched internally to 50 Ω and the coax cable chosen has a characteristic impedance of 50 Ω. We therefore need a method of matching the low impedance of the resonator-chip combination to the

[22] Rohde & Schwarz ZNB20

coax cable.

The method used by other cryogenic ion trapping groups [118, 119] and our first generation resonator involves building an L-match circuit which consists of an inductor in series and capacitor in parallel with the load.

As we have measured the load impedance to be lower than $50\,\Omega$ and since we require a DC path to ground, to stop the buildup of charge on the RF electrode, the only possible topology for the L-match is a parallel capacitor first followed by a shunt inductor.

We can see that the L-match is basically a filter. The Q_{filter} factor of the filter is related to the load and source impedance by [115],

$$R_{source} = R_{load}(Q_{filter}^2 + 1) \tag{5.14}$$

where R_{load} is the load resistance and R_{source} is the source resistance when $R_{load} < R_{source}$.

We then calculate the series reactance required, X_S, and the parallel reactance, X_P, using

$$\begin{aligned} \frac{1}{\omega C} \equiv X_P &= \frac{R_{source}}{Q_{filter}} \\ \omega L \equiv X_S &= R_{load} Q_{filter} \end{aligned} \tag{5.15}$$

We can then for a given frequency calculate the required L and C values to match the $50\,\Omega$ source to the $4.3\,\Omega$ load of the resonator. For $10.1\,\text{MHz}$ this becomes $L = 221nH$ and $C = 1.03nF$. By making the matching capacitor variable you can tune the matching network to get a better match to the trap-resonator circuit.

The issue arises with this topology is that when the cryosystem cools down to 4K the trap capacitance and effective series resistance (ESR) do not scale the same as the matching network. This means that the two resonant circuits become unoptimised at cryogenic temperatures. This can be calibrated out by measuring the impedance with a VNA when the system is at cryogenic temperatures, then upon warming up the variable capacitor can be adjusted to mismatch at room temperature by the same magnitude but opposite phase to the mismatch measured at cryogenic temperatures. Then when cooling down again the system will match. This double cooldown process would have to be performed for every trap tested which is undesirable.

5.6.5 Autotransformer

The chosen method of matching is by using a transformer based design. A traditional double wound transformer consists of two windings denoted as primary and secondary, usually wound around a common core such that magnetic flux is coupled between the two. Transformers are commonly used to change the voltage supply range between AC circuits by the ratio of their windings given by [115],

$$\frac{V_P}{V_S} = \frac{N_P}{N_S} \tag{5.16}$$

where V_P and V_S are the voltage on the primary and secondary respectively, N_P and N_S are the number of turns of the primary and secondary respectively. Since we define impedance on the primary as,

$$Z_P = \frac{V_P}{I_P} \tag{5.17}$$

where Z_P is the impedance of the primary, V_P is the voltage and I_P is the current of the primary. Due to the conservation of energy we can see that as we change the winding ratio we swap from voltage to current, this is equivalent to saying that we change the impedance of the line by changing the ratio.

If we add a capacitor to the secondary to form a tank circuit we create a resonant transformer. By using resonance and setting the primary to secondary ratio correctly we can couple power optimally into the tank circuit in a similar way to how the L-match functions.

To aid in the construction of the transformer and to maximise the inductance which gives the maximum possible Q by Equation 5.12, we can build a different style of transformer called an autotransformer. Figure 5.15 shows the circuit diagram of the full resonator setup used on the cryogenic system that replaced the L-match first generation resonator. The transformer is wound with NbTi superconducting wire around a PTFE core which gives physical support with minimal inductive losses. Since the voltage is high and the current is low in between the coil and the trap by our definition of impedance in Equation 5.17 we can see that this point is high impedance. As we move the input "tap point" as seen in Figure 5.15 away from the ground plane the impedance of the "tap" rises. This would be the same as increasing the number of turns on the primary of a double wound transformer. Since the autotransformer coil is both the primary and secondary, moving the "tap" does not change the resonant frequency.

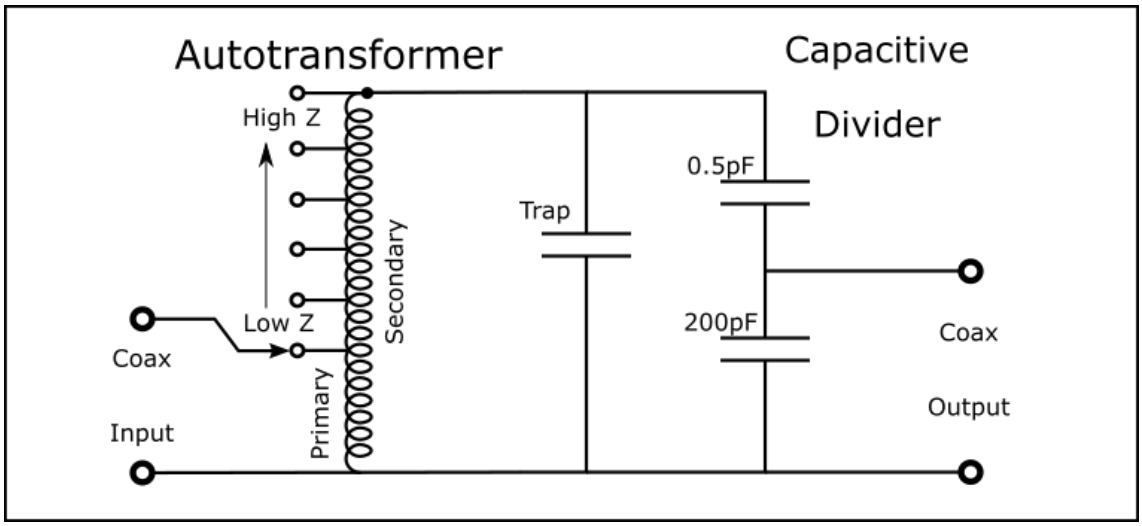

Figure 5.15: Circuit diagram of the autotransformer resonator used in the cryostat circuit. The autotransformer is "tapped" to tune the optimum input impedance as close to 50 Ω as possible. The capacitor divider is used to create a high impedance monitor point to measure the trap voltage via an external scope.

Once the coil-trap frequency has been set, the outer enamel insulation of the superconducting wire is removed with a small file and a wire "tap" can be moved up the coil until 50 Ω input impedance is found where it can then be soldered in place. The output capacitive divider seen in Figure 5.15 is used to monitor the trap voltage.

The autotransformer is used as the resonant coil of the trap tank circuit, therefore it is both the impedance match and voltage gain component in a single device. While the input impedance is now at 50 Ω the point between the autotransformer coil and the trap is of high impedance. If this point was directly loaded with a coax cable and oscilloscope with a typical input impedance of 16 pF and 1 MΩ it would load the resonant circuit making it impossible to generate the necessary voltages needed for trapping. By using a capacitive divider we create an additional impedance transform by sacrificing measured voltage amplitude. The equation governing the capacitive divider is [115],

$$V_B = V_T * \frac{C_T}{C_B} \tag{5.18}$$

where V_B is the voltage across the bottom capacitor, V_T is the voltage across the total divider, C_T is the total combined capacitance of both capacitors in series and C_B is the capacitance of the bottom capacitor. For the values in Figure 5.15 we get a total capacitance of $C_T = 0.499pF$ which gives a dividing ratio of 401. So for a trap voltage of 300V we would measure around 0.748V. Due to the large capacitance per unit length of coax

cable when not matched to 50 Ω the measured bottom capacitor value when loaded with 2m of coax cable and the scope was 511 pF $\pm 2pF$ this gives a measured voltage of 0.293V.

The trap capacitance range varies between 8 pF to 33 pF. For an autotransformer with 21 turns the 50 Ω "tap" point was experimentally found to be at 1.5 turns, we can therefore estimate the end impedance as 700 Ω. We measured a variation in the end impedance of 37 Ω across the 15 tested traps. This only has a "tap" point variation of around 0.3 ± 0.1 of a turn. We can therefore see that the autotransformer topology is insensitive to a wide range of trap capacitances while still maintaining a cryogenic Q factor of 173 when the cryogenic wire is below 12K. This also makes this topology insensitive to trap variations caused by being cooled down to 4K.

5.7 Cryogenic Microwave and RF Antenna

For addressing the internal states of the ytterbium ion we need to generate RF and microwave (12.6 GHz) fields. For room temperature systems [53] it is possible to mount external coils and microwave horns around the imaging optics.

With cryogenic systems the ion is much further away from the outer window, in addition there are two radiation shields in between which makes external setups undesirable. Ion trapping setups which have internal microwave horns have been demonstrated [120]. These microwave horns are relatively large ($\approx 33mm$ long) and it would be difficult to fit such a horn within the cryogenic setup. So another form of internal antenna is required.

5.7.1 Antenna theory

There are hundreds of types of antenna [11] for different frequency bands and radiation patterns. They broadly fall into two categories, resonant and non-resonant antennas.

Resonant antennas are ones which cause a standing wave to form at the antenna's operating frequency. An example of this kind of antenna would be a dipole.

In a centre fed (current fed) dipole the balanced transmission line enters the antenna in the middle as shown in Figure 5.16.

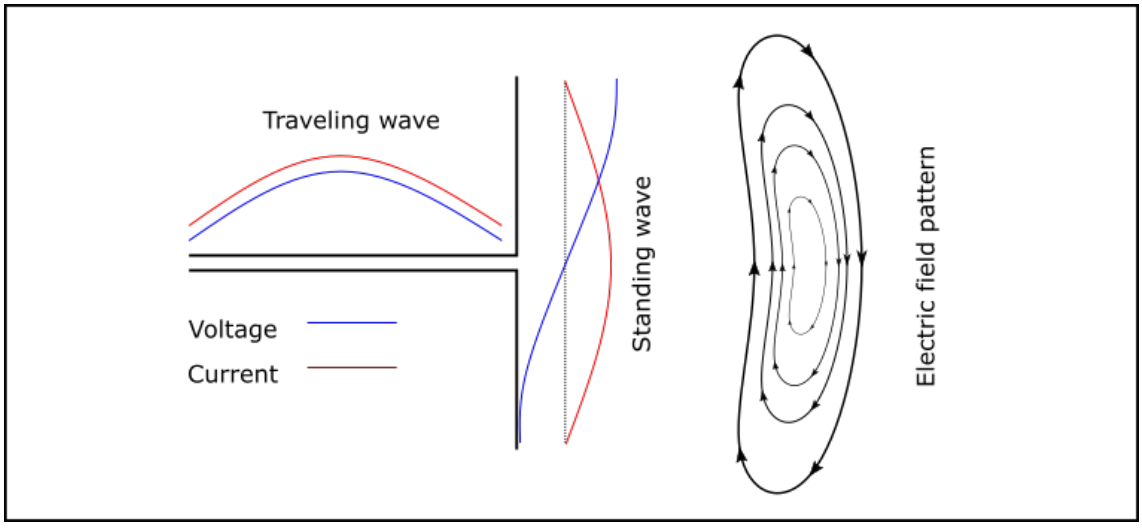

Figure 5.16: Centre fed (current fed) dipole with current and voltage plots. The standing wave on the dipole forms a loop electric field half a wavelength away from the antenna. This folded electric field propagates away from the antenna in a torus radiation pattern.

The travelling wave on the transmission line imparts its energy onto the dipole which

acts like a high Q resonator forming a standing wave where the current is maximum in the centre and zero at the edges while the voltage is 90° out of phase being maximum and minimum at the ends of the antenna and zero in the middle.

Non-resonant antennas are loaded at the end of the emitting section such that there is no impedance mismatch, no reflected power and therefore no standing wave. Examples of such antennas are long wire antennas and helical antennas to name a few[11].

Antennas take energy out of the transmission line and radiate it away. This is a form of dissipation, similar to that caused by a resistor of an appropriate value. This effective resistance is called the radiation resistance and is geometry dependent. It is also a measure of how efficient an antenna is at radiating for a given input current.

5.7.2 Patch Antenna

As mentioned there are hundreds of antenna designs. We require the antenna to be physically small so that it will fit within the cryogenic environment without major alterations. We also need a forward dominant radiation pattern. This means that the radiated power is directed towards the ion and not backwards or sideways.

It was decided that the best candidate would be a patch antenna. Although patch antennas have relatively low efficiencies compared to waveguide antennas due to the presence of dielectric losses and very high Q which makes them narrow bandwidth [11], they have one of the smallest footprints compared to other microstrip antenna designs and they can be made with our PCB miller.

Figure 5.17 shows a typical patch antenna that is microstrip fed from the left edge. The longest edge is the length (L) which is also the direction of polarisation, ϵ_r is the dielectric constant of the substrate.

There are multiple methods of feeding into the patch. One method is already shown in Figure 5.17 and involves connecting a microstrip line to the edge of the patch. Typical edge impedances range from $200\,\Omega$ to $330\,\Omega$ so the microstrip line needs to impedance match to the edge. This style of feed has the broadest bandwidth but also requires the most space around the patch [11]. Other methods include aperture coupled and proximity coupled but since the feed line into the system is a coax cable, a probe fed method was used.

Figure 5.18 shows a probe fed patch antenna where the probe is usually the central

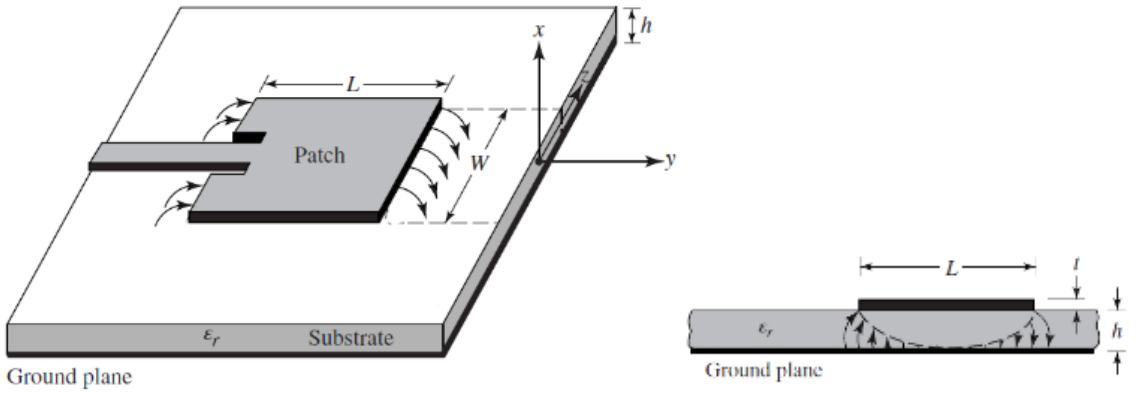

(a) (b)

Figure 5.17: A patch antenna. (a) shows the top of the patch with the radiative electric field lines along the short edge (W). (b) shows the side on view of the patch and the electric field line density. L is the length of the patch and the direction of polarisation, W is the width. h is the dielectric thickness and t is the conductor thickness. Adapted from [11]

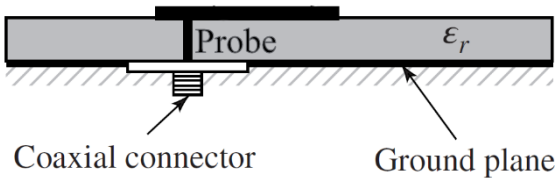

Figure 5.18: Probe fed patch antenna. The central core of the coax passes through the dielectric and bonds to the surface conductor. The position of the feed from the centre determines the impedance.

core of a coax cable. The probe fed antenna has a narrower bandwidth than the edge fed design and suffers from slight edge fringing of the electric field but it is the easiest design to implement with a coax fed source.

There are three main methods used to calculate the dimension of the patch antenna and model its behaviour. The simplest method is the transmission line model [121, 122]. This model is the least accurate method but it gives a good enough result to understand the principles behind the patch and can be used as a starting point before using another model for higher accuracy.

Full wave modelling gives the best accuracy and is the most complex. This style of modelling is beyond the scope of pen and paper calculations but it can be used in the form of commercial software suites such a Comsol or ADS which uses full wave methods

to calculate the fields. This model is also the least intuitive [123, 124, 125].

Since we have Comsol in our lab we will start by calculating the required antenna size with the transmission line model. This model will then form the starting basis for the Comsol simulation which will then be used to optimise the size and probe position.

5.7.3 Patch Transmission Line Model

In this model the patch antenna is described as two radiating narrow slots, each has a width W and a length L separated by a distance S [121, 122]. This two slot approach does not reflect the physical layout of the patch but forms the basis for the mathematical model. Figure 5.19 shows the physical layout of the patch on the left (a) and the equivalent circuit model of the two thin radiating slots represented as two admittance's (b).

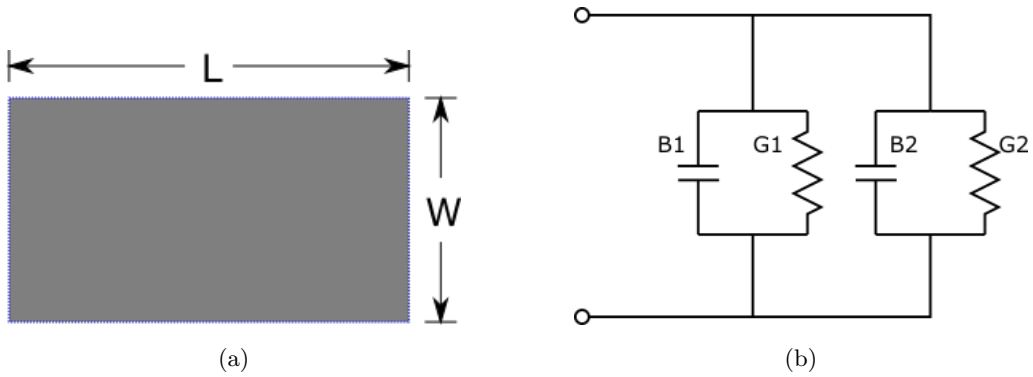

(a) (b)

Figure 5.19: Patch and the equivalent circuit model under the transmission line model. (a) The physical patch with length L and width W. (b) Circuit model for the admittance parameters of the two slots. G1 and B1 are the two "virtual" components of the model that represent slot one, G2 and B2 are the two "virtual" components of the model that represent slot two which are used in the models approximation.

The substrate used for the antenna is Rogers 3003 series. Table 5.3 has the required substrate parameters, where $tan\delta$ is the dielectric loss factor (0 is ideal).

Substrate	Thickness (mm)	Frequency (GHz)	ϵ_r	$tan\delta$
Ro 3003	1.575	0-40	3.00	0.0010

Table 5.3: Table of important physical parameters of the patch antenna substrate.

The first step for designing an efficient rectangular patch antenna is to design its width W. The following equations for designing the patch under the transmission line model are

derived by Belanis [11] and are found on pages 788 to 815. The width is give by,

$$W = \frac{c}{2 * f_r}\sqrt{\frac{2}{\epsilon_r + 1}} \tag{5.19}$$

where W is the width, c is the speed of light in a vacuum, f_r is the radiation frequency and ϵ_r is the dielectric constant of the substrate dielectric. For Rogers 3003 and a frequency of 12.6 GHz we get a design width of 8.412 mm.

Due to fringe effects we now need to calculate the effective dielectric constant. This is because the edge effects make the antenna look longer than expected [121, 122].

The effective dielectric constant is approximated by [126],

$$\epsilon_{reff} = \frac{\epsilon_r + 1}{2} + \frac{\epsilon_r - 1}{2}[1 + 12\frac{h}{W}]^{-1/2} \tag{5.20}$$

where h is the dielectric height and W is the width previously calculated. This equation only applies when the width of the patch is greater than the dielectric thickness. We calculate an effective dielectric constant of 2.555.

We now calculate the length extension caused by the fringe effect, ΔL. This is approximated by [126],

$$\Delta L = 0.412\frac{(\epsilon_{reff} + 0.3)(\frac{W}{h} + 0.264)}{(\epsilon_{reff} - 0.258)(\frac{W}{h} + 0.8)}h \tag{5.21}$$

We calculate a length extension of 0.7361 mm. We now estimate the proper length using

$$L = \frac{1}{2f_r\sqrt{\epsilon_{reff}}\sqrt{\mu_0\epsilon_0}} - 2\Delta L \tag{5.22}$$

where μ_0 and ϵ_0 are the permeability and permittivity of free space. We calculate the proper length as being 5.970 mm.

Our patch model dimensions are $W = 8.412mm, L = 5.970mm$. The next step is to calculate the probe position. We know from antenna theory that the current is maximum in the centre of the antenna and the voltage is zero. As we move towards the edge the voltage rises and the current drops to zero. From Equation 5.17, we know that the impedance in the centre will therefore be zero and it will rise to the edge impedance on the edge.

We can approximate the edge impedance R_{in} by[127],

$$R_{in} = 90\frac{(\epsilon_r)^2}{\epsilon_r - 1}(\frac{L}{W}) \tag{5.23}$$

which gives us an edge impedance of 287.4 Ω. The impedance scales as,

$$R(y) = R_{in} cos^2(\frac{\pi}{L} y) \tag{5.24}$$

where $R(y)$ is the impedance at position (y) where $y = 0$ is defined as the leading edge. Figure 5.20 shows a plot of the impedance along the length of the patch.

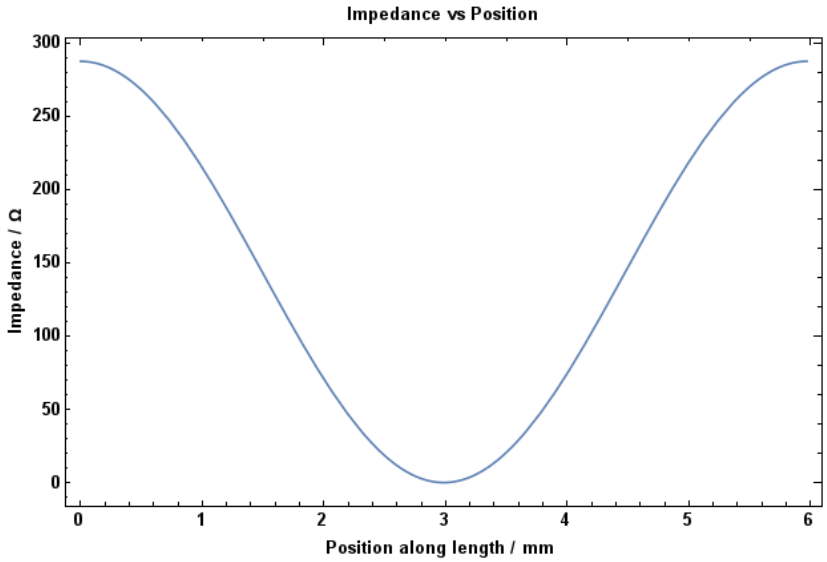

Figure 5.20: Graph of impedance long the length of the patch.

We need to calculate the position where the impedance is equal to 50 Ω. It is visible in Figure 5.20 that there are two positions, either side of the centre, that meet this criteria. We calculated a probe position of 2.167 mm from the leading edge. We now have all the dimensions required to perform the full wave calculations using Comsol, Table 5.4 shows the starting patch criteria.

Substrate	Rogers 3003
Patch Width	8.412mm
Patch Length	5.970mm
Feed position	2.167mm

Table 5.4: Transmission line model patch

In Comsol we build the patch using the calculated dimension and dielectric substrate. We also can perform an optimisation routine with the dependent variables being the width, length and the probe position. The optimisation criteria is the minimisation of the single port scattering parameter S_{11}. This parameter is the complex voltage ratio of the reflected

wave to the incoming wave at a given frequency $\frac{b}{a} = S_{11}$. The lower this parameter the better the match of the patch at the drive frequency.

Figure 5.21 shows the far field plot of the antenna after optimisation, a 2D slice is shown (b) which is taken as the YZ plane of the 3D plot (a). For a 1W input source the maximum normalised far field electric field strength is $1.62\,\mathrm{V\,m^{-1}}$ using the Stratton-Chu fomula [128] for mapping the near field boundary to the far field as the distance from the antenna approaches infinity.

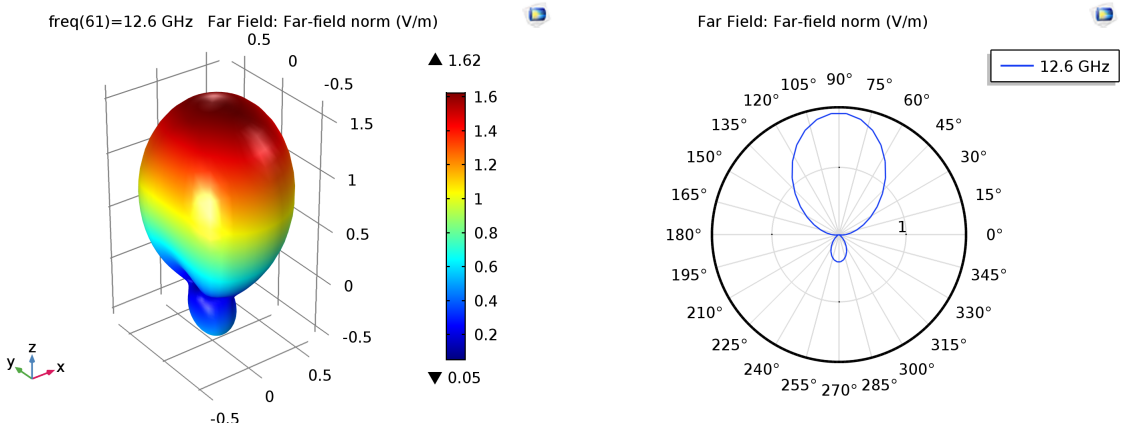

Figure 5.21: (a) shows the far field plot of the patch. (b) a 2D slice along the YZ plane of the far field plot.

Figure 5.22 shows the S_{11} value for the optimised antenna. The minimum S_{11} parameter occurs at 12.590 GHz with $-18.98\,\mathrm{dB}$.

The final patch parameters optimised by Comsol were a length of 5.153 mm, width of 5.469 mm and a feed position of 1.497 mm.

Since the patch will be mounted at 25 mm from the ions position we also need to calculate the near field magnetic field strength of the microwave radiation as the separation $S < 2\lambda$. Comsol gives a near field strength of 611 pT for a 1W source at 25 mm.

Since we will be using the patch at cryogenic temperatures we also need to take into account thermal contraction on the patch which will reduce its size. Rogers 3003 has the same thermal expansion coefficient as copper to $-50\,^{\circ}\mathrm{C}$. While there are no tests we could find for Rogers at 4K for antenna design we can use the expansion of copper as an approximation. Copper has an expansion ratio $\Delta L/L$ of around -0.26% from 300K to 4K[129], this means that we should increase every dimension by 0.26% to compensate.

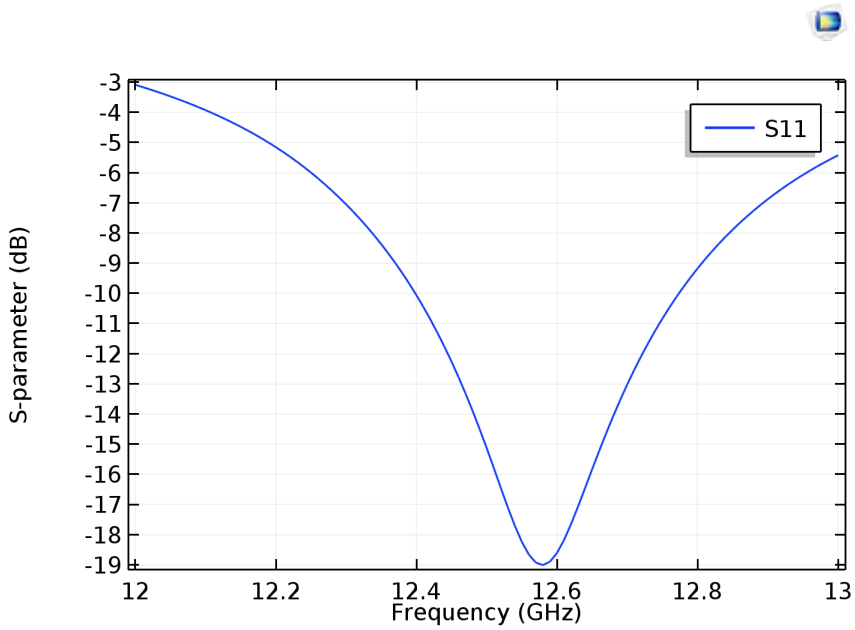

Figure 5.22: Single port scattering parameter after optimisation routine.

5.7.4 Patch testing and mounting

The patch was milled from Rogers 3003 substrate using the same miller that was used previously to create the trap PCB. The dielectric size and ground plane were milled to be 10x10mm with the patch milled onto the top surface. A 0.8mm hole was drilled at the calculated probe position.

The optimum angle and polarisation for the microwave and RF radiation has been calculated before[53, 120], to optimally excite Ω_+, Ω_- and Ω_π Rabi frequencies the microwave Poynting vector (S) should enter at an angle of 45° to the magnetisation axis of the ion. The microwave magnetic field polarisation should also be angled 45° to the normal of the ion trap surface.

The patch was mounted into a milled holder made from PTFE. Testing of the patch antenna was done by mounting the PTFE holder into a lens mount on a angular rotational base. A near field probe[23] was used with a VNA to test the angular field pattern at the same distance that the ion would be compared to the patch. The patch was created 0.5 mm larger in all dimensions, the patch was then trimmed down to size with a scalpel until it matched at 12.6 GHz.

The patch was mounted into one of the window mounts of the 4K shield. Figure 5.23 (a) shows the milled patch under the microscope and (b) the completed mount with surrounding RF coil.

[23] Flann Series 246 12.6GHz

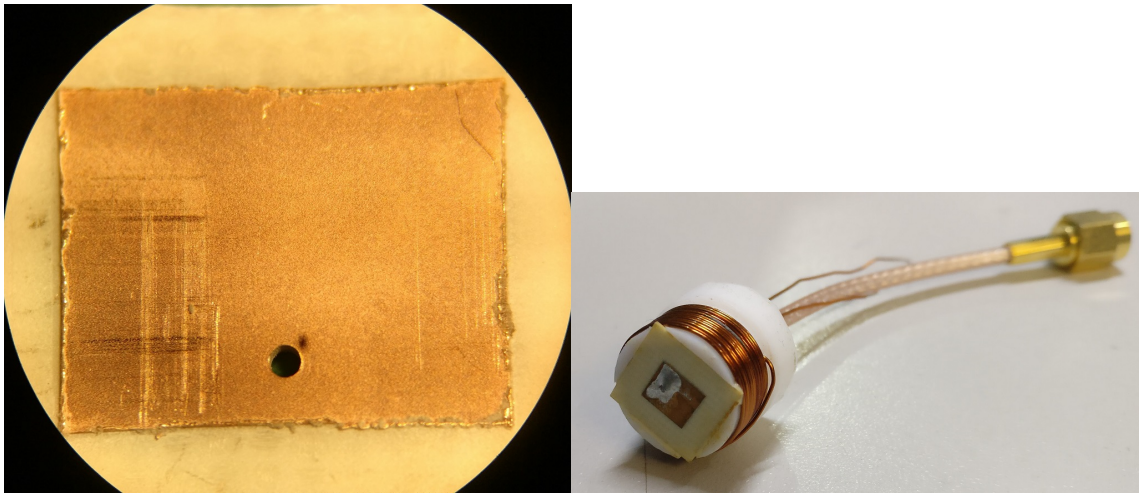

(a) (b)

Figure 5.23: (a) Milled patch on Rogers 3003 substrate. (b) The full RF and microwave assembly with coax feed and SMA connector.

5.7.5 RF Emitter

The RF coil is made from 12 loops of superconducting wire. This antenna diameter (12 mm) is much smaller than the wavelength of the radiating energy (≈ 10 MHz) therefore the antenna is very inefficient [11] but this style of antenna has been successfully used on other ion trap systems [53] except mounted externally.

Figure 5.24 shows the mounting position and the vectors of the radiation compared to the ion trap and magnetic field direction.

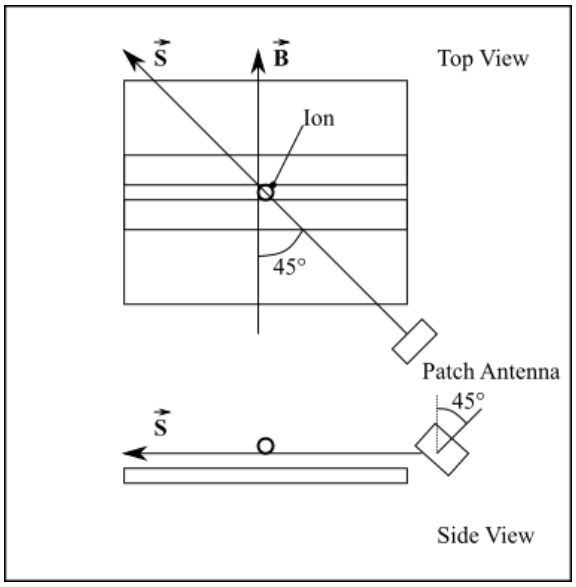

Figure 5.24: Microwave patch antenna Poynting vector and magnetic field vector shown relative to the ion trap. The antenna is mounted at 45° to the matnetic field vector and also rotated 45° to the surface normal of the trap.

5.7.6 Magnetic Field Gradient Coils

For creating the magnetic field polarisation axis or high field gradients for quantum logic operations we need to create suitable internal field generating coils. A previous PhD student Darren De Motte created an internal mount for permanent magnets that were to be used for generating high field gradients[1]. Due to changes in the trap geometry and the lack of on chip microwave resonators we can no longer use the permanent magnet design so a new design was needed.

It was decided to use superconducting coils mounted onto the radiation shield similar to how the microwave patch was mounted. While the gradients would be limited with coils compared to the permanent magnets, they have the benefit that during shuttling they can be turned off and each coil can be driven with unequal currents allowing for tuning of the magnetic null position.

Figure 5.25 shows one of the pair of coils made for the cryogenic setup. Each coil is mounted on a PTFE holder that gets screwed into the 4K radiation shield.

We can calculate the field strength with Comsol and a simulation was setup with the two coils separated by 52 mm, each with a diameter of 16 mm in an Anti-Helmholtz configuration. Due to the space required for the cryogenic chip mount and PCB the coils are further apart than a true Anti-Helmholtz configuration and so the gradient will be sub-optimal.

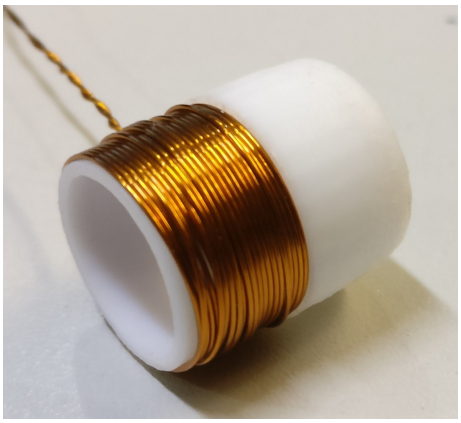

Figure 5.25: Image of one coil. 121 windings in four layers of superconducting NbTi wire. Mounted on a PTFE holder.

One of the coils is mounted around the atomic oven but without physical contact to the copper shroud of the oven, this is to stop heat from conducting into the coil and raising its temperature past the critical temperature of the NbTi wire. Figure 5.26 shows a plot of the simulated magnetic field gradient of the coils through their principle axis. For 121 turns in four layers of superconducting wire passing 10A we get a maximum simulated magnetic field gradient of $11.85\,\mathrm{T\,m^{-1}}$. The wire diameter, number of turns and drive current were chosen due to the constraints on space within the system, heating caused by the non-superconducting feed wires, critical current point of the wire and achieving the highest magnetic field gradient possible.

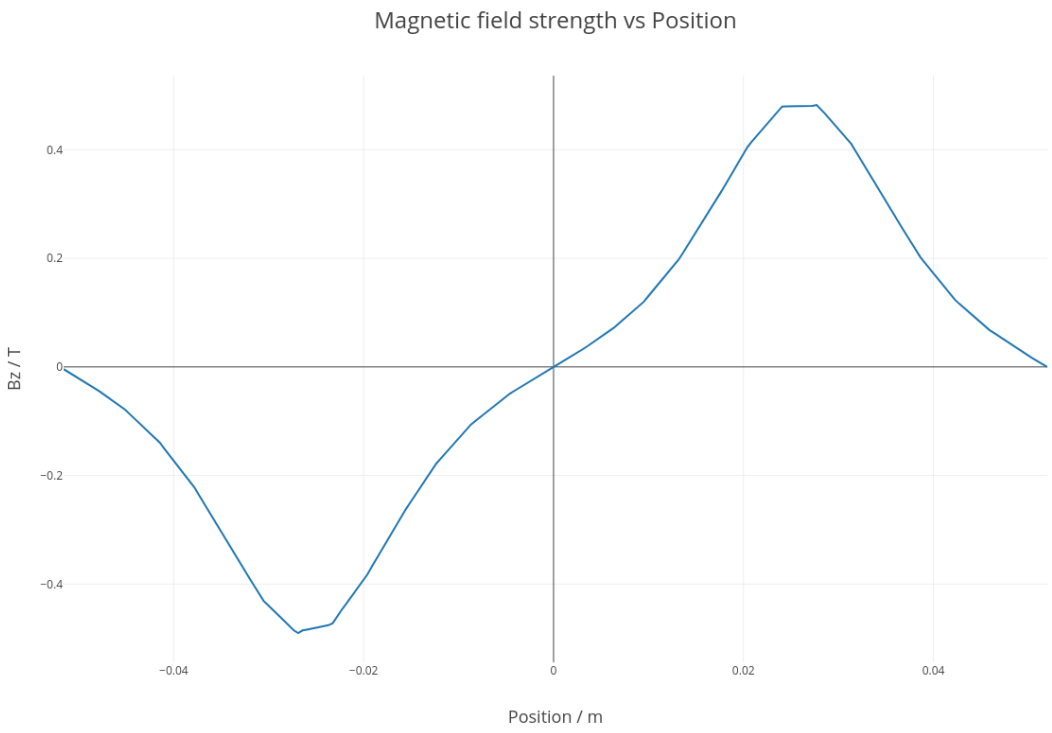

Figure 5.26: Graph of the simulated magnetic field strength along the coil principle axis. In the centre at the ion position the gradient is $11.85\,\mathrm{T\,m^{-1}}$.

5.8 Conclusion

In this chapter I have set out to describe the internal structures of a cryogenic vacuum system for the purpose of ion trap research. While cryogenics has many engineering challenges it also allows us to perform rapid chip testing and development.

I described the creation of cryogenic temperatures by the use of a closed cycle cryostat, and how we can mitigate the vibration caused by that cryostat by the use of a ultra low vibration interface with helium buffer gas.

I then described the internal radiation shields, atomic oven and mounting structure for creating a quick turnaround trapping system in the vacuum environment.

I also described the motivation of designing a cryogenic resonator and showed the progression from an L-match design to an autotransformer resonator.

Finally I described the design process and creation of a cryogenic microwave and RF emitter. I then ended with the design of the gradient coil design and the simulated results from Comsol.

In later chapters I will discuss the results that this system generated from multiple traps which were changed over within a 24 hour period showing that the system is capable of rapid deployment.

5.9 Characterisation of the ion traps

With microfabicated surface ion traps forming the core component of our proposed quantum computer, the rapid development and testing of these very delicate devices is key to successfully creating a scalable quantum computer.

There are many scientific fields that culminate together to produce these surface ion traps including material science, microfabrication engineering, computer science and quantum physics. Surface traps are first designed with a desired trapping field profile, then the microfabrication team attempts to create these traps by adapting common manufacturing processes. This is an iterative process and sometimes there are unexpected problems with the microfabrication techniques. With traditional room temperature systems, the rate at which data can be gathered and given back to the microfabrication team is slow due to the limitations in how quickly the system can be prepared for trap testing. With a cryogenic system we are able to rapidly test surface ion traps and give valuable data back to the microfabrication team who can make changes and fix any issues that arise.

In this chapter we will discuss the experimental results gained from three generations of surface ion traps. The first generation ion traps were created in 2014 and are manufactured with a gold on sapphire layered structure. The second generation ion traps are from an collaborative partner microfabriation department[24]. These traps are also manufactured with a gold on sapphire layered structure. The third generation of ion traps are manufactured by our own department and were created in 2017. These traps are manufactured with a gold on high resistivity silicon ($10\,\mathrm{k\Omega\,cm}$). These traps also feature a buried ground layer.

5.9.1 Chip Preparation

The first step before the microfabricated ion trap can be placed into the cryogenic system is to measure the capacitance and effective series resistance (ESR) of the trap, this is done to ensure that no pinholes have formed in the substrate lays causing short circuits and that the trap will be able to resonate with the cryogenic resonator at an acceptable frequency for trapping.

To do this we created a three pin surface probe which is connected to our vector net-

[24] National University of Defence Technology, Changsha, Hunan China

work analyser (VNA) while making physical contact with the traps surface RF electrodes allowing us to take measurements at the expected trapping RF drive frequency.

The first step is to calibrate the VNA with the probe to remove the electrical effects of the coax cable and the surface probe geometry. To calibrate the VNA we created a PCB with three electrical standards, an open circuit stub, a closed circuit short and a 50 Ω termination. By placing the probe onto each calibration section and performing a calibration run on the VNA we move the measurement plane to the tips of the surface probe pins. This ensures that all measured values represent the traps geometry and not the measurement setup.

Trap Cleaning

The next step is to clean the trap thoroughly from any dust and particulates that might have come into contact with the surface. It is also important to remove any residual organic compounds from the microfabrication process, such as the photoresist layer.

The first cleaning step is to submerge the trap in acetone and place in an ultrasonic bath for 10 minutes. This process dissolves dust and grease in a gentle manner without damaging the trap surface. Following the acetone bath, the same process is performed again with isopropyl alcohol (IPA). The IPA step is to wash off any acetone before it can evaporate redepositing organic compounds onto the surface.

The final cleaning process is to place the trap into a plasma asher[25] with a mixture of oxygen ($50\,\mathrm{cm^3\,min^{-1}}$) and argon ($200\,\mathrm{cm^3\,min^{-1}}$) for 10 minutes. This ashing process removes harder organic compounds such as any remnant photoresist.

The trap is now ready for diebonding with indium foil and wirebonding to the in vacuum PCB.

5.9.2 Generation 1 - Linear Sapphire 2014

The first generation microfabricated linear surface ion traps were constructed on a 600 µm thick sapphire wafer, then a layer of silicon dioxide followed by a titanium adhesion layer to bond with 5 µm of electroplated gold.

Figure 5.27 shows a stitched microscope image of a first generation 100 µm ion height

[25] Alpha Plasma Q235

Figure 5.27: First generation microfabricated linear ion trap. Designed for a 100 µm ion height. The RF electrodes are 144 µm wide with 5 µm gaps (trenches) between the electrodes. The central ground width is 86 µm and the DC electrodes have a width of 200 µm. This generation of traps had issues with the cleaving process where the wafer is snapped to separate the traps, this can be seen by the damage to the top right of the image.

linear surface trap. Stitching is a process where we can take multiple images of the trap using the microscope and attach them together to create a full composite image of the entire surface. Using the surface probe, previously described, we measured the capacitance and ESR for the trap. At an estimated RF driven trapping frequency of 20 MHz we measured a capacitance of 13.5(2) pF with an ESR of 0.58(1) Ω. When mounting the trap within the cryogenic system we measured an actual resonant frequency of 21.113(1) MHz.

Surface Layer Adhesion

When the first ion trap was brought to cryogenic temperatures it was clear from the EMCCD camera that a catastrophic failure had occurred to the surface of the trap. After removing the trap we imaged it under a microscope forming a stitched image than can be seen in Figure 5.28.

The top layer had become detached across the surface of the ion trap. Using a multimeter, to check for continuity, the regions where gold was missing showed no electrical connectivity. This, therefore, means that the titanium layer is either missing or it separated along with the gold layer. After enquiring with the microfabrication team it was discovered that hydrofluoric acid (HF) was used during the manufacturing process. HF is known to etch titanium at a rate of $>100\,\text{Å}\,\text{min}^{-1}$[130], therefore it is most likely that HF removed the titanium causing the adhesion fault. Following this discovery the adhesion layer was changed to chromium for future batches from this generation of ion traps.

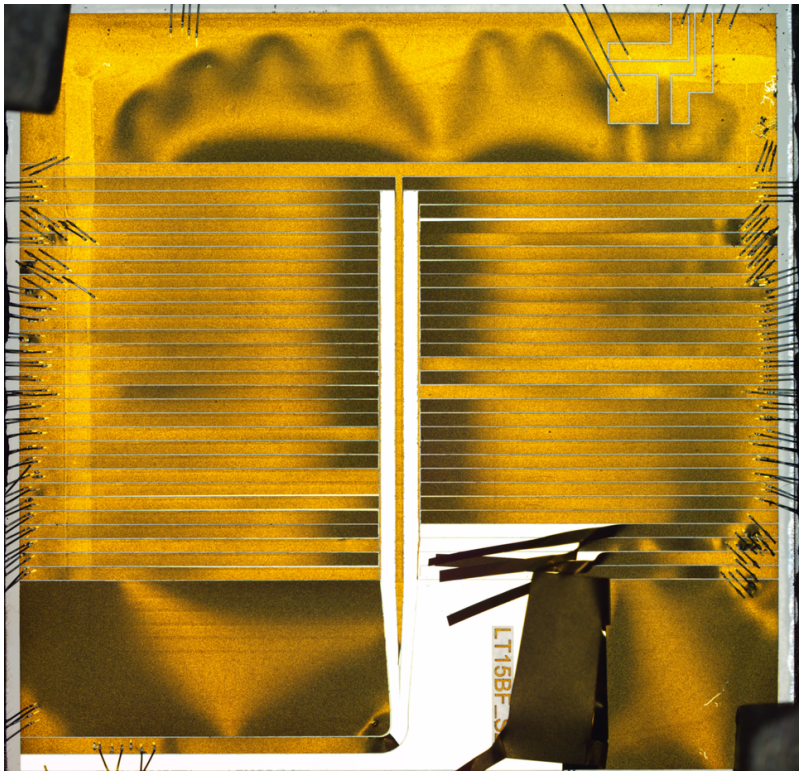

Figure 5.28: Linear surface ion trap after cryogenic cycle, that shows extreme surface damage. The cause was attributed to titanium removal by hydrofluoric acid during the microfabrication process.

Investigating Glow

After receiving a new batch of traps one was successfully mounted and cooled down to cryogenic temperatures. After a period of a few hours of applied RF power, bright regions appeared on the EMCCD camera which we will refer to as "glow" from now on.

When new traps have RF power first applied it has been previously observed that they "glow" in the gaps (trenches) between the RF electrodes and the ground plane. This is the region with the highest voltage potential difference. "Glow" is not to be confused

with electrical breakdown which happens at a much higher voltages and is rapidly catastrophic. "Glow" is usually assumed to be caused by dust or particulates that bridge the small micron sized trenches and permits electrons to jump across. This assumption comes from the fact that, in general experience with other ion trap systems, a more carefully cleaned trap exhibits less "glow". Normally after a few hours the "glow" starts to subside, as presumably the dust is vaporised away.

However, with our new batch of traps the "glow" increased in brightness over the time span of 4 to 10 hours. After which the trap would be rendered unusable due to the emitted light flux obscuring the trapping region. It was also observed that the glow would start appearing at decreasingly lower applied RF voltages over time. Figure 5.29 shows a stitched image along the RF-GND electrode boundary, this image was taken after 8 hours at 155 V peak RF.

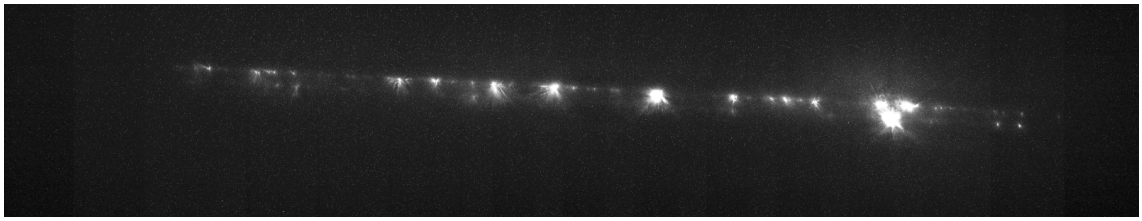

Figure 5.29: Stitched EMCCD camera image of "glow" between one RF electrode and the neighbouring central ground electrode.

We theorised that the "glow" could be caused by a low pressure plasma since the background pressure of the system is around 10^{-12} mbar. This plasma is formed in the trenches where the electric field strength is highest. Different cleaning regiments were tried in case this was leaving residue that could cause the plasma. None of the cleaning steps changed the pattern or severity of the "glow" observed.

The next step was to try and measure the frequency spectrum of the plasma to narrow down the list of possible contaminants. We tried to split the light spectra with a prism and diffraction grating but with so few photons emitted by the "glow" this was unsuccessful. We also didn't have available in the lab any spectrometers that could easily be hooked up to the system to measure the spectral lines.

We had available a narrow band UV filter (350 nm to 370 nm) normally used for 369.5 nm florescence imaging and an IR filter (<550 nm) normally used for laser overlapping. So a method was created where we could measure the number of photons emitted in three spectral bands.

The reasoning behind this approach was to see if we could see a shift in the dominant emission spectrum of the "glow" over time and by running this experiment on multiple traps at different stages of decay we might observe some physical change under the microscope that correlates with the observed glow and its spectra.

First, the RF voltage was set and the trap allowed to thermally stabilise. Then each of the two filters were placed in line with the imaging optics and the EMCCD camera was used to take an image. Then a background image, with no filter, was taken. The two filtered images were then subtracted from the unfiltered image to give a third image formed from difference of the two filtered images and the unfiltered one. Since the EMCCD camera is insensitive beyond UV wavelengths (<350 nm) we can treat this new third image as representing the photons emitted in the middle wavelength range (370 nm to 550 nm). Figure 5.31 shows the unfiltered image at the top and the two filtered images, on the left and right edge, along with the difference image down the center, for different applied RF voltages.

It was also observed, that over time the "glow" emissions would change in wavelength. When "glow" is first observed it requires a high applied RF voltage (≈ 180 V) and it would be dominant in the UV spectrum with little to no IR light. Over the span of a 2 to 4 hours the IR spectrum would become dominant.

Figure 5.31 shows a different trap from the same batch that has larger trenches (30 µm), this trap was used because the breakdown voltage is higher due to the trench size being wider between the RF and ground electrode. Using this trap allows for a larger RF voltage sweep when testing the "glow" spectra.

Once the trap was removed from the cryogenic system, the positions where glow was observed were imaged under the microscope. Figure 5.32 shows three regions where glow was observed, with different focus planes. The top row of three images are focused onto the surface of the gold surface. The second row of images are focused at the midway height between the bottom of the trench and the surface (2.5 µm depth from surface). The bottom row of images are focus at the bottom of the trench. As can be seen the gold from the surface layer has been ejected into the trench.

We can use a computer program called ImageJ[131] which is included as part of the Fiji software package[132] to examine the surface profile of the ejected gold. ImageJ is a microscope image manipulation suite normally used by bio-medical researches. One of modules[133] contained in the Fiji software suite can be used to analyse multiple focal

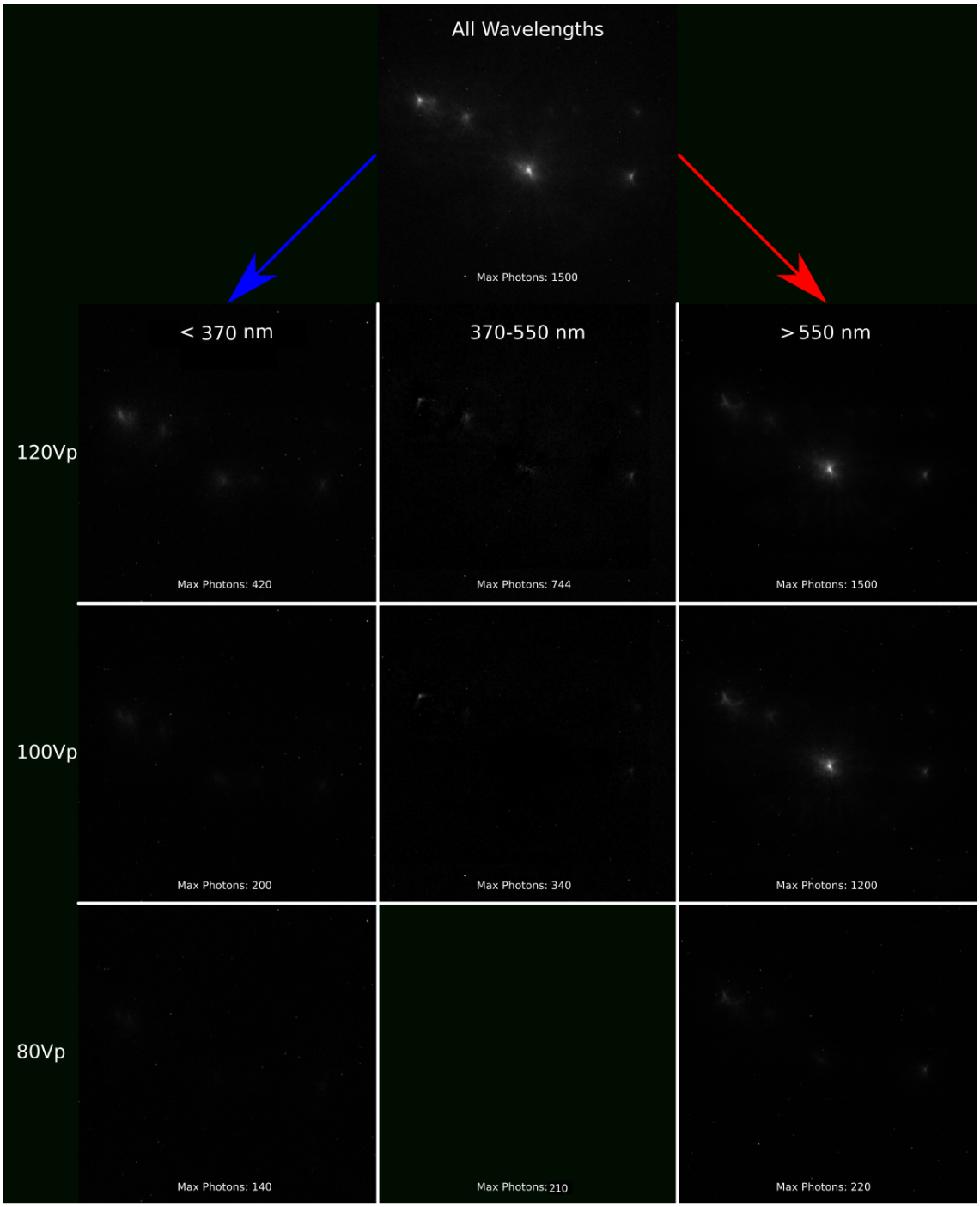

Figure 5.30: Spectral decomposition of trap "glow" over three different applied RF voltages. Regions of brightest "glow" tend to exhibit in the longer wavelengths (<550 nm). Images taken on a new trap at the first appearance of "glow". Image exposure is 0.5 s.

plane image stacks where images are taken at different focal planes to build up a 3d image.

Figure 5.33 shows the 3D representation of Figure 5.32 (b). It is built out of 5 images each focused at intervals of 1 µm. While this method of building a surface profile is not as accurate as other methods such as atomic force microscopy (AFM) it does give us a

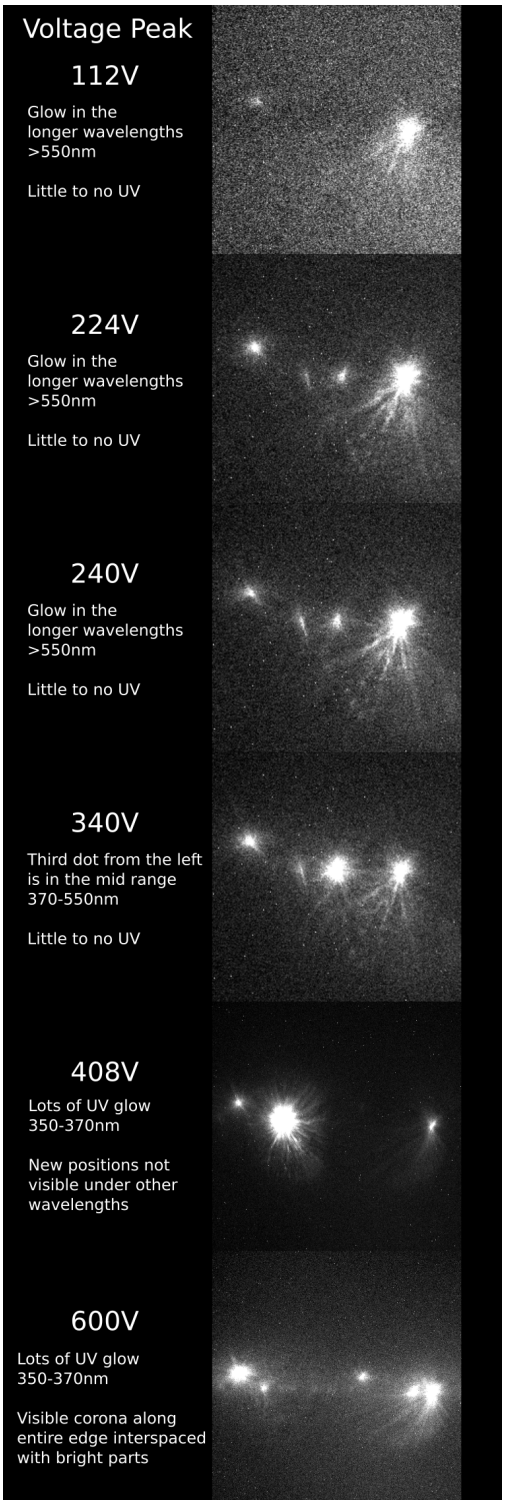

Figure 5.31: Image sequence of a wide trench (30 µm) ion trap design, showing the "glow" positions over an RF voltage range from 112 V to 600 V.

guide as to how much gold is ejected. Due to the surface appearing relatively undamaged compared to the volume of gold seen in the trenches, it was theorised that the gold had been ejected from the underside of the electrode surface. It was therefore decided to test

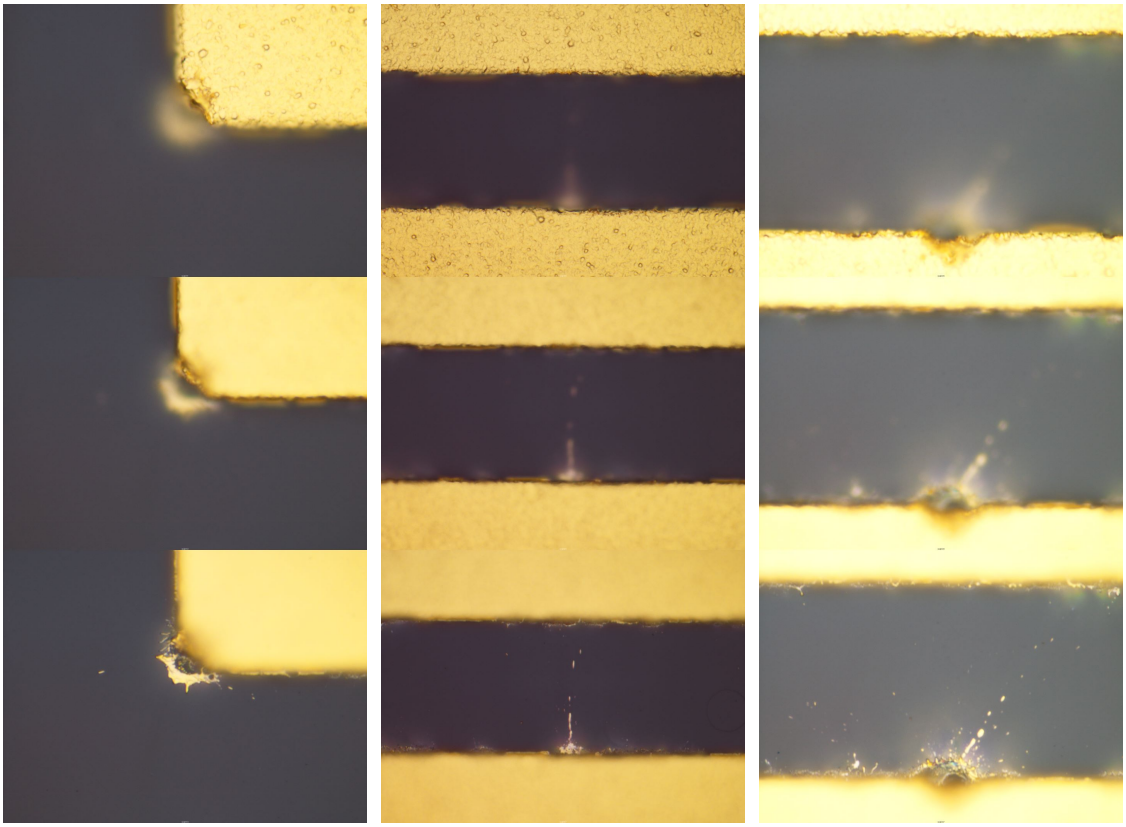

(a) (b) (c)

Figure 5.32: Composite images from three different locations where "glow" was observed. The top row of images are focused onto the gold surface of the electrodes. The second row is focused half way between the surface and the bottom of the trench. The bottom row is focused on the trench floor.(a) is centred on the corner of a DC electrode, (b) is along the edge of an RF electrode, (c) is from the middle of a DC electrode edge.

the chromium layer as this layer might have some part in the "glow" generation mechanism, where the gold was being dragged along during ejection of the chromium.

It was decided to create a sample of traps with no electroplated gold layer, leaving just the chromium seed layer. After glow was observed on one of these traps it was imaged under the microscope and we noticed deep undercutting Lichtenberg [134] style damage marks. Some of these patterns extended within the chromium layer. Figure 5.34 shows the damage of the chromium layer after glow was observed. It is visible where the damage breaches the surface (appears black on the image) and where the Lichtenberg style meandering has propagated a few microns under the surface.

Combined with the progressing damage observed and the chromium damage pattern it was likely that the chromium microfabrication process was the primary mechanism of the

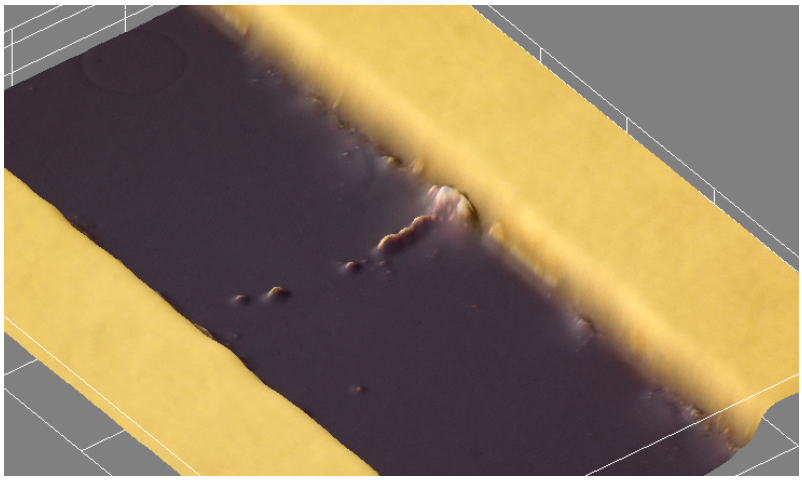

Figure 5.33: ImageJ 3D image from 5 stacked microscope images displaced by 1 µm increments. Ejected gold volume with little observable surface damage suggest gold is ejected from the bottom of the gold layer at the gold-chromium boundary.

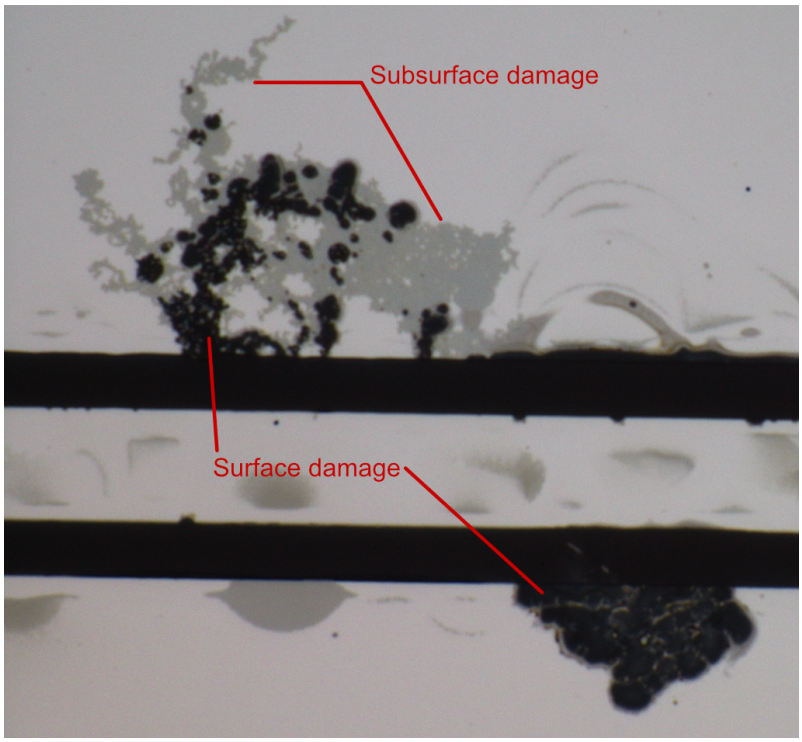

Figure 5.34: Image of a surface ion trap without the top electroplated gold layer. Visible is the chromium damage after observing glow. Also shown are Lichtenberg style damage marks under the surface of the chrome layer.

"glow" process. A fellow PhD student Weikang Fan who works on the microfabrication team used this data and proposed that Cl^+ ions from the dry etching process might be bonding to the chromium. These Cl^+ ions are then dislocated when high voltages are applied causing a Cl^+ plasma. Further details of the chemistry of this process are available

in his thesis which is in pre-publication.

After changing our microfabrication process to remove the dry etching step and use a wet etching process instead we observed no further glow with later batches of traps.

5.9.3 Generation 2 - Linear Sapphire 2017

The second generation of microfabricated linear surface ion traps were manufactured by the National University of Defence Technology in China[26]. These traps are manufactured on 850 µm of sapphire with 5 µm of gold for the surface layer.

Figure 5.35 shows the layout of the ion trap. It is designed for a 150 µm ion height. It consists of two RF electrodes 147 µm wide with 10 µm trenches between the electrodes. A central grounded electrode (GND) 180 µm wide and 15 DC electrodes on each side that are 145 µm wide.

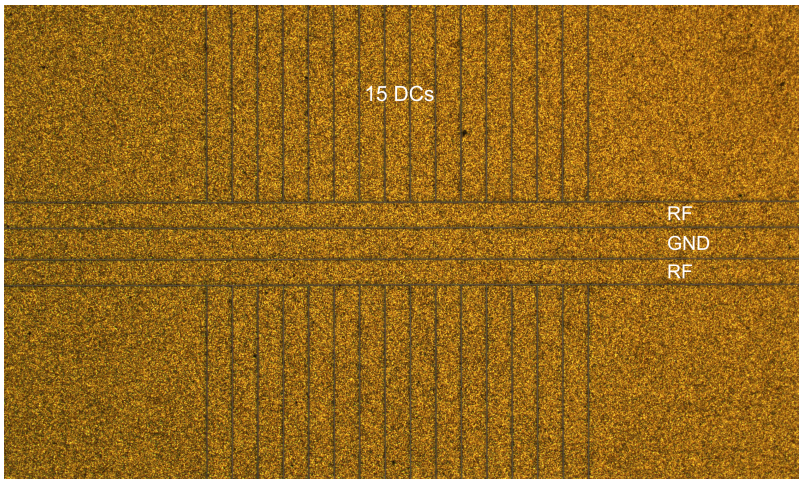

Figure 5.35: Second generation microfabricated linear ion trap. Designed for a 150 µm ion height. The RF electrodes are 147 µm wide with 10 µm trenches. The central ground (GND) width is 180 µm and the DC electrodes have a width of 145 µm.

This trap was tested with an AFM at manufacture and over a square surface of 20 μm^2. 65536 samples were taken yielding a maximum displacement of 409(1) nm and an average of 188(1) nm. The average roughness was 62.5(1) nm to one standard deviation.

We measured the trap parameters with the surface probe at an estimated 20 MHz RF drive frequency. The measured capacitance was 18.2(2) pF with an ESR of 0.40(1) Ω. When mounting the trap within the cryogenic system we measured an actual resonant frequency of 18.120(1) MHz.

Under RF power this trap did not exhibit any "glow".

[26] National University of Defence Technology, Changsha, Hunan China

At 4 K the cryogenic resonator had a measured maximum Q of 175 with an impedance, towards the generator, of $(48.51(2) + 0.23(2)\mathrm{j})\,\Omega$.

Trapping parameters

The trap was simulated in our ScuffEM toolkit that was described in Chapter 3. The initial trapping parameters for a four DC electrode configuration is given in table 5.5. The axial secular frequency for this trap was 166.5(1) kHz, the two other axial frequencies were 1.023(1) MHz and 1.224(1) MHz.

	Simulated	Measured after micromotion compensation
Ion Height	157 µm	156(2) µm
RF Voltage (for 0.5 eV trap depth)	213 V	207(5) V
DC1,4 (for 0.1 eV trap depth)	5.83 V	5.76(1) V
DC2,3 (for 0.1 eV trap depth)	−4.26 V	−4.34(1) V

Table 5.5: Table of trapping parameters for the second generation ion trap.

On the 31^{st} of October 2017 the cryogenic system trapped its first $^{174}Yb^{+}$ ion, this ion is shown in Figure 5.36.

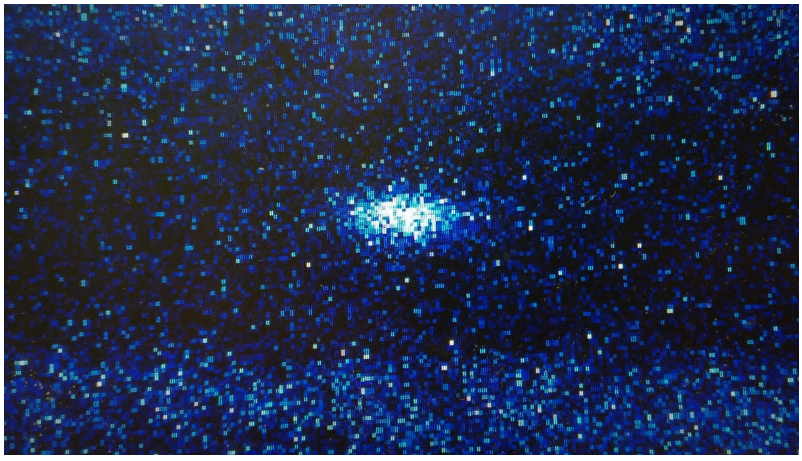

Figure 5.36: First ion trapped on the cryogenic system. Lifetime of ion was 4 hours 32 minutes. This image was taken shortly after the ion appeared for the first time, this is before any optical adjustments or micromotion compensation.

The first ion had a lifetime of 4 hours 32 minutes using the simulated parameters in Table 5.5. After multiple trapping runs and optimising the beam paths, laser powers, DC voltages and wavelengths the average lifetime was greater than 15 hours. The optimised DC parameters are also shown in Table 5.5.

The cryogenic oven also showed fast loading times averaging to 9 seconds from turning the oven on till the first ion appeared on the EMCCD camera.

Ion chains were also trapped, a 6 ion chain is shown in Figure 5.37 which had a lifetime of 1 hour 32 minutes, this was the time until one of the ions went into a dark state.

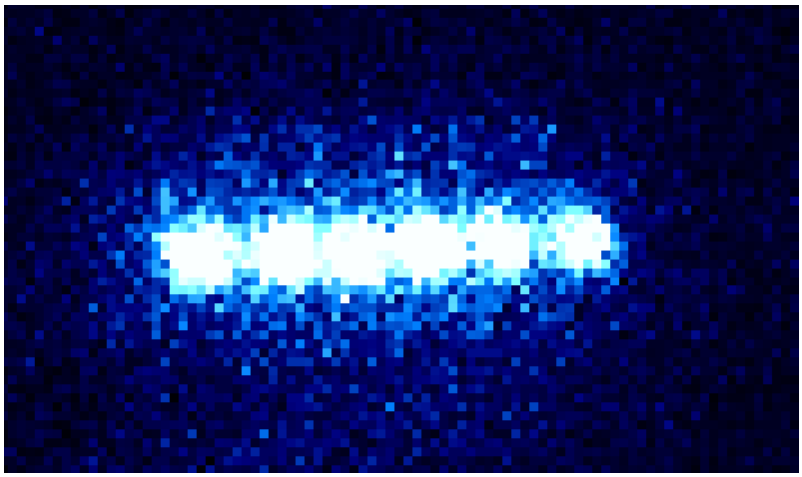

Figure 5.37: Image of 6 ions with a lifetime of 1 hour 32 minutes.

Heating rate

Using the Doppler re-cool method described in Chapter 2 we then measured the heating rate of the ion trap.

Measurements were taken for laser-off intervals of 10,15,20 and 30 seconds. Photon counts were collected from the PMT in 500 µs bins from 0 to 2 ms. Figure 5.38 shows the combined collected samples for 250 runs with 15 second laser-off intervals.

By combining each set of measurements for each of different laser-off periods we can plot a gradient which will represent the heating rate of the ion. Figure 5.39 shows the combined data of the 10, 15, 20 and 30 second laser-off measurements. Each data point in the graph contains the results from 250 heating rate measurements.

We calculated a gradient of 105(7) quanta/s for an axial secular frequency of 137(1) kHz. The radial secular frequencies were 1.378(1) MHz and 1.466(1) MHz at a RF drive voltage of 187(5) V.

By assuming that the heating rate $\dot{n}$ dependency on the electric field noise scales as $1/\omega^2$, we can can calculate the the electric field noise at 1 MHz(S_E(1MHz)). We calculate a S_E(1MHz) of $5.94(40) \times 10^{-14}\,\mathrm{V^2\,m^{-2}\,Hz^{-1}}$

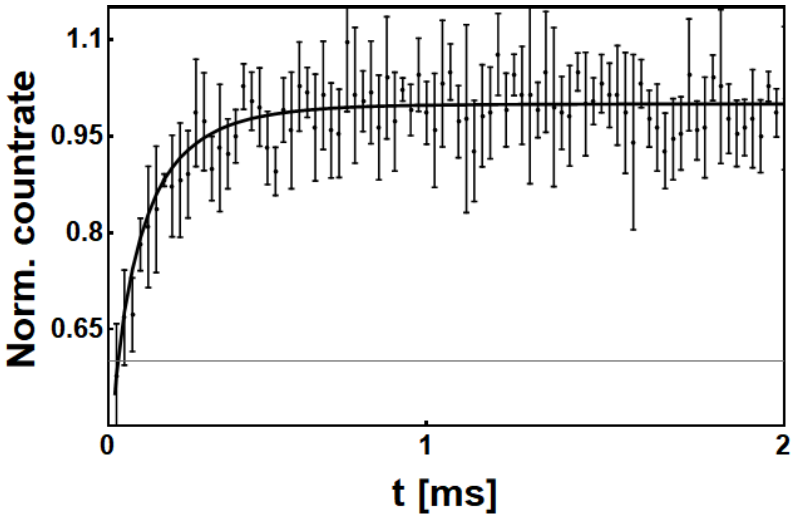

Figure 5.38: Generation two ion trap normalised count rate ($\dot{n}$) binned photon counts for 250 runs with a laser-off interval of 15 seconds. Each dot represents the value of a bin with appropriate error bars, time period between bins is 500 µs.

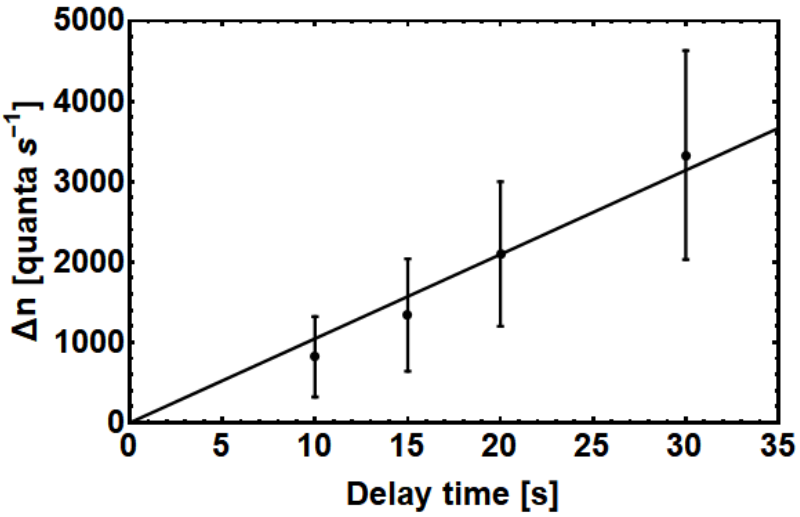

Figure 5.39: Generation two ion trap heating rate ($\dot{n}$) data from four sets of measurements at 10,15,20 and 30 second laser-off intervals. The gradient gives the heating rate of the ion as 105(7) quanta/s for an axial secular frequency of 137(1) kHz.

Trap ion transport

To test our 80 channel DAC card interface we used our shuttling program as described in Chapter 3 to generate a voltage ramp profile. This profile was set to slowly move (10 Hz) the ion a distance of 1885 µm or the equivalent of 13 DC electrode widths. The purpose of the test was to check that both the ramp generator, PC to DAC interface and cryogenic wiring to the trap were all working correctly. Figure 5.40 shows a three frame capture of

the ions motion through the 369.5 nm laser light. The ion is not visible at the extremes of the shuttling motion.

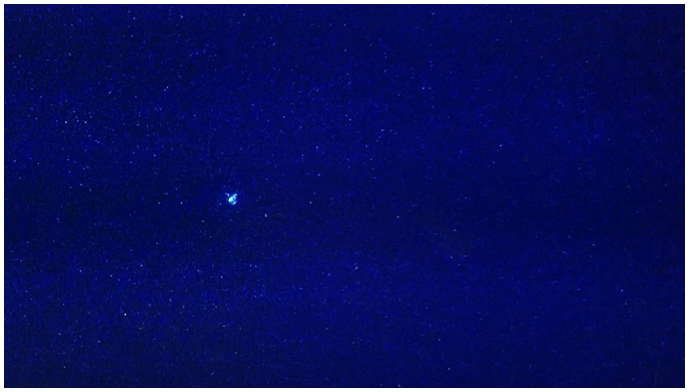

(a)

(b)

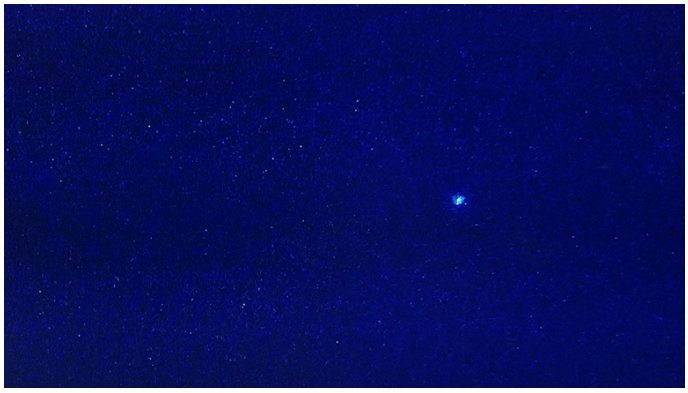

(c)

Figure 5.40: Images from the DAC interface test. From (a) to (c) the ion is shown as it passes through the 369.5 nm laser light (≈ 100 µm visible path). The total distance shuttled is 1855 µm or 13 DC electrode widths.

The DC test was left to run for 6 hours, this is an equivalent distance travelled of 407.16 m with no loss of an ion. The laser beams were left on during this process but they did not track with the ion.

5.9.4 Generation 3 - Linear Silicon 2018

It has been shown before[135] with intrinsic silicon microfabricated ion traps that when the silicon is cooled down to cryogenic temperatures it exhibits good electrical insulation properties and low RF power losses due to the freezing out of charge carriers in the silicon. For our room temperature systems, however, the silicon charge carriers would not be frozen out and so it was decided by the microfabrication team to experiment with high resistivity silicon.

These third generation of microfabricated linear surface ion traps were manufactured with the following layers: 650 µm high resistivity silicon (10 kΩ cm); 1 µm of gold (Buried ground layer); alternating layers of silicon dioxide (0.2 µm thick) and silicon nitride (1.8 µm thick) forming a total stack height of 8 µm; 5 µm gold (Surface layer).

Figure 5.41 shows the layout of the ion trap. It is designed for a 100 µm ion height. It consists of two RF electrodes which are connected through a single meander electrode to the edge of the chip. Each RF section is 144 µm wide with 5 µm trenches between the electrodes. A central ground electrode 86 µm wide and 8 DC electrodes on each side that are 200 µm wide.

I measured the trap parameters with the surface probe at an estimated 20 MHz RF drive frequency. The measured capacitance was 14.9(2) pF with an ESR of 21(1) Ω. When mounting the trap within the cryogenic system we measured an actual resonant frequency of 14.929(1) MHz. Under RF power this trap did not exhibit any "glow".

Due to the very large ESR measured the traps power losses are much higher than that measured on the second generation sapphire trap. This has a detrimental effect on the resonator Q and the required drive power must be increased to compensate.

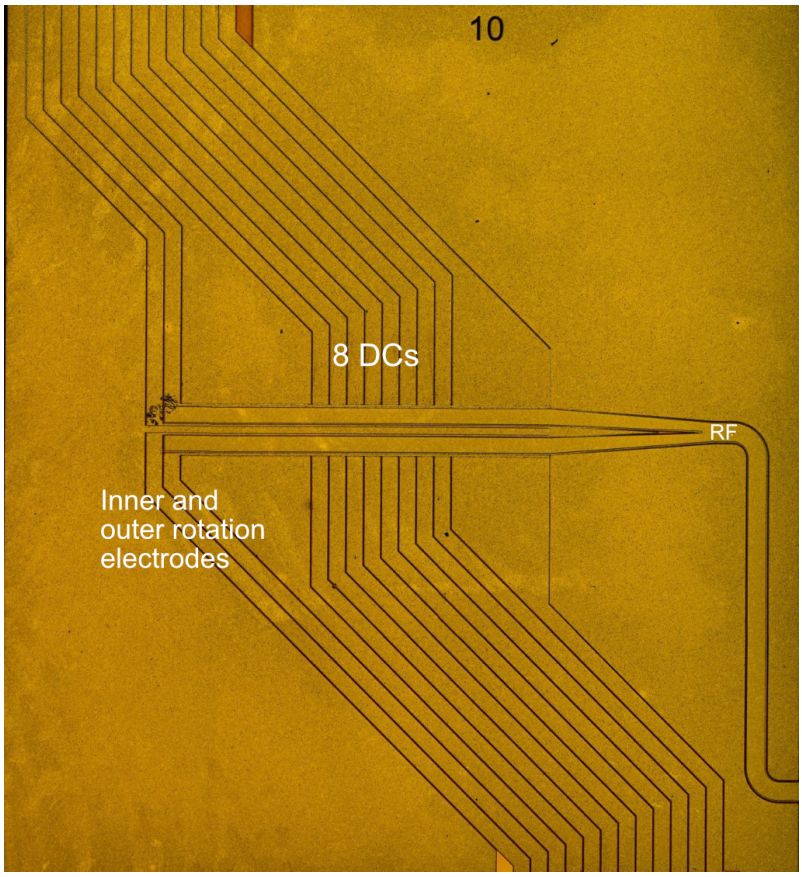

Figure 5.41: Third generation microfabricated linear ion trap. Designed for a 100 µm ion height. The split RF electrodes are 144 µm wide with 5 µm trenches. The central ground width is 86 µm wide and the DC electrodes have a width of 200 µm.

Cryogenic resonance and Q

I decided to record the resonator Q value while cooling down the cryogenic system. If the high resistivity silicon exhibits the same charge carrier freeze out as intrinsic silicon we would expect to see an increase in Q around 50 K to 60 K.

Figure 5.42 shows the resonator Q while cooling the trap down to cryogenic temperatures. Data was collected with the VNA every 5 seconds automatically using a Python script.

Due to the high trap dielectric losses the starting resonator Q at room temperature is only 37.9. As the temperature drops there is a rise in the Q which would be expected. At around 81 K the Q reaches a maximum of 49.4. At around 60 K the Q gradient inverts and the Q lowers rapidly to a minimum of 42.5 at 32.7 K.

At around 18 K to 14 K the superconducting wire of the resonator starts superconducting. This is most likly the reason that there is a slight Q rise below 18 K.

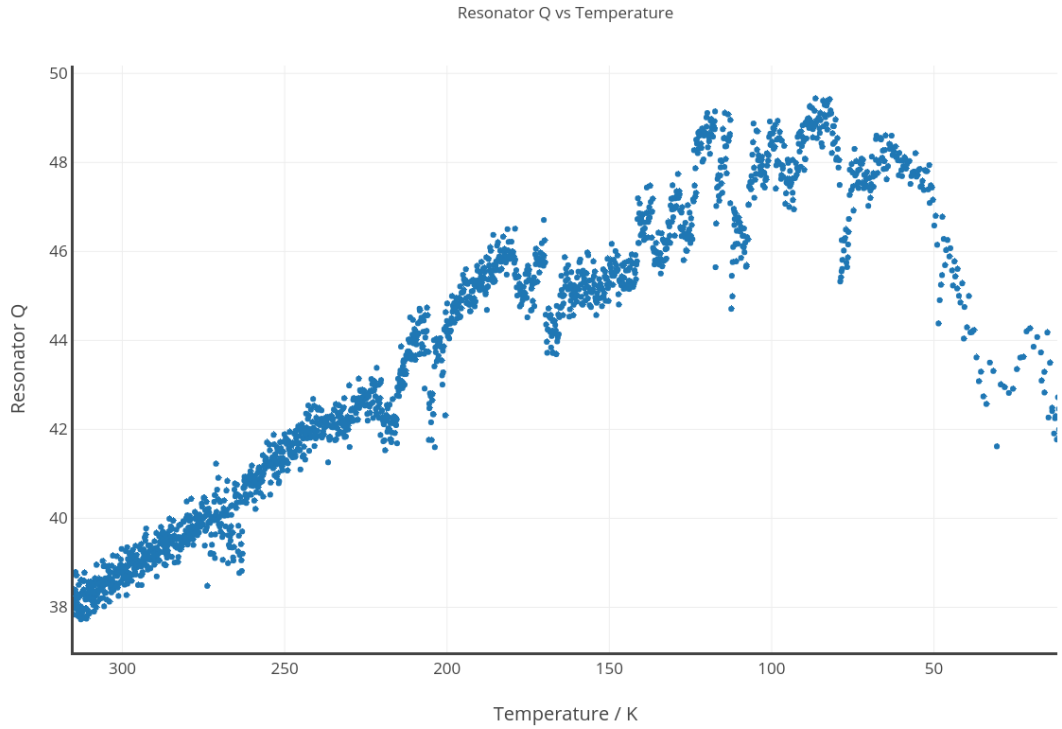

Figure 5.42: Graph of resonator Q vs temperature of the high resistivity silicon micro-fabricated ion trap. At 315 K the Q is 37.9 which rises to a maximum of 49.4 at 81 K. There is then a Q inversion around 60 K. At around 18 K to 14 K the cryogenic wire of the resonator starts superconducting causing the Q to rise.

At 315 K the Q is 37.9 which rises to a maximum of 49.4 at 81 K. There is then a Q inversion around 60 K.

The impedance at 4K is measured as $(47.88(2) + 0.11(2)\mathrm{j})\,\Omega$. Therefore we can attribute the low Q to the losses in the trap dielectric and not to impedance miss-match. This meant that the silicon substrate was not becoming a better isolator when going cryogenic.

Trapping parameters

The trap was also simulated in our ScuffEM toolkit. The initial trapping parameters for a four DC electrode configuration is given in table 5.6.

Figure 5.43 shows the first trapped ion on the high resistivity silicon ion trap. This was the first time that we have, on the same system, trapped on two different ion traps in less than one week. This is an important step in demonstrating the fast turnaround time of the cryogenic system. The axial secular frequency for this trap was 334.2(1) kHz, the two other axial frequencies were 1.423(1) MHz and 1.824(1) MHz.

Initial trapping lifetime was 2 hours 23 minutes. After micromotion compensation the

	Simulated	Measured after micromotion compensation
Ion Height	96 µm	98(2) µm
RF Voltage (for 0.5 eV trap depth)	112 V	109(5) V
DC1,4 (for 0.1 eV trap depth)	2.18 V	2.54(1) V
DC2,3 (for 0.1 eV trap depth)	−1.98 V	−1.34(1) V

Table 5.6: Table of trapping parameters for the second generation ion trap.

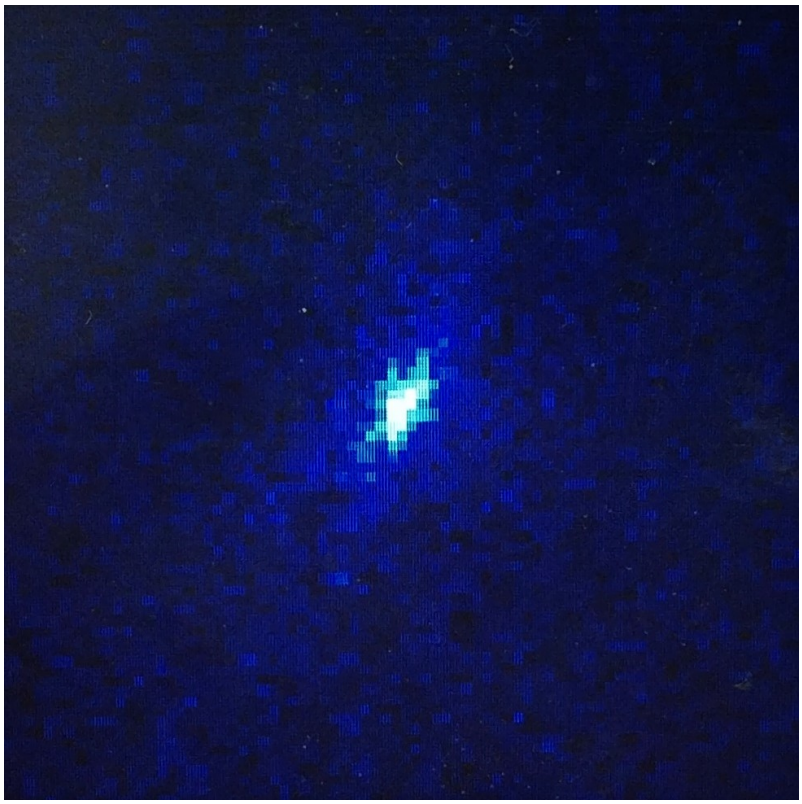

Figure 5.43: First cryogenically trapped ion on the high resistivity silicon substrate surface ion trap.

average lifetime for a single ion was over 6 hours.

Heating rate

Heating rate method used was identical to the generation two ion traps.

Figure 5.44 shows the combined collected samples for 250 runs with 15 second laser-off intervals.

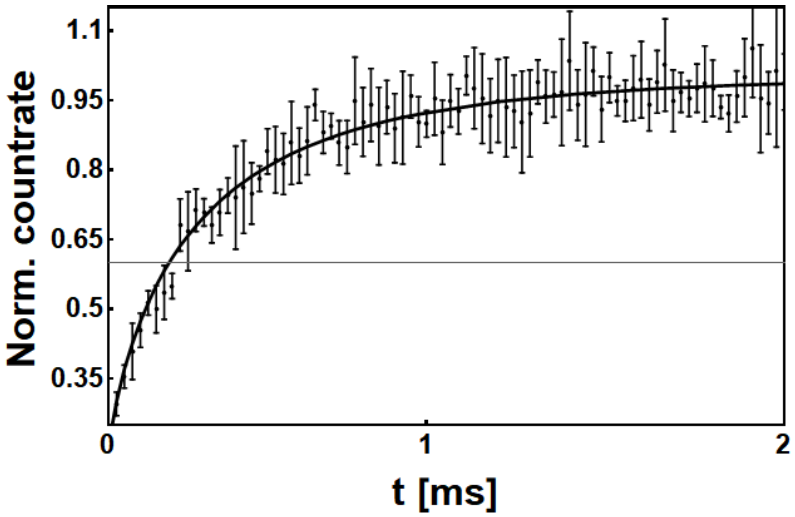

Figure 5.44: Generation three normalised count rate ($\dot{n}$). Binned photon counts for 250 runs with a laser-off interval of 15 seconds. Each dot represents the value of a bin with appropriate error bars, time period between bins is 500 µs

Figure 5.45 shows the combined data of the 10, 15, 20 and 30 second laser-off measurements. Each data point in the graph contains the results from 250 heating rate measurements.

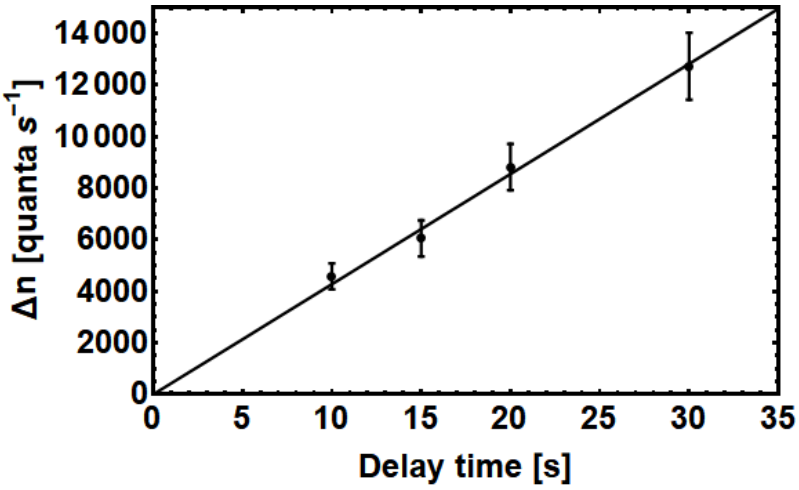

Figure 5.45: Generation three recooling florescence ($\dot{n}$) data from four sets of measurements at 10, 15, 20 and 30 second laser-off intervals. The gradient gives the heating rate of the ion as 423(7) quanta/s for an axial secular frequency of 138.8(10) kHz.

We calculated a gradient of 423(7) quanta/s for an axial secular frequency of 138.8(10) kHz. The radial secular frequencies were 1.052(1) MHz and 1.131(1) MHz at a RF drive voltage of 87(5) V.

Using the same assumption as that for the generation two trap we can calculate the electric field noise at 1 MHz(S_E(1MHz)) to be $2.39(40) \times 10^{-13}\,\mathrm{V^2\,m^{-2}\,Hz^{-1}}$

5.9.5 Comparing heating rates

We can compare the heating rates to each other and to known published results.

It has been predicted[136] that the heating rate scales with ion-surface separation approximately as $\dot{n} \propto d^{-4}$. We can compare the two traps and work out the power scaling factor.

Generation two had a heating rate of 105(7) quanta/s at an ion height of 156(2) µm. Generation three had a heating rate of 423(7) quanta/s at an ion height of 98(2) µm. This gives us a heating rate scaling power factor of -2.99(6). This is less steep than the patch potential model would predict. The discrepancy may be caused by other differences between the two traps such as surface roughness, different trap geometry and manufacturing processes.

We can also compare our heating rate measurements to other published results. Figure 5.46 is adapted from Chiaverini *et al.* [12] who compared both cryogenic and room temperature systems. It can be seen that the two heating rates for our traps, designated by blue crosses, fall within the range of data by other groups and also within the range of traps that were cryogenic, designated by open symbols.

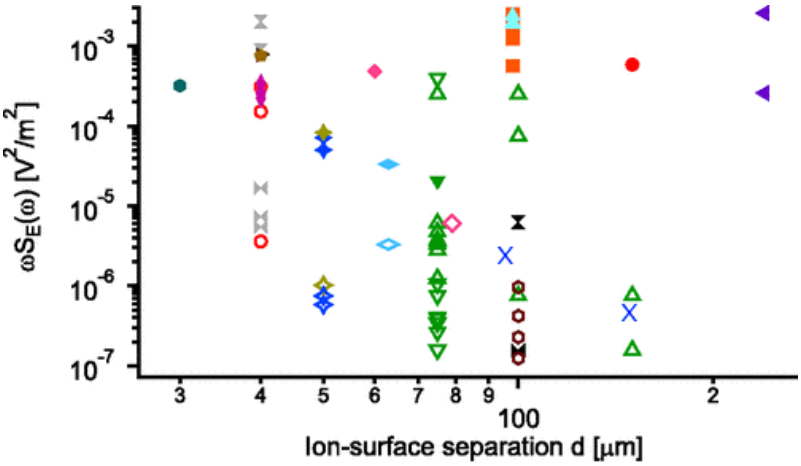

Figure 5.46: Graph showing published noise spectral density results from both cryogenic and room temperature systems. Open symbols (holes) are cryogenic systems. Closed symbols (filled) are room temperature. Bowties are systems with in situ surface milling equipment. Our two data points are represented as blue crosses. Adapted from Chiaverini *et al.* [12]

5.9.6 Preparation for a complex junction

Till now all the traps used in the cryogenic system required fewer than 30 DC connections. This allowed us to create simple PCBs on our in house miller and each connection was plugged in by hand.

As we move towards complex geometries, it is therefore necessary to design the required high density PCB for upto 100 connections and the required DC connector to allow for a large number of connections in a limited space within the inner radiation shield.

Previous systems in our group[53] made use of a two part PCB structure. The front PCB was attached to the removable trap mount, while the back PCB was mounted from behind and contained spring-loaded gold pogo pins, named such as they contain a spring, like a pogo stick to apply positive pressure to the mating surface. When the two PCBs are screwed together the pogo pins make contact between the back PCB, which contains a single stage RC filter and is permanently soldered to the DC wires and the front PCB which can be removed from the system. The back PCB in this setup, however, is 30 mm larger than our inner radiation shield and it would also impact our resonator coil.

So it was decided to create a special custom DSUB connector each with 50 connections and built in filtering.

Figure 5.47 shows the design for the 50 connection DSUB with built in filtering. It consists of three parts, the PCB section is soldered to the main PCB that eventually gets

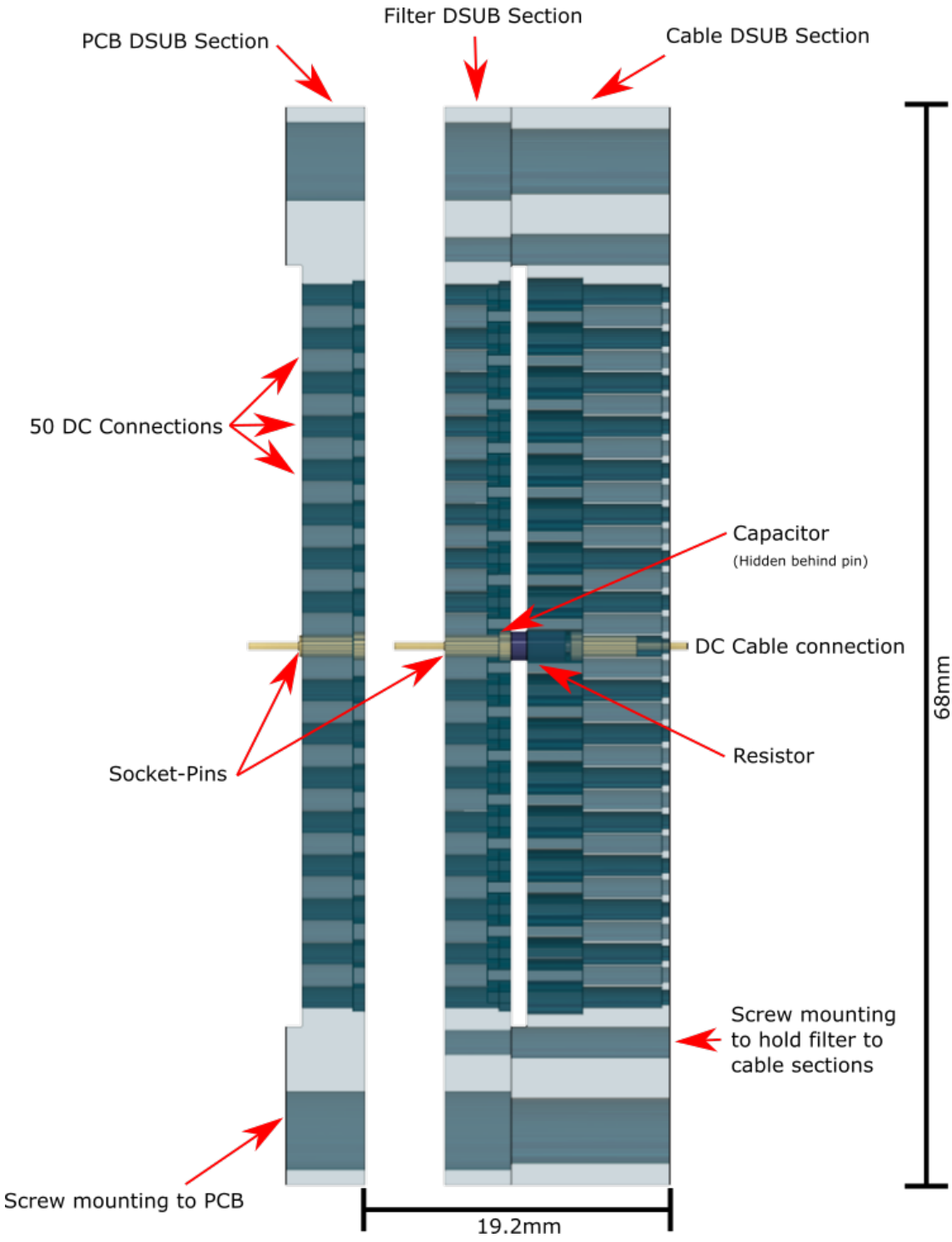

Figure 5.47: Custom DSUB with built in filtering. The PCB section is soldered to the main PCB, that is wirebonded to the trap. The filter and cable sections normally remain within the vacuum system. The DSUB contains 50 connections and measures 69 mm long, 19.2 mm deep, when closed, and 9 mm wide.

wirebonded to the trap. The PCB section is easily removable from the system by removing the two screws on either end. In the figure the DSUB is in an unplugged position.

The middle section of the DSUB is the filter section, which houses the 1 kΩ resistor and the 620 pF ceramic capacitor for each channel. This RC filter is in a low pass topology and has a cutoff frequency of 257 kHz, this cutoff was chosen such that it was lower than the RF drive frequency but high enough to allow faster shuttling regimes to be tried at a later date by only needing an external filter change. The middle sections usually remains within the vacuum system but it can be detached by removing two screws on either end, this allows for easy filter alterations.

The final section of the DSUB is the cable section, which houses the DC cable solider point and strain relief. This section is never removed from the vacuum system under normal operation.

X-Junction

The next trap to be tested within the cryogenic system is an x-junction like the sample shown in Figure 5.48. This trap has 60 DC connections plus 4 RF connections. Since the high resistivity silicon showed such a high ESR with generation three, the microfabrication team are currently working on a different main substrate and ground plane structure to reduce the ESR and lower the chip losses. The surface wirebond positions at the edges of the trap are fixed irrespective of the trap layout or electrode geometry, so designing the in vacuum PCB was completed in preparation for their arrival.

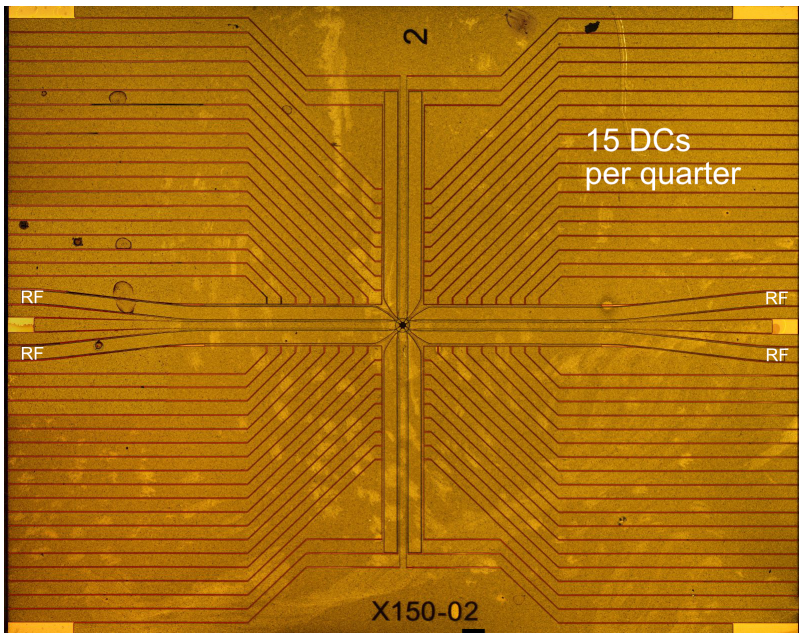

Figure 5.48: Sample x-junction from generation three. This x-junction design has 60 DC connections split into four corner groups. It also features four RF inputs on the left and right side.

Figure 5.49 shows the designed PCB for the x-junction trap with overlaid trap geometry. Since the x-junction contains 4 RF connections on two edges of the trap the PCB is required to feed both RF signals in phase. This was accomplished by routing the RF on the bottom side of the PCB in two equal length traces which merge into a single SMP connector. This single feed-in ensures the RF remains in phase on both halves of the trap. All non-used DC connections are grounded to the PCB ground plane.

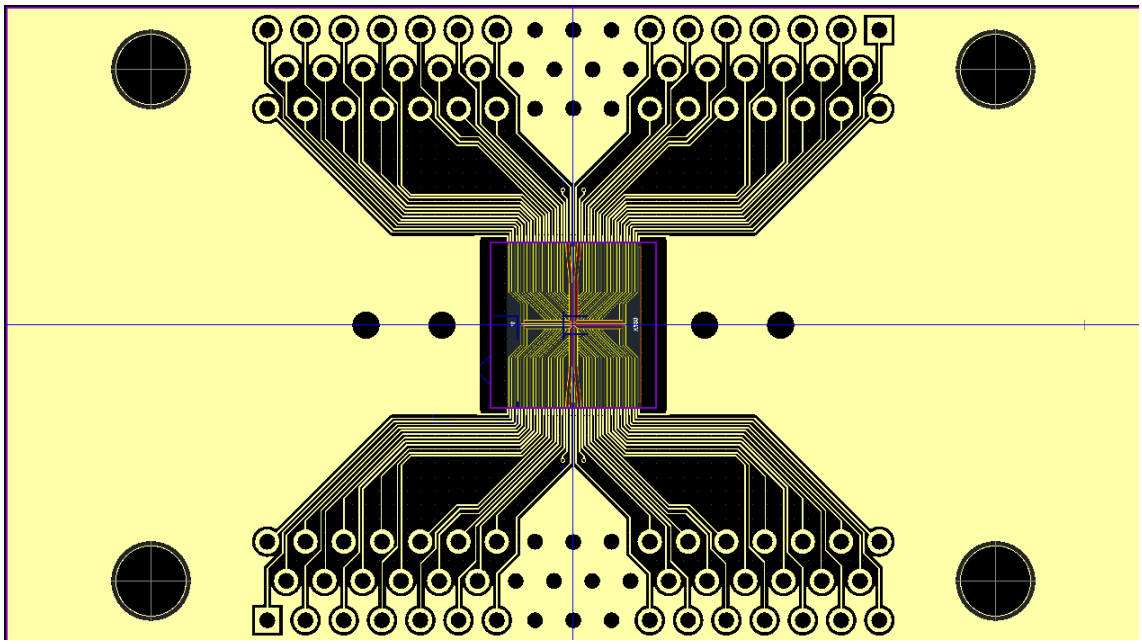

(a)

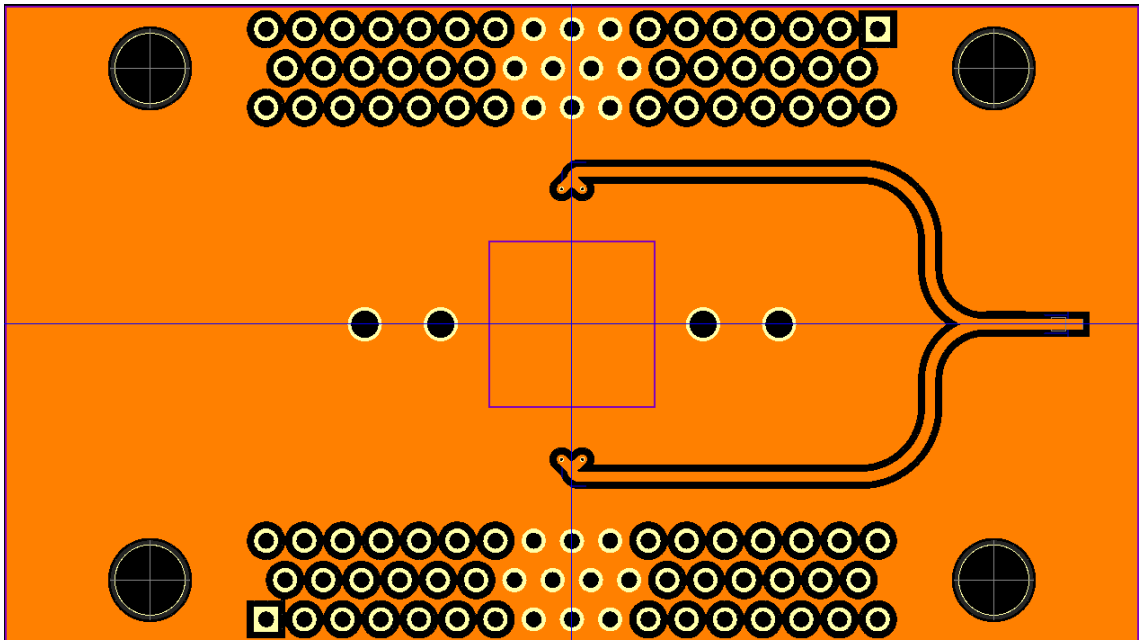

(b)

Figure 5.49: X-Junction PCB design with overlaid trap geometry. (a) shows the top layer with DC terminations from two DSUBs and vias for RF pass through from the bottom layer. (b) shows the bottom layer with dual RF traces terminating in a single SMP connector. SMP connection can be seen in b) on the far right where the RF line ends in a microstrip stub

5.9.7 Conclusion

In this chapter I have described the process by which we clean and prepare the surface ion traps for being tested in the cryogenic system.

I then described three generations of ion trap that have been tested in the system. I gave my findings about the surface adhesion problems that arose from the use of HF on the titanium adhesion layer and this information was used to alter manufacturing techniques by others.

I also described the effects of "glow" that were prominent in the first generation of chips. I discussed the testing procedure developed for measuring the light power spectra and showed the damage that resulted from "glow". Using a systematic approach the cause was narrowed down to being caused by the chromium layer. This information was then given over to the microfabrication team and changes were made which resulted in no further glow on later generations.

I describe the first ion trapped in the system with a generation two chip. I also give the trapping parameters used and the lifetimes of the ion for both the generation two and three traps. I performed heating rate measurments on both generation two and three traps and the results were presented, these were then compared to other published results from similar ion traps.

I also discussed the high ESR value that was discovered with the high resistivity silicon chips (generation three). While the resonator Q was high enough to allow trapping on these traps it does reduce the efficiency of the trap as power is dissipated in the substrate.

I then went on to show the future plans for the cryogenic system and the preparation for testing a complex geometry trap such as the x-junction. This trap requires a higher number of DC connections so a new connector was created that will fit within the vacuum system while also allowing for single stage filtering. I also presented the new PCB design for the high density connections needed to connect the system to the trap.

Chapter 6

Conclusion

In this thesis I set out to create a cryogenic vacuum system for trapping ytterbium ions in surface microfabricated ion traps.

The purpose was to allow us to test and refine the manufacturing techniques and trap reliability to help us create a fully scalable quantum computer.

I started by giving a brief overview of ion trapping and the theory behind Paul traps which form the basis of the trap technology we employ.

Due to the nature of this system being used to test ion traps rather than the more traditional approach of pairing one trap with one system for months, we needed to create a cryogenic system and ancillary equipment was would be generic enough to allow it to be invariant to the trap within the system.

This also drove the need to develop a novel cryogenic auto-transformer resonator that would not only fit within the confines of the cold head but also resonate with a wide variety of traps without needed modifications.

Combined with the software development based on the ScuffEM software toolkit and a custom DAC controller I was able to show the system trapping for the first time.

We shortly encountered issues with our ion traps in the form of "glow", I then showed how this new cryogenic system could be used to find a possible source of the problem. After feeding this back to the microfabrication team we made recipe changes to the microfabrication process and the issue of "glow" was resolved. This issue alone would have set back the other experiments in the lab due to their long baking process.

I then went on to describe the later trap generations and the heating rate measurements I performed on them.

6.1 Future work

The work culminating in this thesis was primarily focus on the engineering challenges in building a cryogenic ion trapping system. The system worked for the intended purpose of analysing ion traps and taking data. However the system is equipped with the apparatus needed to trap Yb^+ 171, including a novel microwave patch antenna and high gradient magnetic field coils.

Going forward it would be good to trap on a complex junction ion trap, such as an X-junction and use the full channel space of the DAC controller. This would allow us to characterise the RF and DC potentials at the discontinuity of the junction.

Quantum gates could also be formed in the system on chains of ions and quantum logic operations could be undertaken. It would be interesting to see how much of an effect the cryogenic copper shield has on blocking external electric and magnetic field noise.

More distant future goals would be to create an internal cryogenic DAC system close to the chip position to minimise the impedances of the DC electrode paths. While having active electronics will be a technical challenge both because it will need to operate at 4K but also because it introduces a noise source near the ion, it would allow for very fast DC voltage profiles to be generated and faster shuttling regimes to be performed.

This is very early days for the cryogenic system and I look forward to seeing what becomes of it in the years to come.

Bibliography

[1] Darren De Motte. *Cryogenic ion trapping for next generation quantum technologies*. PhD thesis, University of Sussex, dec 2015. URL http://sro.sussex.ac.uk/66011/. vi, ix, 13, 19, 20, 55, 60, 73, 75, 77, 84, 91, 110

[2] M. Johanning, A. Braun, D. Eiteneuer, C. Paape, C. Balzer, W. Neuhauser, and C. Wunderlich. Resonance-enhanced isotope-selective photoionization of YbI for ion trap loading. *Applied Physics B*, 103(2):327–338, April 2011. doi: 10.1007/s00340-011-4502-7. URL https://doi.org/10.1007/s00340-011-4502-7. vi, 18, 19, 20

[3] Y. Onoda, K. Sugiyama, M. Ikeda, and M. Kitano. Loading rate of yb^+ loaded through photoionization in radiofrequency ion trap. *Applied Physics B*, 105(4):729–740, May 2011. doi: 10.1007/s00340-011-4576-2. URL https://doi.org/10.1007/s00340-011-4576-2. vi, 18, 19

[4] Chr. Balzer, A. Braun, T. Hannemann, Chr. Paape, M. Ettler, W. Neuhauser, and Chr. Wunderlich. Electrodynamically trapped yb^+ ions for quantum information processing. *Phys. Rev. A*, 73:041407, Apr 2006. doi: 10.1103/PhysRevA.73.041407. URL https://link.aps.org/doi/10.1103/PhysRevA.73.041407. vi, 18, 19, 20

[5] Altaf H. Nizamani, James J. McLoughlin, and Winfried K. Hensinger. Doppler-free yb spectroscopy with the fluorescence spot technique. *Physical Review A*, 82(4), October 2010. doi: 10.1103/physreva.82.043408. URL https://doi.org/10.1103/physreva.82.043408. vi, 19, 20

[6] Dipankar Das, Sachin Barthwal, Ayan Banerjee, and Vasant Natarajan. Absolute frequency measurements in yb with0.08ppbuncertainty: Isotope shifts and hyperfine structure in the399-nmS01→p11line. *Physical Review A*, 72(3), September 2005. doi: 10.1103/physreva.72.032506. URL https://doi.org/10.1103/physreva.72.032506. vi, 19, 20

[7] T. Loftus, J. R. Bochinski, and T. W. Mossberg. Optical double-resonance cooled-atom spectroscopy. *Physical Review A*, 63(2), January 2001. doi: 10.1103/physreva.63.023402. URL https://doi.org/10.1103/physreva.63.023402. vi, 19, 20

[8] K. Deilamian, J. D. Gillaspy, and D. E. Kelleher. Isotope shifts and hyperfine splittings of the 3988-nm yb i line. *Journal of the Optical Society of America B*, 10(5):789, May 1993. doi: 10.1364/josab.10.000789. URL https://doi.org/10.1364/josab.10.000789. vi, 19, 20

[9] C Day. Basics and Applications of Cryopumps. *CERN Accelerator School Proceedings on 'Vacuum in Accelerators'*, pages 241–274, 2006. doi: 10.5170/CERN-2007-003.241. URL https://cds.cern.ch/record/1047069/files/p241.pdf. ix, 69, 70

[10] Shicryogenics. RDK-415D Capacity Map. Technical report, shicryogenics, 2012. URL http://www.shicryogenics.com//wp-content/uploads/2012/11/RDK-415D{_}Capacity{_}Map.pdf. ix, 75

[11] Constantine Balanis. *Antenna Theory : Analysis and Design*. Wiley, 2015. ISBN 978-1-119-17899-6. x, 93, 96, 101, 102, 103, 105, 109

[12] J Chiaverini and J M Sage. Insensitivity of the rate of ion motional heating to trap-electrode material over a large temperature range. *Physical Review A*, 89(1):012318, jan 2014. ISSN 1050-2947. doi: 10.1103/PhysRevA.89.012318. URL https://journals.aps.org/pra/pdf/10.1103/PhysRevA.89.012318https://link.aps.org/doi/10.1103/PhysRevA.89.012318. xiii, 71, 134, 135

[13] Alan M Turing. On computable numbers, with an application to the Entscheidungsproblem. *Proceedings of the London mathematical society*, 2(1):230–265, 1937. 3

[14] C. A. R. Hoare. Algorithm 64: Quicksort. *Communications of the ACM*, 4(7):321, jul 1961. ISSN 00010782. doi: 10.1145/366622.366644. URL http://portal.acm.org/citation.cfm?doid=366622.366644. 3

[15] John D. Dixon. Asymptotically fast factorization of integers. *Mathematics of Computation*, 36(153):255–255, jan 1981. ISSN 0025-5718. doi: 10.1090/S0025-5718-1981-0595059-1. URL http://www.ams.org/jourcgi/jour-getitem?pii=S0025-5718-1981-0595059-1. 3

[16] Peter W. Shor. Polynomial Time Algorithms for Prime Factorization and Discrete Logarithms on a Quantum Computer. *SIAM Journal on Computing*, 26(5):1484–1509, oct 1997. ISSN 0097-5397. doi: 10.1137/S0097539795293172. 5

[17] David Deutsch. Quantum Theory, the Church-Turing Principle and the Universal Quantum Computer. *Proceedings of the Royal Society A: Mathematical, Physical and Engineering Sciences*, 400(1818):97–117, jul 1985. ISSN 1364-5021. doi: 10.1098/rspa.1985.0070. URL https://people.eecs.berkeley.edu/{~}christos/classics/Deutsch{_}quantum{_}theory.pdfhttp://rspa.royalsocietypublishing.org/cgi/doi/10.1098/rspa.1985.0070. 5

[18] T. D. Ladd, F. Jelezko, R. Laflamme, Y. Nakamura, C. Monroe, and J. L. O'Brien. Quantum computers. *Nature*, 464(7285):45–53, mar 2010. ISSN 0028-0836. doi: 10.1038/nature08812. 5

[19] David P. DiVincenzo. The Physical Implementation of Quantum Computation. *Fortschritte der Physik*, 48(9-11):771–783, sep 2000. ISSN 00158208. doi: 10.1002/1521-3978(200009)48:9/11⟨771::AID-PROP771⟩3.0.CO;2-E. 5

[20] J Q You and Franco Nori. Atomic physics and quantum optics using superconducting circuits. *Nature*, 474(7353):589–597, jun 2011. ISSN 0028-0836. doi: 10.1038/nature10122. URL http://www.nature.com/doifinder/10.1038/nature10122http://www.ncbi.nlm.nih.gov/pubmed/21720362. 6

[21] M H Devoret and R J Schoelkopf. Superconducting Circuits for Quantum Information: An Outlook. *Science*, 339(6124):1169–1174, mar 2013. ISSN 0036-8075. doi: 10.1126/science.1231930. URL http://www.ncbi.nlm.nih.gov/pubmed/23471399http://www.sciencemag.org/cgi/doi/10.1126/science.1231930. 6

[22] F. Jelezko and J. Wrachtrup. Single defect centres in diamond: A review. *physica status solidi (a)*, 203(13):3207–3225, oct 2006. ISSN 18626300. doi: 10.1002/pssa.200671403. URL http://doi.wiley.com/10.1002/pssa.200671403. 6

[23] Lilian Childress and Ronald Hanson. Diamond NV centers for quantum computing and quantum networks. *MRS Bulletin*, 38(02):134–138, feb 2013. ISSN 0883-7694. doi: 10.1557/mrs.2013.20. URL http://www.journals.cambridge.org/abstract{_}S0883769413000201. 6

[24] Pieter Kok, W J Munro, Kae Nemoto, T C Ralph, Jonathan P Dowling, and G J Milburn. Linear optical quantum computing with photonic qubits. *Reviews of Mod-*

ern Physics, 79(1):135–174, jan 2007. ISSN 0034-6861. doi: 10.1103/RevModPhys.79.135. URL http://link.aps.org/doi/10.1103/RevModPhys.79.135. 6

[25] N. A. Gershenfeld and Isaac L Chuang. Bulk Spin-Resonance Quantum Computation. *Science*, 275(5298):350–356, jan 1997. ISSN 00368075. doi: 10.1126/science.275.5298.350. URL http://www.sciencemag.org/cgi/doi/10.1126/science.275.5298.350http://www.ncbi.nlm.nih.gov/pubmed/8994025. 6

[26] Christoph Kloeffel and Daniel Loss. Prospects for Spin-Based Quantum Computing in Quantum Dots. *Annual Review of Condensed Matter Physics*, 4(1):51–81, apr 2013. ISSN 1947-5454. doi: 10.1146/annurev-conmatphys-030212-184248. URL www.annualreviews.orghttp://www.annualreviews.org/doi/abs/10.1146/annurev-conmatphys-030212-184248. 6

[27] M Saffman, T G Walker, and K Mølmer. Quantum information with Rydberg atoms. *Reviews of Modern Physics*, 82(3):2313–2363, aug 2010. ISSN 0034-6861. doi: 10.1103/RevModPhys.82.2313. URL https://link.aps.org/doi/10.1103/RevModPhys.82.2313. 6

[28] H. Haeffner, C. F. Roos, and R. Blatt. Quantum computing with trapped ions. *Physics Reports*, 469(4):155–203, dec 2008. ISSN 03701573. doi: 10.1016/j.physrep.2008.09.003. URL http://linkinghub.elsevier.com/retrieve/pii/S0370157308003463http://arxiv.org/abs/0809.4368http://dx.doi.org/10.1016/j.physrep.2008.09.003. 6

[29] Rainer Blatt and David Wineland. Entangled states of trapped atomic ions. *Nature*, 453(7198):1008–1015, jun 2008. ISSN 0028-0836. doi: 10.1038/nature07125. URL http://www.nature.com/doifinder/10.1038/nature07125. 6

[30] D. De Motte, A. R. Grounds, M. Rehák, A. Rodriguez Blanco, B. Lekitsch, G. S. Giri, P. Neilinger, G. Oelsner, E. Il'ichev, M. Grajcar, and W. K. Hensinger. Experimental system design for the integration of trapped-ion and superconducting qubit systems. *Quantum Information Processing*, 15(12):5385–5414, dec 2016. ISSN 1570-0755. doi: 10.1007/s11128-016-1368-y. URL http://link.springer.com/10.1007/s11128-016-1368-y. 6

[31] Jan Benhelm, Gerhard Kirchmair, Christian F. Roos, and Rainer Blatt. Towards fault-tolerant quantum computing with trapped ions. *Nature Physics*, 4(6):463–466,

jun 2008. ISSN 1745-2473. doi: 10.1038/nphys961. URL http://www.nature.com/articles/nphys961. 6

[32] C. J. Ballance, T. P. Harty, N. M. Linke, M. A. Sepiol, and D. M. Lucas. High Fidelity Quantum Logic Gates Using Trapped-Ion Hyperfine Qubits. *Physical Review Letters*, 117(6):060504, aug 2016. ISSN 0031-9007. doi: 10.1103/PhysRevLett.117.060504. URL https://link.aps.org/doi/10.1103/PhysRevLett.117.060504. 6

[33] J. P. Gaebler, T. R. Tan, Y. Lin, Y. Wan, R. Bowler, A. C. Keith, S. Glancy, K. Coakley, E. Knill, D. Leibfried, and D. J. Wineland. High Fidelity Universal Gate Set for Be 9 + Ion Qubits. *Physical Review Letters*, 117(6):060505, aug 2016. ISSN 10797114. doi: 10.1103/PhysRevLett.117.060505. URL https://link.aps.org/doi/10.1103/PhysRevLett.117.060505. 6

[34] Marcus D Hughes, Bjoern Lekitsch, Jiddu A Broersma, and Winfried K Hensinger. Microfabricated ion traps. *Contemporary Physics*, 52(6):505–529, nov 2011. ISSN 0010-7514. doi: 10.1080/00107514.2011.601918. 6, 68

[35] B Lekitsch, S Weidt, A G Fowler, K Mølmer, S J Devitt, Ch Wunderlich, and W K Hensinger. Blueprint for a microwave ion trap quantum computer. *arXiv*, 1508.00420:1–11, aug 2015. URL http://arxiv.org/abs/1508.00420. 6

[36] C. J. Ballance, T. P. Harty, N. M. Linke, M. A. Sepiol, and D. M. Lucas. High-fidelity quantum logic gates using trapped-ion hyperfine qubits. *Phys. Rev. Lett.*, 117:060504, Aug 2016. doi: 10.1103/PhysRevLett.117.060504. URL https://link.aps.org/doi/10.1103/PhysRevLett.117.060504. 6

[37] S. Weidt, J. Randall, S. C. Webster, K. Lake, A. E. Webb, I. Cohen, T. Navickas, B. Lekitsch, A. Retzker, and W. K. Hensinger. Trapped-ion quantum logic with global radiation fields. *Phys. Rev. Lett.*, 117:220501, Nov 2016. doi: 10.1103/PhysRevLett.117.220501. URL https://link.aps.org/doi/10.1103/PhysRevLett.117.220501. 6

[38] Michael A. Nielsen and Isaac L. Chuang. *Quantum Computation and Quantum Information: 10th Anniversary Edition*. Cambridge University Press, 2010. doi: 10.1017/CBO9780511976667. 6

[39] M. E. Poitzsch, J. C. Bergquist, W. M. Itano, and D. J. Wineland. Cryogenic linear ion trap for accurate spectroscopy. *Review of Scientific Instruments*, 67(1):129–134, 1996. ISSN 00346748. doi: 10.1063/1.1146560. 6, 74

[40] M Schwarz, O O Versolato, A Windberger, F R Brunner, T Ballance, S N Eberle, J Ullrich, P O Schmidt, A K Hansen, A D Gingell, M Drewsen, and J R Crespo López-Urrutia. Cryogenic linear Paul trap for cold highly charged ion experiments Related Articles Cryogenic linear Paul trap for cold highly charged ion experiments. *Citation: Rev. Sci. Instrum*, 83:83115, 2012. doi: 10.1063/1.4742770://dx.doi.org/10.1063/1.4742770. URL http://phys.au.dk/fileadmin/site{_}files/forskning/iontrap/pdfs/Cryogenic{_}Schwarz{_}RevSciInstrum{_}83{_}2012.pdf. 6, 74

[41] P B Antohi, D Schuster, G M Akselrod, J Labaziewicz, Y Ge, Z Lin, W S Bakr, and I L Chuang. Cryogenic ion trapping systems with surface-electrode traps. *Review of Scientific Instruments*, 80(1):013103, 2009. ISSN 00346748. doi: 10.1063/1.3058605. URL http://scitation.aip.org/content/aip/journal/rsi/80/1/10.1063/1.3058605. 6, 74, 91

[42] Joseph Aidan Delf Randall. *High-fidelity entanglement of trapped ions using long-wavelength radiation*. PhD thesis, Imperial College London, 2016. URL https://spiral.imperial.ac.uk/handle/10044/1/31528. 8, 20, 21

[43] Klaus Mølmer and Anders Sørensen. Multiparticle Entanglement of Hot Trapped Ions. *Physical Review Letters*, 82(9):1835–1838, mar 1999. ISSN 0031-9007. doi: 10.1103/PhysRevLett.82.1835. URL http://link.aps.org/doi/10.1103/PhysRevLett.82.1835http://arxiv.org/abs/quant-ph/9810040{%}5Cnhttp://link.aps.org/doi/10.1103/PhysRevLett.82.1835. 8

[44] Altaf Hussain Nizamani. *Yb+ ion trapping and optimum planar trap geometries for scalable quantum technology*. PhD thesis, University of Sussex, 2011. URL http://sro.sussex.ac.uk/7171/. 8, 24, 91

[45] DJ Wineland and H Dehmelt. Proposed $1014\delta\nu/\nu$ laser fluorescence spectroscopy on tl+ mono-ion oscillator iii (side band cooling). *Bull. Am. Phys. Soc*, 20(4):637–637, 1975. 8

[46] J H Wesenberg, R J Epstein, D Leibfried, R B Blakestad, J Britton, J P Home, W M Itano, J D Jost, E Knill, C Langer, R Ozeri, S Seidelin, and D J Wineland. Fluorescence during Doppler cooling of a single trapped atom. *Physical Review A*, 76(5):053416, nov 2007. ISSN 1050-2947. doi: 10.1103/PhysRevA.

76.053416. URL https://journals.aps.org/pra/pdf/10.1103/PhysRevA.76.053416https://link.aps.org/doi/10.1103/PhysRevA.76.053416. 8, 17

[47] D. J. Wineland, R. E. Drullinger, and F. L. Walls. Radiation-pressure cooling of bound resonant absorbers. *Physical Review Letters*, 1978. ISSN 00319007. doi: 10.1103/PhysRevLett.40.1639. 10

[48] W. Neuhauser, M. Hohenstatt, P. Toschek, and H. Dehmelt. Optical-sideband cooling of visible atom cloud confined in parabolic well. *Physical Review Letters*, 1978. ISSN 00319007. doi: 10.1103/PhysRevLett.41.233. 10

[49] J. Walz, S. B. Ross, C. Zimmermann, L. Ricci, M. Prevedelli, and T. W. Hänsch. Confinement of electrons and ions in a combined trap with the potential for antihydrogen production. *Hyperfine Interactions*, 100(1):133–144, December 1996. doi: 10.1007/bf02059938. URL https://doi.org/10.1007/bf02059938. 11

[50] Wolfgang Paul. Electromagnetic traps for charged and neutral particles. *Reviews of Modern Physics*, 62(3):531–540, July 1990. doi: 10.1103/revmodphys.62.531. URL https://doi.org/10.1103/revmodphys.62.531. 11

[51] H.G. Dehmelt. Radiofrequency spectroscopy of stored ions i: Storage. In *Advances in Atomic and Molecular Physics Volume 3*, pages 53–72. Elsevier, 1968. doi: 10.1016/s0065-2199(08)60170-0. URL https://doi.org/10.1016/s0065-2199(08)60170-0. 12

[52] Raymond E March. An Introduction to Quadrupole Ion Trap Mass Spectrometry. *Journal of Mass Spectrometry*, 32(4):351–369, apr 1997. ISSN 1076-5174. doi: 10.1002/(SICI)1096-9888(199704)32:4⟨351::AID-JMS512⟩3.0.CO;2-Y. 13

[53] David Francesco Murgia. *Microchip ion traps with high magnetic field gradients for microwave quantum logic*. PhD thesis, Imperial College London, 2017. URL https://spiral.imperial.ac.uk/bitstream/10044/1/48045/1/Murgia-D-2017-PhD-Thesis.pdf. 13, 20, 79, 89, 91, 92, 101, 108, 109, 135

[54] Émile Mathieu. Mémoire sur le mouvement vibratoire d'une membrane de forme elliptique. *Journal de Mathématiques Pures et Appliquées*, 13:137–203, 1868. URL http://eudml.org/doc/234720. 13

[55] Harold J. Metcalf and Peter van der Straten. *Laser Cooling and Trapping*. 1999. ISBN 978-0-387-98728-6. doi: 10.1007/978-1-4612-1470-0. 16

[56] Kurt Gibble and Steven Chu. Laser-cooled cs frequency standard and a measurement of the frequency shift due to ultracold collisions. *Phys. Rev. Lett.*, 70:1771–1774, Mar 1993. doi: 10.1103/PhysRevLett.70.1771. URL https://link.aps.org/doi/10.1103/PhysRevLett.70.1771. 17

[57] H. Häffner, C.F. Roos, and R. Blatt. Quantum computing with trapped ions. *Physics Reports*, 469(4):155 – 203, 2008. ISSN 0370-1573. doi: https://doi.org/10.1016/j.physrep.2008.09.003. URL http://www.sciencedirect.com/science/article/pii/S0370157308003463. 17

[58] M. Saffman, T. G. Walker, and K. Mølmer. Quantum information with rydberg atoms. *Rev. Mod. Phys.*, 82:2313–2363, Aug 2010. doi: 10.1103/RevModPhys.82.2313. URL https://link.aps.org/doi/10.1103/RevModPhys.82.2313. 17

[59] C. Monroe, D. M. Meekhof, B. E. King, S. R. Jefferts, W. M. Itano, D. J. Wineland, and P. Gould. Resolved-sideband raman cooling of a bound atom to the 3d zero-point energy. *Phys. Rev. Lett.*, 75:4011–4014, Nov 1995. doi: 10.1103/PhysRevLett.75.4011. URL https://link.aps.org/doi/10.1103/PhysRevLett.75.4011. 17

[60] Ch. Roos, Th. Zeiger, H. Rohde, H. C. Nägerl, J. Eschner, D. Leibfried, F. Schmidt-Kaler, and R. Blatt. Quantum state engineering on an optical transition and decoherence in a paul trap. *Phys. Rev. Lett.*, 83:4713–4716, Dec 1999. doi: 10.1103/PhysRevLett.83.4713. URL https://link.aps.org/doi/10.1103/PhysRevLett.83.4713. 17

[61] Jürgen Eschner, Giovanna Morigi, Ferdinand Schmidt-Kaler, and Rainer Blatt. Laser cooling of trapped ions. *Journal of the Optical Society of America B*, 20 (5):1003, May 2003. doi: 10.1364/josab.20.001003. URL https://doi.org/10.1364/josab.20.001003. 17

[62] D. Leibfried. Experiments towards quantum information with trapped calcium ions. In *AIP Conference Proceedings*. AIP, 2001. doi: 10.1063/1.1354345. URL https://doi.org/10.1063/1.1354345. 17

[63] R J Epstein, S Seidelin, D Leibfried, J H Wesenberg, J J Bollinger, J M Amini, R B Blakestad, J Britton, J P Home, W M Itano, J D Jost, E Knill, C Langer, R Ozeri, N Shiga, and D J Wineland. Simplified motional heating rate measurements of trapped ions. *Physical Review A*, 76(3): 033411, sep 2007. ISSN 1050-2947. doi: 10.1103/PhysRevA.76.033411. URL

https://journals.aps.org/pra/pdf/10.1103/PhysRevA.76.033411http://arxiv.org/abs/0707.1528http://dx.doi.org/10.1103/PhysRevA.76.033411https://link.aps.org/doi/10.1103/PhysRevA.76.033411. 17

[64] J. Benhelm, G. Kirchmair, C. F. Roos, and R. Blatt. Experimental quantum-information processing with $^{43}Ca^{+}$ ions. *Phys. Rev. A*, 77:062306, Jun 2008. doi: 10.1103/PhysRevA.77.062306. URL https://link.aps.org/doi/10.1103/PhysRevA.77.062306. 18

[65] Ralph G. DeVoe and Christian Kurtsiefer. Experimental study of anomalous heating and trap instabilities in a microscopic ^{137}Ba ion trap. *Phys. Rev. A*, 65:063407, Jun 2002. doi: 10.1103/PhysRevA.65.063407. URL https://link.aps.org/doi/10.1103/PhysRevA.65.063407. 18

[66] M. Roberts, P. Taylor, G. P. Barwood, P. Gill, H. A. Klein, and W. R. C. Rowley. Observation of an electric octupole transition in a single ion. *Phys. Rev. Lett.*, 78: 1876–1879, Mar 1997. doi: 10.1103/PhysRevLett.78.1876. URL https://link.aps.org/doi/10.1103/PhysRevLett.78.1876. 20

[67] Florian Mintert and Christof Wunderlich. Ion-trap quantum logic using long-wavelength radiation. *Physical Review Letters*, 87(25), November 2001. doi: 10.1103/physrevlett.87.257904. URL https://doi.org/10.1103/physrevlett.87.257904. 20

[68] M. Johanning, A. Braun, N. Timoney, V. Elman, W. Neuhauser, and Chr. Wunderlich. Individual addressing of trapped ions and coupling of motional and spin states using rf radiation. *Phys. Rev. Lett.*, 102:073004, Feb 2009. doi: 10.1103/PhysRevLett.102.073004. URL https://link.aps.org/doi/10.1103/PhysRevLett.102.073004. 20

[69] C Ospelkaus, U Warring, Y Colombe, K R Brown, J M Amini, D Leibfried, and D J Wineland. Microwave quantum logic gates for trapped ions. *Nature*, 476(7359):181–184, aug 2011. ISSN 0028-0836. doi: 10.1038/nature10290. URL http://dx.doi.org/10.1038/nature10290http://www.nature.com/doifinder/10.1038/nature10290. 21

[70] N. Timoney, I. Baumgart, M. Johanning, A. F. Varón, M. B. Plenio, A. Retzker, and Ch. Wunderlich. Quantum gates and memory using microwave-dressed states.

Nature, 476(7359):185–188, August 2011. doi: 10.1038/nature10319. URL https://doi.org/10.1038/nature10319. 21

[71] Matthew Sadiku. *Numerical Techniques in Electromagnetics, Second Edition*. CRC Press, jul 2000. ISBN 978-0-8493-1395-0. doi: 10.1201/9781420058277. 23, 24, 25

[72] Raymond G. Mclenaghan and Giovanni Rastelli. Separation of variables for systems of first-order partial differential equations and the dirac equation in two-dimensional manifolds. In *Symmetries and Overdetermined Systems of Partial Differential Equations*, pages 471–496. Springer New York, 2008. doi: 10.1007/978-0-387-73831-4_25. URL https://doi.org/10.1007/978-0-387-73831-4_25. 23

[73] Weimin Wang, Wenying Ma, Qiang Wang, and Hao Ren. Conformal mapping for multiple terminals. *Scientific Reports*, 6(1), November 2016. doi: 10.1038/srep36918. URL https://doi.org/10.1038/srep36918. 23

[74] Mário H Oliveira and José A Miranda. Biot-savart-like law in electrostatics. *European Journal of Physics*, 22(1):31–38, January 2001. doi: 10.1088/0143-0807/22/1/304. URL https://doi.org/10.1088/0143-0807/22/1/304. 23

[75] M. G. House. Analytic model for electrostatic fields in surface electrode ion traps. *Physical Review A*, 78(3):033402, sep 2008. ISSN 1050-2947. doi: 10.1103/PhysRevA.78.033402. 23, 30

[76] A. Thom, C.J. Apelt, and G.F.J. Temple. *Field Computations in Engineering and Physics*. Literary Licensing, LLC, 2013. ISBN 9781258812126. URL https://books.google.co.uk/books?id=ruZqngEACAAJ. 24

[77] Lawrence Sirovich. *Introduction to Applied Mathematics*. Springer New York, 1988. doi: 10.1007/978-1-4612-4580-3. URL https://doi.org/10.1007/978-1-4612-4580-3. 24

[78] Roger Harrington. *Field computation by moment methods*. IEEE Press, Piscataway, NJ, 1993. ISBN 978-0-780-31014-8. 24

[79] Peter Bettess. The finite element method vol. 1: Basic formulation and linear problems, fourth edition by o. c. zienkiewicz and r. l. taylor, McGraw-hill, maidenhead, england, 1989. no. of pages: 648. price (cloth): £25.00 ISBN: 0-07-084174-8. *International Journal for Numerical Methods in Engineering*, 30(3):565–567, August 1990.

doi: 10.1002/nme.1620300312. URL https://doi.org/10.1002/nme.1620300312. 24

[80] A. F. Peterson and R. Mittra. Method of conjugate gradients for the numerical solution of large-body electromagnetic scattering problems. *Journal of the Optical Society of America A*, 2(6):971, June 1985. doi: 10.1364/josaa.2.000971. URL https://doi.org/10.1364/josaa.2.000971. 24

[81] M. L. James. *Applied numerical methods for digital computation*. HarperCollins College Publishers, New York, NY, 1993. ISBN 9780065004946. 24

[82] Kilian Singer, Ulrich Poschinger, Michael Murphy, Peter Ivanov, Frank Ziesel, Tommaso Calarco, and Ferdinand Schmidt-Kaler. Colloquium : Trapped ions as quantum bits: Essential numerical tools. *Reviews of Modern Physics*, 82(3): 2609–2632, sep 2010. ISSN 0034-6861. doi: 10.1103/RevModPhys.82.2609. URL https://link.aps.org/doi/10.1103/RevModPhys.82.2609. 25, 27, 28, 37

[83] John T. Katsikadelis. *Boundary Elements. Theory and Applications*. Elsevier, 2002. ISBN 0-080-44107-6. 25, 27

[84] Rene Brun, Fons Rademakers, Philippe Canal, Axel Naumann, Olivier Couet, Lorenzo Moneta, Vassil Vassilev, Sergey Linev, Danilo Piparo, Gerardo GANIS, Bertrand Bellenot, Enrico Guiraud, Guilherme Amadio, Wverkerke, Pere Mato, TimurP, Matevž Tadel, Wlav, Enric Tejedor, Jakob Blomer, Andrei Gheata, Stephan Hageboeck, Stefan Roiser, Marsupial, Stefan Wunsch, Oksana Shadura, Anirudha Bose, CristinaCristescu, Xavier Valls, and Raphael Isemann. root-project/root: v6.18/02, 2019. URL https://zenodo.org/record/3895860. 28

[85] M.˜T. Homer Reid and S.˜G. Johnson. Efficient Computation of Power, Force, and Torque in BEM Scattering Calculations. *ArXiv e-prints*, jul 2013. 29

[86] M.˜T. Homer Reid and S.˜G. Johnson. SCUFFEM Github. URL http://github.com/homerreid/scuff-EM. 29

[87] John B. Bell, A. N. Tikhonov, and V. Y. Arsenin. Solutions of Ill-Posed Problems. *Mathematics of Computation*, 32(144):1320, oct 1978. ISSN 00255718. doi: 10.2307/2006360. 37

[88] E. (Ernst) Hairer, S. P. (Syvert Paul) Nørsett, and Gerhard Wanner. Solving ordinary differential equations I. nonstiff problems. *Mathematics and Computers in Sim-*

ulation, 29(5):447, oct 1987. ISSN 03784754. doi: 10.1016/0378-4754(87)90083-8. URL http://linkinghub.elsevier.com/retrieve/pii/0378475487900838. 37

[89] Thorlabs. Precision Pinholes and Pinhole Wheel, 2017. URL https://www.thorlabs.com/newgrouppage9.cfm?objectgroup{_}id=1400. 51

[90] James McLoughlin. *Development and implementation of an Yb+ ion trap experiment towards coherent manipulation and entanglement*. PhD thesis, University of Sussex, 2012. URL http://sro.sussex.ac.uk/40783/. 68

[91] K. Erents and G. M. McCracken. Thermal release of hydrogen isotopes from cryogenic surfaces. *Vacuum*, 21(7):257–260, jul 1971. ISSN 0042207X. doi: 10.1016/0042-207X(71)91357-1. URL https://www.sciencedirect.com/science/article/pii/0042207X71913571?via{%}3Dihubhttp://linkinghub.elsevier.com/retrieve/pii/0042207X71913571. 69

[92] G Pagano, P W Hess, H B Kaplan, W L Tan, P Richerme, P Becker, A Kyprianidis, J Zhang, E Birckelbaw, M R Hernandez, Y Wu, and C Monroe. Cryogenic Trapped-Ion System for Large Scale Quantum Simulation. feb 2018. URL https://arxiv.org/pdf/1802.03118.pdfhttp://arxiv.org/abs/1802.03118. 69, 96

[93] Todd Raeker. Physical Adsorption: Forces and Phenomena (Bruch, L.W.; Cole, Milton W.; Zaremba, Eugene). *Journal of Chemical Education*, 75(12):1557, dec 1998. ISSN 0021-9584. doi: 10.1021/ed075p1557. URL http://pubs.acs.org/doi/abs/10.1021/ed075p1557. 70

[94] V. Ponec, Z. Knor, and S. Černý. Sorption and reactions of atomized hydrogen on metals. *Journal of Catalysis*, 4(4):485–498, 1965. ISSN 10902694. doi: 10.1016/0021-9517(65)90053-9. 70

[95] Geoffrey Maitland, Maurice Rigby, E Brian Smith, and W a Wakeham. Intermolecular Forces: Their Origin and Determination. *The International Series of Monographs on Chemistry*, 3(4):616, 1987. ISSN 00319228. doi: 10.1063/1.2915587. URL http://www.amazon.com/Intermolecular-Forces-Determination-International-Monographs/dp/0198556411. 70

[96] John Bertrand Johnson. Thermal Agitation of Electricity in Conductors. *Physical Review*, 32(1):97–109, jul 1928. ISSN 0031-899X. doi: 10.1103/PhysRev.32.97. URL http://link.aps.org/doi/10.1103/PhysRev.32.97. 70

[97] Harry Nyquist. Thermal Agitation of Electric Charge in Conductors. *Physical Review*, 32(1):110–113, jul 1928. ISSN 0031-899X. doi: 10.1103/PhysRev.32.110. URL http://link.aps.org/doi/10.1103/PhysRev.32.110. 71

[98] J. H. Dellinger. The temperature coefficient of resistance of copper. *Journal of the Franklin Institute*, 170(3):213–216, 1910. ISSN 00160032. doi: 10.1016/S0016-0032(10)90872-7. 71

[99] Q A Turchette, Kielpinski, B E King, D Leibfried, D M Meekhof, C J Myatt, M A Rowe, C A Sackett, C S Wood, W M Itano, C Monroe, and D J Wineland. Heating of trapped ions from the quantum ground state. *Physical Review A*, 61(6):063418, may 2000. ISSN 1050-2947. doi: 10.1103/PhysRevA.61.063418. URL https://journals-aps-org.ezproxy.sussex.ac.uk/pra/pdf/10.1103/PhysRevA.61.063418https://link.aps.org/doi/10.1103/PhysRevA.61.063418. 71

[100] Ivan A. Boldin, Alexander Kraft, and Christof Wunderlich. Measuring anomalous heating in a planar ion trap with variable ion-surface separation. *Physical Review Letters*, 120(2), January 2018. doi: 10.1103/physrevlett.120.023201. URL https://doi.org/10.1103/physrevlett.120.023201. 71

[101] D T C Allcock, L Guidoni, T P Harty, C J Ballance, M G Blain, A M Steane, and D M Lucas. Reduction of heating rate in a microfabricated ion trap by pulsed-laser cleaning. *New Journal of Physics*, 13(12):123023, dec 2011. ISSN 1367-2630. doi: 10.1088/1367-2630/13/12/123023. URL http://stacks.iop.org/1367-2630/13/i=12/a=123023?key=crossref.a64e2d675f5dd69983a07d7624d8928d. 71

[102] D. A. Hite, Y. Colombe, A. C. Wilson, K. R. Brown, U. Warring, R. Jördens, J. D. Jost, K. S. McKay, D. P. Pappas, D. Leibfried, and D. J. Wineland. 100-Fold Reduction of Electric-Field Noise in an Ion Trap Cleaned with In Situ Argon-Ion-Beam Bombardment. *Physical Review Letters*, 109(10):103001, sep 2012. ISSN 0031-9007. doi: 10.1103/PhysRevLett.109.103001. URL https://link.aps.org/doi/10.1103/PhysRevLett.109.103001. 71

[103] N. Daniilidis, S. Gerber, G. Bolloten, M. Ramm, A. Ransford, E. Ulin-Avila, I. Talukdar, and H. Häffner. Surface noise analysis using a single-ion sensor. *Physical Review B*, 89(24):245435, jun 2014. ISSN 1098-0121. doi: 10.1103/PhysRevB.89.245435. URL https://link.aps.org/doi/10.1103/PhysRevB.89.245435. 71

[104] Jaroslaw Labaziewicz, Yufei Ge, Paul Antohi, David Leibrandt, Kenneth R Brown, and Isaac L Chuang. Suppression of Heating Rates in Cryogenic Surface-Electrode Ion Traps. *Physical Review Letters*, 100 (1):013001, jan 2008. ISSN 0031-9007. doi: 10.1103/PhysRevLett.100.013001. URL https://journals.aps.org/prl/pdf/10.1103/PhysRevLett.100.013001https://link.aps.org/doi/10.1103/PhysRevLett.100.013001. 71

[105] T H Geballe and B T Matthias. Superconductivity. *Annual Review of Physical Chemistry*, 14(1):141–160, oct 1963. ISSN 0066-426X. doi: 10.1146/annurev.pc.14.100163.001041. URL http://www.annualreviews.org/doi/10.1146/annurev.pc.14.100163.001041. 72

[106] J. Bardeen, L. N. Cooper, and J. R. Schrieffer. Theory of Superconductivity. *Physical Review*, 108(5):1175–1204, dec 1957. ISSN 0031-899X. doi: 10.1103/PhysRev.108.1175. URL https://journals.aps.org/pr/pdf/10.1103/PhysRev.108.1175https://link.aps.org/doi/10.1103/PhysRev.108.1175. 72

[107] S. M. Anton, J. S. Birenbaum, S. R. O'Kelley, V. Bolkhovsky, D. A. Braje, G. Fitch, M. Neeley, G. C. Hilton, H.-M. Cho, K. D. Irwin, F. C. Wellstood, W. D. Oliver, A. Shnirman, and John Clarke. Magnetic Flux Noise in dc SQUIDs: Temperature and Geometry Dependence. *Physical Review Letters*, 110(14):147002, apr 2013. ISSN 0031-9007. doi: 10.1103/PhysRevLett.110.147002. URL https://link.aps.org/doi/10.1103/PhysRevLett.110.147002. 72

[108] Kunihiro Okada, Michiharu Wada, Takashi Nakamura, Ichiro Katayama, Ludwig Boesten, and Shunsuke Ohtani. Cryogenic ion trap for minimization of trapped ion loss. *Japanese Journal of Applied Physics, Part 1: Regular Papers and Short Notes and Review Papers*, 40(6 A):4221–4222, 2001. ISSN 00214922. doi: 10.1143/JJAP.40.4221. 74

[109] PB Antohi. *Cryogenic Surface Electrode Ion Traps with Integrated Superconducting Microwave Resonators for Polar Molecule Ion Spectroscopy*. PhD thesis, Massachusetts Institute of Technology, 2011. URL https://dspace.mit.edu/handle/1721.1/68866http://dspace.mit.edu/handle/1721.1/68866. 74, 91

[110] Grahame Vittorini, Kenneth Wright, Kenneth R. Brown, Alexa W. Harter, and S. Charles Doret. Modular cryostat for ion trapping with surface-electrode ion traps.

Review of Scientific Instruments, 84(4), 2013. ISSN 00346748. doi: 10.1063/1.4802948. 74

[111] T. Trollier. Trade-Off between Thermal Link Solutions for the Cryosystem Cryocooler On-Board the International Space Station, jul 2004. ISSN 0094243X. URL http://aip.scitation.org/doi/abs/10.1063/1.1774805. 75

[112] J. A. Dean. Lange's handbook of chemistry. *Materials and Manufacturing Processes*, 5(4):687–688, 1990. ISSN 15322475. doi: 10.1080/10426919008953291. 87

[113] Steffen Kahra. *Trapping and cooling of single molecular ions for time resolved experiments*. PhD thesis, Ludwig-Maximilians-Universität München, mar 2010. URL https://edoc.ub.uni-muenchen.de/12880/http://nbn-resolving.de/urn:nbn:de:bvb:19-128803. 91

[114] Günther Leschhorn. Time-resolved measurements on a single molecular target and Discrete Kink Solitons in Ion traps. jan 2011. URL http://nbn-resolving.de/urn:nbn:de:bvb:19-139027. 91

[115] Paul Horowitz and Hill Winfield. The Art of Electronics. *American Journal of Physics*, page 1131, 1990. ISSN 00029505. doi: 10.1119/1.16385. 93, 94, 95, 96, 97, 98, 99

[116] W. Macalpine and R. Schildknecht. Coaxial Resonators with Helical Inner Conductor. *Proceedings of the IRE*, 47(12):2099–2105, dec 1959. ISSN 0096-8390. doi: 10.1109/JRPROC.1959.287128. URL http://ieeexplore.ieee.org/document/4065638/. 95, 96

[117] J. D. Siverns, L. R. Simkins, S. Weidt, and W. K. Hensinger. On the application of radio frequency voltages to ion traps via helical resonators. *Applied Physics B*, 107(4):921–934, jun 2012. ISSN 0946-2171. doi: 10.1007/s00340-011-4837-0. URL http://link.springer.com/10.1007/s00340-011-4837-0. 95

[118] D Gandolfi, M Niedermayr, M Kumph, M Brownnutt, and R Blatt. Compact radio-frequency resonator for cryogenic ion traps. *Review of Scientific Instruments*, 83(8):084705, aug 2012. ISSN 0034-6748. doi: 10.1063/1.4737889. URL http://aip.scitation.org/toc/rsi/83/8http://aip.scitation.org/doi/10.1063/1.4737889. 96, 97

[119] M F Brandl, P. Schindler, T. Monz, and R. Blatt. Cryogenic resonator design for trapped ion experiments in Paul traps. *Applied Physics B*, 122 (6):157, jun 2016. ISSN 0946-2171. doi: 10.1007/s00340-016-6430-z. URL https://link.springer.com/content/pdf/10.1007{%}2Fs00340-016-6430-z.pdfhttp://link.springer.com/10.1007/s00340-016-6430-z. 96, 97

[120] Anastasiya Khromova aus Sankt Petersburg, C O Wunderlich Gühne Gutachter der Disputation, and C O Wunderlich Gühne C Grupen T Mannel. *Quantum Gates with Trapped Ions using Magnetic Gradient Induced Coupling*. PhD thesis, University of Siegen, 2012. URL http://dokumentix.ub.uni-siegen.de/opus/volltexte/2012/672/pdf/khromova.pdf. 101, 108

[121] M.J. Withers. Handbook of Microstrip Antennas. *IEE Review*, 36(9):354, 1990. ISSN 09535683. doi: 10.1049/ir:19900148. URL http://digital-library.theiet.org/content/journals/10.1049/ir{_}19900148. 103, 104, 105

[122] K. Carver and J. Mink. Microstrip antenna technology. *IEEE Transactions on Antennas and Propagation*, 29(1):2–24, jan 1981. ISSN 0096-1973. doi: 10.1109/TAP.1981.1142523. URL http://ieeexplore.ieee.org/document/1142523/. 103, 104, 105

[123] Inam E. Rana and Nicolaos G. Alexopoulos. Current Distribution and Input Impedance of Printed Dipoles. *IEEE Transactions on Antennas and Propagation*, 29 (1):99–105, 1981. ISSN 15582221. doi: 10.1109/TAP.1981.1142536. 104

[124] J.R. Mosig and F.E. Gardiol. General integral equation formulation for microstrip antennas and scatterers. *IEE Proceedings H Microwaves, Antennas and Propagation*, 132(7):424, 1985. ISSN 0950107X. doi: 10.1049/ip-h-2.1985.0076. URL http://digital-library.theiet.org/content/journals/10.1049/ip-h-2.1985.0076. 104

[125] M. Bailey and M. Deshpande. Integral equation formulation of microstrip antennas. *IEEE Transactions on Antennas and Propagation*, 30(4):651–656, 1982. ISSN 0096-1973. doi: 10.1109/TAP.1982.1142880. URL http://ieeexplore.ieee.org/lpdocs/epic03/wrapper.htm?arnumber=1142880. 104

[126] E. Hammerstad and O. Jensen. Accurate models for microstrip computer-aided design. In *1980 IEEE MTT-S International Microwave symposium Digest*, pages 407–409, 1980. doi: 10.1109/MWSYM.1980.1124303. 105

[127] D.R. Jackson and N.G. Alexopoulos. Simple approximate formulas for input resistance, bandwidth, and efficiency of a resonant rectangular patch. *IEEE Transactions on Antennas and Propagation*, 39(3):407–410, mar 1991. ISSN 0018926X. doi: 10.1109/8.76341. URL http://ieeexplore.ieee.org/document/76341/. 105

[128] Jeong-Seok Lee, Tae-Lim Song, Jin-Kyoung Du, Tae-Wan Koo, and Jong-Gwan Yook. A study on near-field to far-field transformation using stratton-chu formula. *The Journal of Korean Institute of Electromagnetic Engineering and Science*, 24(3): 316–323, March 2013. doi: 10.5515/kjkiees.2013.24.3.316. URL https://doi.org/10.5515/kjkiees.2013.24.3.316. 107

[129] Steven W. Van Sciver. Low-Temperature Materials Properties. In *Helium Cryogenics*, pages 17–58. Springer New York, New York, NY, 2012. ISBN 9781441999788. doi: 10.1007/978-1-4419-9979-5_2. URL http://link.springer.com/10.1007/978-1-4419-9979-5{_}2. 107

[130] K.R. Williams and R.S. Muller. Etch rates for micromachining processing. *Journal of Microelectromechanical Systems*, 5(4):256–269, 1996. ISSN 10577157. doi: 10.1109/84.546406. 117

[131] Curtis T. Rueden, Johannes Schindelin, Mark C. Hiner, Barry E. DeZonia, Alison E. Walter, Ellen T. Arena, and Kevin W. Eliceiri. ImageJ2: ImageJ for the next generation of scientific image data. *BMC Bioinformatics*, 18(1):529, dec 2017. ISSN 1471-2105. doi: 10.1186/s12859-017-1934-z. 119

[132] Johannes Schindelin, Ignacio Arganda-Carreras, Erwin Frise, Verena Kaynig, Mark Longair, Tobias Pietzsch, Stephan Preibisch, Curtis Rueden, Stephan Saalfeld, Benjamin Schmid, Jean-Yves Tinevez, Daniel James White, Volker Hartenstein, Kevin Eliceiri, Pavel Tomancak, and Albert Cardona. Fiji: an open-source platform for biological-image analysis. *Nature Methods*, 9(7):676–682, jul 2012. ISSN 1548-7091. doi: 10.1038/nmeth.2019. 119

[133] Tobias Pietzsch, Stephan Saalfeld, Stephan Preibisch, and Pavel Tomancak. BigDataViewer: visualization and processing for large image data sets. *Nature Methods*, 12(6):481–483, jun 2015. ISSN 1548-7091. doi: 10.1038/nmeth.3392. 119

[134] Yuzo Takahashi. Two hundred years of lichtenberg figures. *Journal of Electrostatics*, 6(1):1–13, February 1979. doi: 10.1016/0304-3886(79)90020-2. URL https://doi.org/10.1016/0304-3886(79)90020-2. 122

[135] Michael Niedermayr, Kirill Lakhmanskiy, Muir Kumph, Stefan Partel, Jonannes Edlinger, Michael Brownnutt, and Rainer Blatt. Cryogenic surface ion trap based on intrinsic silicon. *New Journal of Physics*, 16(11):113068, nov 2014. ISSN 1367-2630. doi: 10.1088/1367-2630/16/11/113068. 129

[136] M. Brownnutt, M. Kumph, P. Rabl, and R. Blatt. Ion-trap measurements of electric-field noise near surfaces. *Reviews of Modern Physics*, 87(4):1419–1482, dec 2015. ISSN 0034-6861. doi: 10.1103/RevModPhys.87.1419. 134

Appendix A

Beam Blocks

During experiments the 369.5 nm laser can be turned off using the AOM switch previously described is section 4.2. But it is also useful to be able to turn off and on the other lasers. Firstly for safety when approaching the upper optics table with equipment, for example. But is also useful during trapping runs. When trapping on a new ion trap, the various voltage parameters will likely be sub-optimal, this can create a "fuzzy" uncrystallised ion that is not clearly defined on the camera. Cycling the 935.2 nm laser light on and off causes the ion to go bright and dark. This is caused by the ion being unable to fluoresce when trapped in the $^2D_{3/2}$ state when the laser is blocked. This brightening and darkening can be seen as an average photon count on the imaging camera, even when the ion is not crystalised. Turning off the 399 nm light is used when you have trapped an ion and do not wish to trap more. The oven takes a finite time to cool down and during this time atoms are still being emitted. With the 399 nm laser on there is a risk of trapping unwanted ions, so blocking the laser allows for better trapping control.

The beamblock unit consists of a servo motor mounted in a box with a light absorbing armature, when the servo arm is moved in the path of the beam it blocks the light. This allows the laser to be left on which is critical for locking but allows on/off times of around 150ms to be achieved. The servo works by sending pulses down a data wire, the window for the pulses is always 20ms, if you vary the pulse width between 0.75ms and 2.25ms in the 20ms window the servo moves to represent an angular scale from 0 to 180 degrees where 0.75ms represents 0 degrees.

To save from using three digital outputs from the experimental computer, a Arduino micro-controller was used with a mosfet driver board (see Figure A.1) which controls the three beam blocks (Circuit diagram can be found in the appendix). The PCM data lines

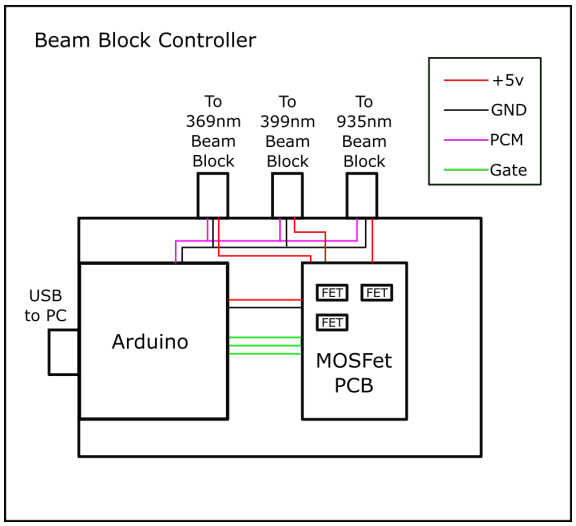

Figure A.1: Beam block controller. Pulse coded modulation (PCM Data) and ground lines are shared between all beam blocks. The MOSFETs are switched by the Gate lines, enabling each servo when required.

carry the 20ms windowed signal which is shared between all beam blocks. The power lines are switched by MOSFETs and their gates are switched by the micro-controller. This only allows one beam block to be active at a time, but this is intentional as the device is powered by USB and must fall bellow the 500mA limit for the port. Also when the beam blocks are static they shutdown fully, which increases their life span and stops static jitter which is a common problem with servos. Static jitter is where the servo will vibrate at high frequencies when being held at a constant angle. This has detrimental effects on lasers and locking setups. Since the servos are geared motors they can hold the armature position when disabled.